Atomistic simulation study of the radiation resistance of high/medium entropy alloys

YANGEN LI

SEPTEMBER 2023

Atomistic simulation study of the radiation resistance of high/medium entropy alloys

A dissertation submitted to

THE GRADUATE SCHOOL OF ENGINEERING SCIENCE

OSAKA UNIVERSITY

in partial fulfillment of the requirements for the degree of

DOCTOR OF PHILOSOPHY IN ENGINEERING

BY

YANGEN LI

SEPTEMBER 2023

Abstract

High/medium entropy alloys (H/MEAs) as new proposed materials have attracted extensive attention because of their outstanding properties, such as high strength, high tensile ductility and good corrosion. In particular, their excellent radiation resistance makes them possible to be applied to the development of the next-generation nuclear energy and contributes to the development of sustainable energy sources. However, the mechanism of radiation resistance and defect behavior of H/MEAs have not been fully understood at the atomic scale. In order to better understand the properties of H/MEAs and facilitate the development of high-performance H/MEAs. In this work, we have used a variety of atomic simulation methods, including density function theory (DFT), molecular dynamic (MD) and Monte Carlo (MC) to systematically study the surface radiation resistance and internal defects evolution of CoNiCrFeMn HEA. We have also further studied the chemical ordering effect on the radiation resistance of CoNiCrFeMn HEA, as well as the chemical ordering structures in CrCoNi MEA and its effect on defect diffusion behavior.

Surface radiation results show that compared to pure Ni, CoNiCrFeMn HEA has less defects during a single primary knock-on atom (PKA) process, and the average depth of defects distribution is shallower. For the consecutive radiation bombardments, CoNiCrFeMn HEA also exhibits much higher surface radiation resistance. Even under extreme irradiation flux, the number of defects in CoNiCrFeMn HEA is much less and stable and suggesting good surface radiation resistance, while in the pure Ni, the formation of dislocation will lead to a boost of defects. As for the internal radiation results, compared to pure Ni, less defects and dislocations are produced in the CoNiCrFeMn HEA, and interstitial cluster have much smaller mean free path (MFP) and exhibit a 3-D motion during migration. The 3-D motion of interstitial cluster in HEA will increase the opportunity of recombination of interstitial and vacancy, which may explain the mechanism of good radiation resistance in HEAs.

We further studied the chemical ordering of CoNiCrFeMn HEA and its effect on radiation resistance. The hybrid MD – MC annealing simulation results show that an initial stage Cr-rich region will form in CoNiCrFeMn HEA at a lower temperature of 600 K; whereas, annealing at a higher temperature of 1100 K will form a chemical short-range order (CSRO). MD radiation damage simulation shows that the Cr-rich region accelerates the aggregation and evolution of defects, facilitating more dislocation formation. On the other hand, the CSRO effectively delays the growth of defect number and tends to reduce the dislocation density and defect diffusion, suggesting enhanced radiation resistance. However, the CSRO structure will be destroyed by radiation damage, thus the enhanced radiation resistance will disappear in due time. Therefore, we propose a CSRO radiation damage – diffusion healing competition model, which can help us to better understand and design radiation resistance HEAs with CSRO enhanced effect.

Finally, chemical ordering structure and its effect on interstitial and vacancy diffusion are studied in CrCoNi MEA. A machine learning neural network potential (NNP) based on the DFT training dataset is used to accurately describe interatomic interactions in CrCoNi MEA. After annealing at 673 K, long-range chemical ordering structures will form in CrCoNi MEA. Interstitial and vacancy diffusion results show that the formation of chemical ordering structures could reduce diffusion trajectories and mean squared displacement (MSD), which will lead to the sluggish diffusion phenomenon. A mesh region division method was used to investigate the correlation between interstitial or vacancy diffusion region and the distribution of chemical ordering structures. Our results show that chemical ordering structures could limit interstitial and vacancy diffusion region, and lead to the sluggish diffusion phenomenon.

Contents

Chapter 1

Introduction to high/medium entropy alloys and atomic simulation

1.1 High/medium entropy alloys

The widespread use of metallic materials has greatly contributed to the progress of human society and the history of human is also the history of the development of metal materials. In the past, metal materials were often used with only one principal element, and were named after it. For example, iron was the principal element in steel, magnesium was the principal element in magnesium alloys, and titanium was the principal element in titanium alloys. This limitation leads to a bottleneck in the development of metal materials. With the development of technology, people continue to explore and break through the range of chemical composition of alloys, looking for new metal materials with better properties. Recently, a new type of amorphous alloy known as high/medium entropy alloys (H/MEAs) has been rapidly developed and has gained widely attention due to the excellent properties.

In 2004, Cantor et al. prepared the first equimolar CrMnFeCoNi alloy, the well-known Cantor alloy [**1**]. In the same year, Yeh et al. published the results of multi-component alloys and introduced the concept of high-entropy alloys (HEAs) for the first time [**2**]. Since then, HEAs have received widespread attention from the materials community and entered a phase of rapid development, while also giving rise to concepts such as medium entropy alloys (MEAs) [**3**–**6**]. H/MEAs often tend to have a simple FCC or BCC structure without forming intermetallic compounds or other complex structures. The unique crystalline structure allows H/MEAs to exhibit many excellent properties such as high strength, high temperature toughness, thermal stability, corrosion resistance and oxidation resistance [**7**–**12**]. Therefore, H/MEAs are not only valuable in theoretical research, but also have great potential for application in industrial production. Currently, H/MEAs are used as functional and structural materials in aircraft engines, ship structures, cutting tools and other applications [**3, 13**]. In particular, their excellent irradiation resistance is expected to meet the development of next-generation nuclear reactors and has become a popular research topic in the field

of nuclear structural materials [**14**–**17**].

The definition of HEAs originates from the name "high entropy". As we all known, entropy is a physical quantity that indicates the degree of disorder in a system and its magnitude can affect the thermodynamics stability of the system. The change in entropy in an alloy system is dominated by the configurational entropy. Therefore, according to the statistic mechanics and Boltzmann's hypothesis, the disorder degree of a system is related to the value of configurational entropy ΔS_{conf} as following equation:

$$\Delta S_{conf} = -R\sum_{i=1}^{n}(x_i \ln x_i) \tag{1.1}$$

where R is the molar gas constant, n is the number of principal elements of HEAs and x_i is the molar fraction of the principal element i. When the molar fraction of the principal elements are equal, the **Eq. 1.1** can be translated into $\Delta S_{conf} = R\ln n$, and the configurational entropy of an equiatomic HEA with five elements is calculated as $1.6R$. As shown in **Fig. 1.1**, based on the above definitions, alloys can be defined as high entropy alloys, medium entropy alloys, and lower entropy alloys, according to the calculation of the configurational entropy [**18, 19**]. HEAs differ significantly from conventional alloys in terms of thermodynamics, kinetics as well as properties and organisation. These differences are generally considered to be related to the following four core effects of HEAs: (1) high entropy effect in thermodynamics, (2) cocktail effect on property, (3) sluggish diffusion effect in dynamics, and (4) severe lattice distortion effect on structure [**20**].

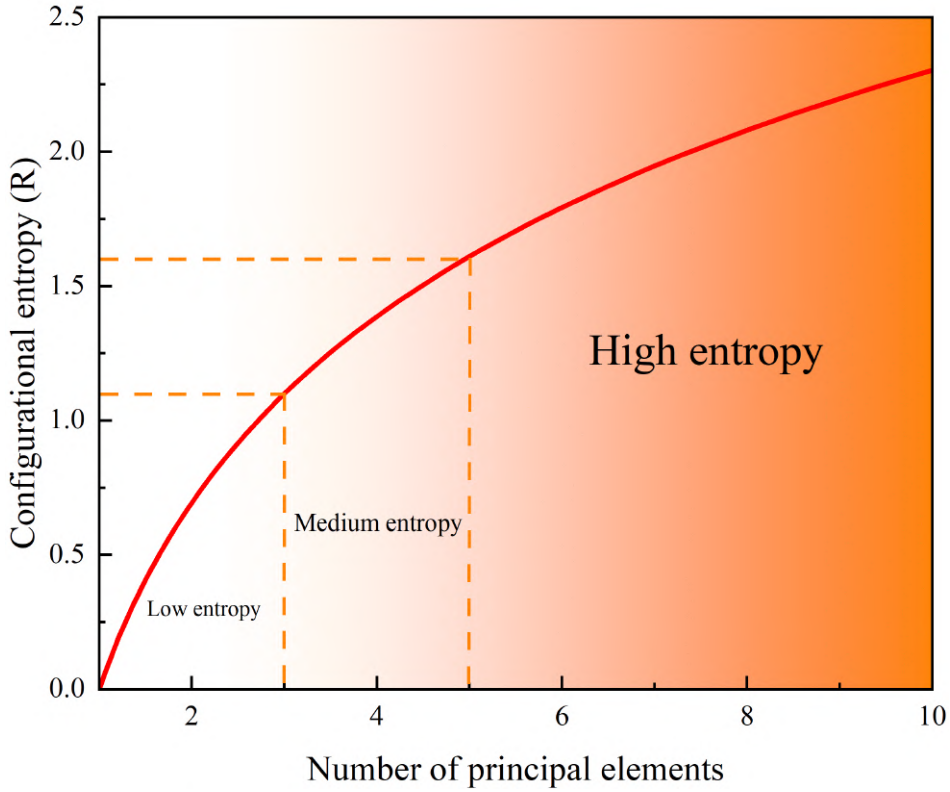

Figure 1.1: Relationship between the configurational entropy and the number of principal elements.

1.2 Effects of high entropy alloys

1.2.1 High entropy effect

The most important effect of HEAs is the high entropy effect. According to previous definition, the entropy of traditional alloys is generally below $1R$, while HEAs is larger than $1.6R$. HEAs tend to form fcc, bcc or hcp solid solutions with simple phase structures, which indicates that the high entropy will affect the phase formation pattern. The maximum number of phases in an alloy can be calculated as following equation:

$$P = C + 1 - F \tag{1.2}$$

where P is the maximum number of phases, C is the number of principal elements, and F is the thermodynamic degree of freedom. As shown in **Fig. 1.2**, generally, the higher the number of principal elements will lead to the higher the number of phases. However, in fact, the number of phases formed in HEAs is much lower than the calculation results [**4**]. Simple single-phase tend to form in HEAs, rather than multiple complex phases. This is because the higher mixing entropy leads to greater compatibility between the principal elements, thus avoiding the formation of solid solutions or intermetallic compounds due to phase separation.

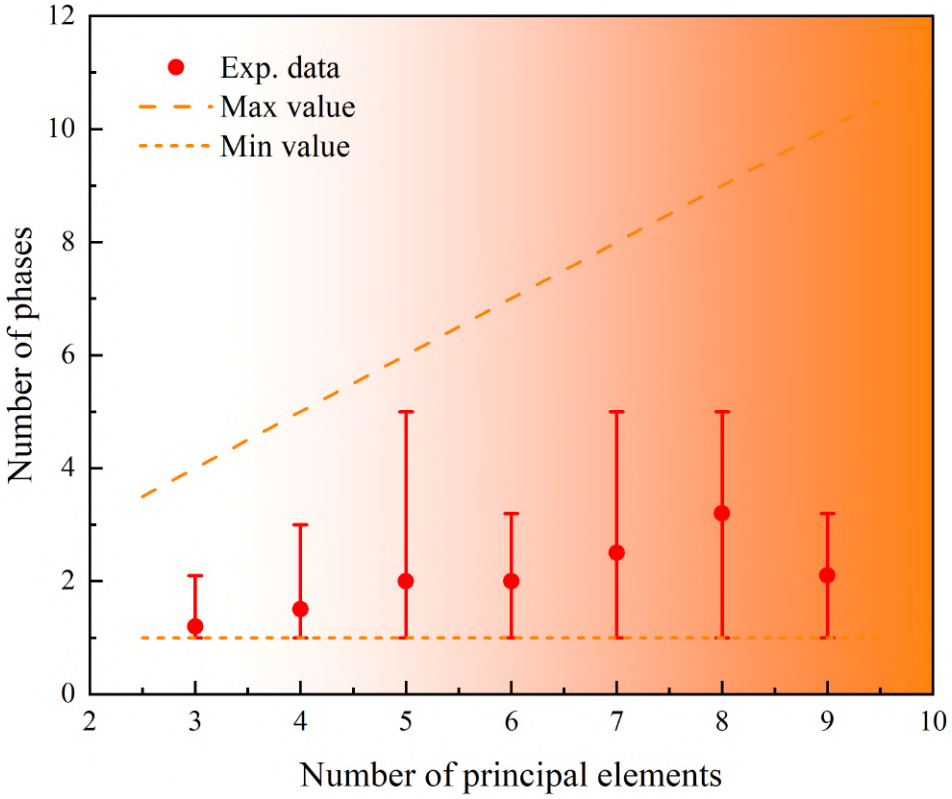

Figure 1.2: Relationship between the number of phases and the number of principal elements.

In addition, according to the equation of Gibbs free energy of systems:

$$\Delta G_{mix} = \Delta H_{mix} - T\Delta S_{mix} \tag{1.3}$$

where ΔG_{mix} is the Gibbs free energy, ΔH_{mix} is the mixing enthalpy, T is the absolute

temperature, and ΔS_{mix} is the mining entropy. The high configurational entropy in HEAs will reduce the Gibbs free energy and form a more stable phase structure. This has been confirmed in some experimental works, for example, the phase structure of the NbMoTaW and VNbMoTaW HEAs can remain unchanged after prolonged annealing at high temperature, indicating the ultra-high phase stability of HEAs [**21**], and the NbMoTaW HEA shows better stability than the refractory metal pure tungsten after being held at 1100°C for 3 days [**22**].

1.2.2 Severe lattice distortion effect

HEAs contain multiply principal elements in equal molar fraction, and it is generally believed that each element randomly occupies a crystal lattice position with equal probability [**3, 23**]. Therefore, HEAs can not distinguish solute and solvent atoms like traditional alloys. Moreover, there are differences in the atomic radius, crystal structure and electronegatively of each principal element, which results in the severe lattice distortion in HEAs. The lattice distortion in the structure can be expressed as the mean square deviation of the atomic radius difference in HEAs:

$$\delta = \sqrt{\sum_{i=1}^{n} c_i \left(1 - \frac{r_i}{\sum c_j r_j}\right)^2} \tag{1.4}$$

where $c_{i,j}$ is the molar fraction of element i and j, $r_{i,j}$ is the radius of element i and j, and n is the number of principal elements. When the lattice distortion δ is less than 6.6%, the alloy tends to form disordered solid solution structures, while when δ is large than 6.6%, the alloy tends to form complex structures such as intermetallic compounds. In other words, in order to reduce lattice distortion energy and maintain a balance of local atomic stress, it is necessary to adjust the relative position of lattice atoms, which leads to lattice distortion, as illustrated in **Fig. 1.3**.

In fact, this solid solution, which contains various atoms with difference size, in-

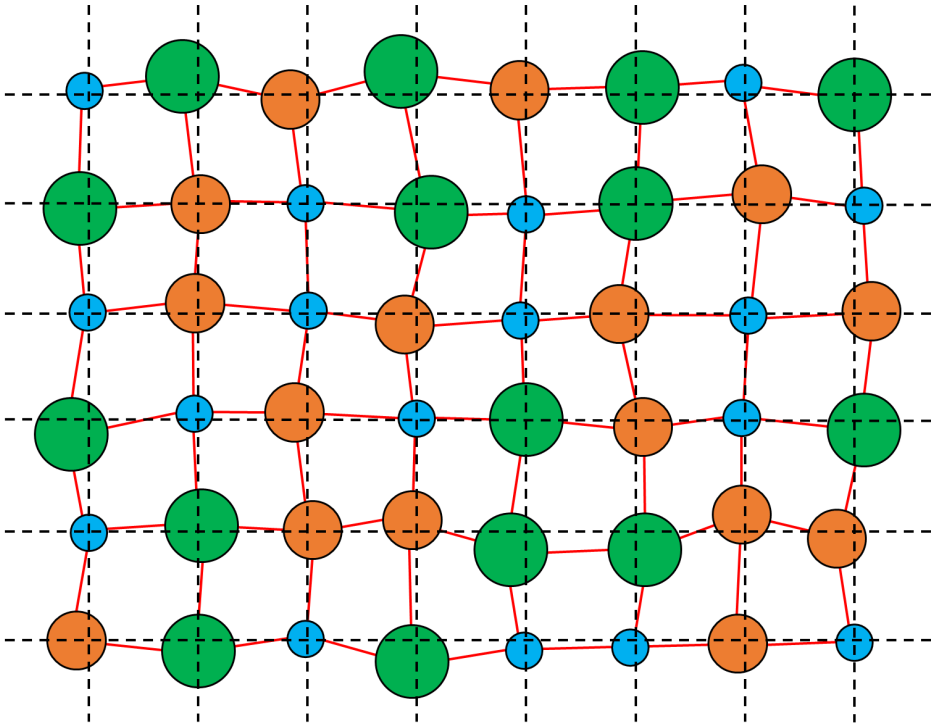

Figure 1.3: Schematic illustration of lattice distortion in HEAs.

evitably leads to lattice distortion effect. This effect has a significant impact on the mechanics, optic and thermodynamics of HEAs. For example, addition of a strong binding Al element to FeCoNi-based HEAs will promote the formation of the BCC phase, which will affect the resistivity [**24**]. In addition, the increase in lattice distortion energy and the adjustment of atomic positions can also reduce the stacking fault energy of HEAs [**25**]. Currently, there are many studies and views on lattice distortion effects in HEAs, and subsequent theoretical derivations and explanations are needed.

1.2.3 Cocktail effect

The multiple principal elements of HEAs have different characteristics and the interaction between different elements makes HEAs to exhibit a compound effect, i.e. the cocktail effect [**3**]. Therefore, the microstructure and properties of HEAs composed of elements with different properties are also different. The desired properties can be achieved by adjusting the principal elements and their properties of HEAs. For example,

if high tensile strength is required and no special requirements for hardness, elements with FCC structure can be considered when designing HEAs. If the material needs to be used in aerospace application, lightweight elements are considered as an alternative. If material is to be used in high temperature resistance environments, then refractory elements will be the first choice. It is important to notice that the properties of HEAs are not simply the sum of the individual principal elements, as the overall performances of HEAs depend not only on the properties of the individual principal elements, but also on the interaction between them. Therefore, the complex interactions between the principal elements have to be considered in the design of HEAs.

1.2.4 Sluggish diffusion effect

The severe lattice distortion and interactions between different principal elements in HEAs can seriously affect the diffusion between atoms. The diffusion of atoms in HEAs take place mainly through vacancy mechanisms [**18**]. During diffusion, each vacancy is surrounded by other kinds of atoms. The potential energy of the different lattice positions varies considerably, resulting in a high diffusion barrier as well as slow diffusivity. As shown in **Fig. 1.4**, if the potential energy will increase after vacancy migration, it indicates that the diffusion barrier is high and vacancy is difficult to move; If the potential energy will decrease after vacancy migration, the diffusion is hard to continue because of the trapping effect. A large number of lattice positions with different potential energies hinder atomic diffusion or act as traps for atomic diffusion. These lead to the sluggish diffusion effect in HEAs [**18, 26**].

Tsai et al. first investigated the diffusivity of different atoms in CoCrFeMnNi HEA by diffusion experiments. Their results indicated that the magnitude of the diffusivity were Mn > Cr > Fe > Co > Ni, and concluded that the diffusivity of atoms were related to the number of elements in the system [**26**]. The more the number of elements contained in the system, the slower the diffusion. However, Dabrowa et al. pointed out

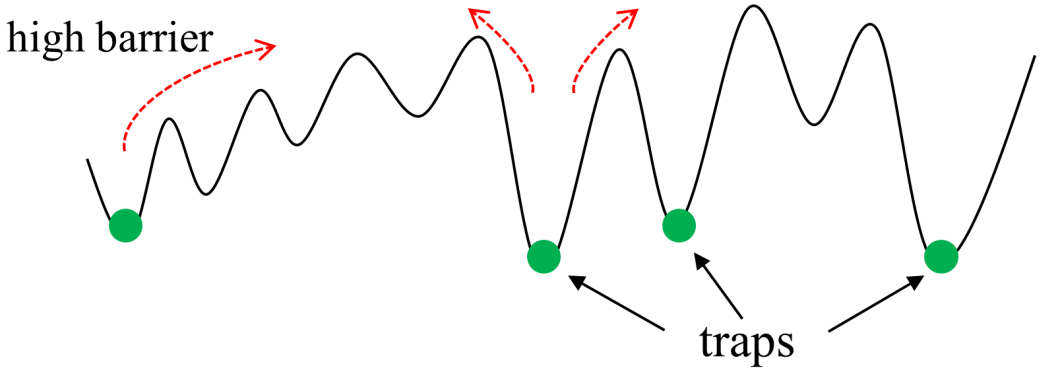

Figure 1.4: Schematic illustration of vacancy diffusion in HEAs.

that the sluggish diffusion phenomenon in HEAs is not directly related to the number of principal elements, but related to the specific element or structure. For example, a HEA contains Mn element may have a lower diffusivity, but in a HEA without Mn element the atomic diffusivity is still faster [**27**]. In addition, Vaidya et al. reported that atomic diffusion in CoCrFeNi and CoCrFeMnNi HEAs is not inevitably sluggish and can be even enhanced at a given absolute temperature [**28**]. All the results suggest that the sluggish diffusion effect in HEAs still needs further study.

1.3 Atomistic simulation methods

With the increasing demand for materials properties, the scale of research objects in materials science is constantly decreasing, and studying only micro scale structures can not reveal the essence of materials properties. Nano-structures, even atomistic-structures, has become the main content of materials research. Therefore, material research is increasingly relying on high-end testing techniques, the difficulty and cost of research are also increasing. Relying solely on experiments for material research is no longer sufficient to meet the research and development requirements of modern new materials. However, computer simulation technology can conduct multi-level research on materials from different scales based on relevant basic theories, and can also

simulate the service performance of materials in extreme environments such as ultra-high temperature and pressure, thereby achieving improvement and design of material properties. In this dissertation, the atomistic simulation methods used including the following three types: (1) first-principles calculations, (2) molecular dynamics simulations, and (3) Monte Carlo methods. In addition, (4) neural network potential was introduced, which can be used to more accurately describe interatomic interactions.

1.3.1 First-principles calculations

First-principles calculations, commonly referred to as first-principle calculation based on density function theory, also known as ab initio calculations, are a set of calculation methods used in materials science, chemistry, and physics to study material properties at the atomic and molecular level. The term "first-principles" means that these calculations are based on fundamental physical principles, such as the laws of quantum mechanics, and do not rely on any empirical or experimental data. The basic idea behind first-principles calculations is to use quantum mechanical equations to describe the behavior of electrons and nuclei in materials. By solving these equations, it is possible to calculate the properties of the materials, such as electronic structure, thermodynamic properties, and chemical reactivity. First-principles calculations are used to study a wide range of materials, from simple elements and small molecules to complex materials such as metals, semiconductors, and polymers. Before synthesizing or manufacturing new materials, they are particularly useful in predicting the properties of new materials, enabling researchers to design materials with specific properties for specific applications.

Density function theory (DFT), the core of first-principles calculations was proposed and proved by Kohn and Hohenberg in 1964 [**29**]. The theory mainly includes two points: 1, the ground state energy obtained from the Schrödinger equation is a unique function of electron density, that is, the ground state energy E can be expressed as

$E[n(r)]$, where $n(r)$ is the electron density. 2, the electron density of the ground state determines all properties of the ground state, the Schrödinger equation can be solved by finding the electron density function with three spatial variables, instead of solving the wave function with multiple spatial variables. In 1965, Kohn and Sham proposed the Kohn-Sham equation [**30**]:

$$\left\{-\frac{1}{2}\nabla^2 + \upsilon\left(r\right) + \int \frac{n\left(r'\right)}{|r-r'|}dr + \mu_{X_c}\left[n\left(r\right)\right]\right\}\psi_i\left(r\right) = \varepsilon_i\psi_i\left(r\right) \tag{1.5}$$

$$n\left(r\right) = \sum_{i=1}^{N}\left|\psi_i\left(r\right)\right|^2 \tag{1.6}$$

where the first term in **Eq. 1.5** is the kinetic energy of the electron, the second term is the interaction energy between the electron and all atomic nuclei, the third term is the Hatree potential energy, which represents the interaction energy between a single electron and the total electron density generated by all electrons, and the forth term is the exchange-correlation potential, this part is unknown and there is no definite expression.

After more than half a century of development, first-principles calculations method has been continuously improved with the effort of many researchers. Especially with the rapid development of new algorithms and the improvement of computing power, first-principles calculations is gradually becoming an important method for studying the evolution of materials with temperature and time.

1.3.2 Molecular dynamics simulations

Molecular dynamics (MD) simulations are the use of computer methods to represent statistic mechanics as an adjunct to experiments [**31**]. MD simulations are used to study the equilibrium and mechanical properties of complex systems that cannot be solved analytical method, and to build a bridge between theory and experiment. It occupies

an important position in the interdisciplinary fields of mathematics, biology, chemistry, physics, material science, and computer science. MD methods first require to establish equations of motion for a group of molecular in a system, and the fundamental process associated with the microscopic quantities of the system are studied by solving the equations of motion for all the particles and molecules. The rigorous solution of this multi body problem requires establishing and solving the Schrödinger equation of the system. According to the Born-Oppenheimer approximation, the motion of electrons is treated separately from the motion of nuclei. The motion of electrons is treated using quantum mechanics methods, while the motion of atomic nuclei is treated using classical dynamics methods. In this case the motion of nuclei and particles satisfies classical mechanical laws, described by Newton's laws, which is a good approximation for most materials.

In short, MD method deals with the motion of particles following Newton's equations:

$$\boldsymbol{F}_i(t) = m_i \boldsymbol{a}_i(t) \tag{1.7}$$

where $\boldsymbol{F}_i(t)$ is the force exerted on the particle i at time t, m_i is the mass of particle i, and $\boldsymbol{a}_i(t)$ is the acceleration of the particle i at time t. The force $\boldsymbol{F}_i(t)$ can be calculated using the first derivative of the potential energy over the coordinate $\boldsymbol{r}_i$, that is $\boldsymbol{F}_i(t) = -\frac{\partial U}{\partial \boldsymbol{r}_i}$, where U is the potential energy function. Therefore, for a system containing N particles, each particle has the following relationship:

$$\begin{cases} m_i \frac{\partial \boldsymbol{v}_i}{\partial t} = \boldsymbol{F} = -\frac{\partial U}{\partial \boldsymbol{r}_i} + \cdots \\ \dot{\boldsymbol{r}}(t) = \boldsymbol{v}(t) \end{cases} \tag{1.8}$$

where $\boldsymbol{v}$ is the velocity vector, m_i is the mass of particle. Therefore, to solve this equation set, it is necessary to give the initial coordinates and velocities of each particle in the system. The flow of MD simulation is shown in **Fig. 1.5**, the input information

includes potential functions for the interaction between atoms or particles. If the properties of thermodynamic equilibrium states are to be considered, other conditions such as temperature and pressure need to be input. Then, under the input information, the motion equation of the system particles is solved. If the atomic coordinates obtained at each moment are statistically calculated, relevant thermodynamics information of the system can be obtained. If the atomic velocities at each moment are statistically calculated, the dynamic properties of atoms can be obtained.

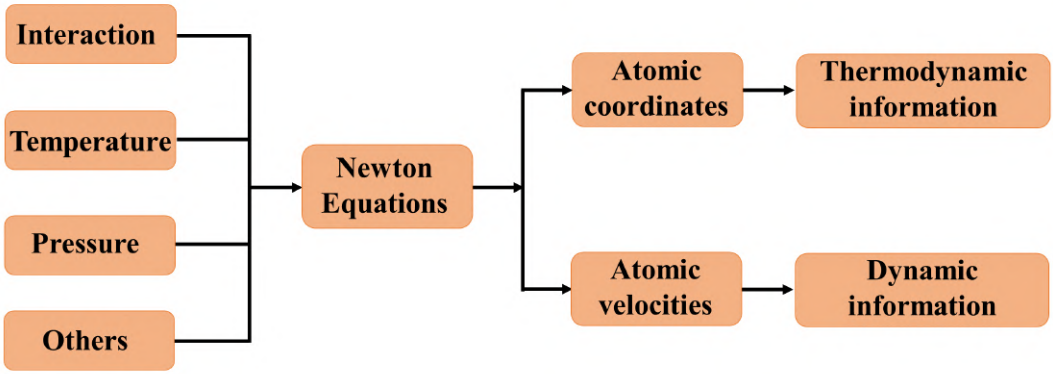

Figure 1.5: Working principle diagram of molecular dynamics

1.3.3 Monte Carlo method

Monte Carlo (MC) method is based on simple theoretical criteria, such as simple interaction between substances and the environments, using repeated random sampling to solve complex system problems [**32**]. This method uses a random sampling technique to simulate the probability and statistical problems of objects. By designing appropriate probability models, this method can also solve deterministic problems, such as definite integrals. With the rapid development of computers, MC methods have been applied in physics, chemistry, materials, biology, sociology, and economics. The basic idea of MC method is to establish an appropriate probability model or random process in order to solve a problem, so that its parameters, such as the probability of events, and the

mathematical expectation of random variables, are equal to the solution of problem. Then a random sample of the model or process is tested several times, and the results are statistically analyzed. Finally, the required parameters are calculated to obtain an approximate solution to the problem.

In the application of material science, the MC method can simulate the state of atoms and molecules that constitute the fundamental particles of materials through random sampling, eliminating the complex calculation of quantum mechanics and molecular dynamics, which allows to simulate large systems. Combined with the methods of statistic physics, MC can establish the relationship between the states of elementary particles and the macroscopic properties of materials, and is an important tool for studying the nature of material properties and factors that influence them. In addition, if the MC method is used to simulate the state change of multi-particle system, and the energy of the new and old system is not used to determine the trade-off between the new and old states, but rather is judged based on the barrier, the dynamic process of the system can be simulated. This method is called kinetic Monte Carlo (kMC). The main characteristics of kMC method are the introduction of the concept of time and only consider a few basic reactions. Compared to MD simulation, this method has larger simulation system and longer simulation time scale.

1.3.4 Neural network potential

The quality of the simulation results and the accuracy of the prediction of material properties depends crucially on the reliability of the interactions described between atoms. The DFT calculation provides an accurate description of interatomic interactions in terms of electronic structure. However, its high computational cost limits the model to a few hundred atoms. The MD and MC simulations can be applied to large scale models to investigate material properties, but the accuracy of the potential describing interatomic interactions is an important issue. With the development of

machine learning, attempts have been made to construct new potentials to describe the interatomic interactions more accurately. The artificial neural networks have become a promising approach to constructing new potential. The neural network potential (NNP) is developed by DFT training database [**33**]. Its accuracy is comparable to that of DFT calculations, while it can also be performed with faster efficiency in large scale models. In this dissertation, we construct a NNP potential based on the DFT calculation results through machine learning, which allows the discovery of new chemical ordering structures in CrCoNi MEA, and investigate their effect on the properties of materials [**34**].

1.4 Key issues and structure of this dissertation

With the increasing demand of energy, it is urgent to develop new types of energy. Traditional energy sources such as oil, coal, and natural gas have limited storage, while renewable energy sources such as hydropower, solar power, and wind energy are constrained by geographical and environmental conditions, making them difficult to become new energy alternatives. Nuclear energy, as a clean, economical, and reliable energy source, has great potential for development in the future. The development of nuclear energy technology also puts forward higher requirements for nuclear structural materials. The new generation of nuclear structural materials needs to be able to work stably under extreme conditions, such as high radiation, high load, and high temperature for a long time. With continuous deepening of research on the properties of HEAs, a lot of works has shown that the lattice distortion and sluggish diffusion effects of HEAs can limit the migration of radiation defects. In addition, due to the present of high atomic level stresses, HEAs have a self repairing mechanism. Therefore, HEAs have excellent radiation resistance and are expected to become the next generation of nuclear structural materials.

However, up to now, the mechanism of radiation resistance of HEAs has not been fully understand, especially the movement mechanism of defects after radiation damage still needs further study. In addition, conduction radiation experiments in the reactor has certain risk and high costs, while studying the radiation resistance of HEAs through simulation methods has more advantages. Based on the above background, this paper simulated the radiation resistance and dynamics behavior of internal defects of HEAs. The main content includes the following parts:

In Chapter 2, the surface radiation resistance of CoNiCrFeMn HEA was studied, and the internal defects (including interstitial, vacancy and dislocation) evolution and migration behavior after radiation damage was investigated. The radiation resistance of CoNiCrFeMn HEA and pure Ni was discussed.

In Chapter 3, the chemical ordering effect on the radiation resistance of CoNiCrFeMn HEA was considered. By using the hybrid MD-MC simulation, chemical short range order was identified in HEAs and its effect on the radiation damage and interstitial diffusion behavior were investigated. A radiation damage - diffusion healing competition model of chemical ordering was established to better control the chemical ordering enhanced radiation resistance effect in HEAs.

In Chapter 4, chemical domain structure was investigated in CrCoNi MEA, and its effect on interstitial diffusion behavior was discussed. In addition, sluggish diffusion phenomenon has been confirmed by simulation in CrCoNi MEA, and the relationship between chemical domain structure and sluggish diffusion effect was investigated.

In Chapter 5, the main results of this dissertation were summarized, and the prospects and problems of the application of H/MEAs in nuclear structure materials and other broader fields were discussed.

Chapter 2

Surface radiation damage and internal defects evolution in CoNiCrFeMn high entropy alloy

2.1 Introduction

With the development of next generation nuclear energy, the working environment of nuclear structural materials becomes severe. It is urgent to develop new structural materials with better radiation resistance performance [**35, 36**]. Among many candidates, HEAs is one of the most promising material because of the excellent properties, the complexity of compositions in HEAs might enhance irradiation tolerance under server irradiation environments [**14, 37–41**]. In contrast to traditional alloys, which contain only one or two principal elements, an HEA contains five or more principal elements; the properties of HEA can also be greatly improved by adjusting the types and proportions of elements [**42–46**]. HEAs represent a fundamentally new alloy design concept with a broad variety of potential applications. Many research results showed that HEAs had excellent mechanical properties, good ductility at low temperatures as well as high strength at high temperatures, and excellent corrosion and wear resistance, which also are helpful for the application as nuclear structural material [**2, 8, 9, 47**]. Recently, researchers have actively explored HEA performance in radiation damage, with several results indicating that HEAs show better radiation resistance than traditional alloys. For instance, a tungsten-based HEA was developed and showed no sign of induced dislocation loops after irradiation experiments. Furthermore, nanoindentation results of radiation-damaged materials also showed only a slight increase in hardness [**48**]. Some irradiation simulation analyses demonstrated that this sluggish diffusion effect is a key factor in HEAs' radiation resistance [**17, 26, 40, 49, 50**], while there also remained some disputes about this effect in HEAs [**51, 52**]. Hyeon-Seok et al. also investigated the generation and evolution of point defects in HEA, their results indicated that defect clusters appearing in the HEA were unstable owing to alloy complexity, and the lattice distortion of HEA could result in a relatively limited collision space and a high recombination rate of defects [**16**]. Chen et al. investigated the diffusion and formation of helium bubbles to valid whether HEA had an excellent

helium irradiation resistance performance under helium implantation [**53**]. Chen et al. studied the structure and phase stability of HEA under irradiation and explored the microstructure and chemical composition dependence of irradiation tolerances [**54**]. Although researchers have done significant work on the irradiation resistance behavior and other properties of HEAs, however, there are still many issues to be solved. For example, the surface radiation resistance of HEAs, the radiation damage defects evolution during continuous bombardments, and migration of defects in HEAs had not been systematically studied, especially the dynamic behavior of interstitial clusters and vacancy defects were rarely paid attention.

A variety of high-energy particles will be produced in the nuclear reactor during operation. The primary issue for the structural materials is direct exposure to high-energy particle bombardment [**55**]. The surface irradiation resistance of structural materials is therefore very important. In addition, under high temperature and high energy irradiation working environment, a large number of interstitial and vacancy defects are also generated inside the materials [**56**]. The migration of interstitial clusters decreased the possibility of trapping vacancy defects and annihilation, and the aggregation of vacancies could lead to the collapse of vacancies to form dislocation loops, which reduced the stability of structures and shortened the life of materials [**50, 57**]. Mohammad et al. studied the effect of chemical alternation on the irradiation resistance. The results showed that increasing the complexity of alloy led to the decrease of defect mobility [**58**]. Lu et al. indicated that controlling the defects mobility and migration pathways could enhance irradiation tolerance, and the complexity of high entropy alloys allowed it to be a promising anti-irradiation material [**40**]. Zhao et al. pointed out that the growth of vacancy clusters could be suppressed by controlling cluster migration pathways and diffusion kinetics [**59**]. Levo et al. showed that increasing complexity of alloys did not always decrease the accumulation of damage. The evolution of defects and transformation of dislocation might be the key factor [**50**]. Therefore, controlling the formation

and migration of defects was the key to improve the irradiation tolerance of materials.

CoNiCrFeMn HEA has been reported to process good properties such as high strength at high temperature, excellent corrosion and wear resistance. It has attracted extensive attention in nuclear energy due to the outstanding irradiation resistance, partially owing to the sluggish diffusion. In this chapter, we will focus on the surface bombardment resistance of CoNiCrFeMn HEA at extreme irradiation flux [**60**]. In addition, since and the irradiation damage inside the CoNiCrFeMn HEA is still unclear and the dynamic behavior of interstitial clusters and vacancy defects in CoNiCrFeMn HEA under severe working conditions has not been given much attention, this chapter will also investigate the accumulation and evolution of defects in CoNiCrFeMn HEA during high energy continuous bombardments at high temperature, and compares it with pure Ni. Finally the migration energies of interstitial and vacancy in CoNiCrFeMn HEA are calculated, and the mean free path of interstitial cluster and the migration behavior of vacancy defects are discussed [**49**].

2.2 Simulation method and model details

2.2.1 Surface radiation simulation

For the surface radiation simulation, the two models, pure Ni and CoNiCrFeMn HEA are shown in **Fig. 2.1**. The number of Ni atoms in the model is 17,280. In CoNiCrFeMn HEA model, five types of atoms are equally proportional and randomly distributed, with a total number of the atoms of 17,280. The dimensions of both models are the same, 4.23, 4.23, and 10.56 nm along x, y, and z directions, respectively. The Ni atom is chosen as the incident atom as it is a component of both the Ni and CoNiCrFeMn HEA. Two layers of atoms at the bottom of the sample box in two models are fixed to avoid the motion caused by the momentum from the incident Ni atoms. In order to prevent the atoms from bombarding the same surface position, the incident Ni

atoms are generated with random orientation and position in a 0.2 nm thick vacuum layer, which is 2 nm away from the top surfaces of models, and then bombarded into the models.

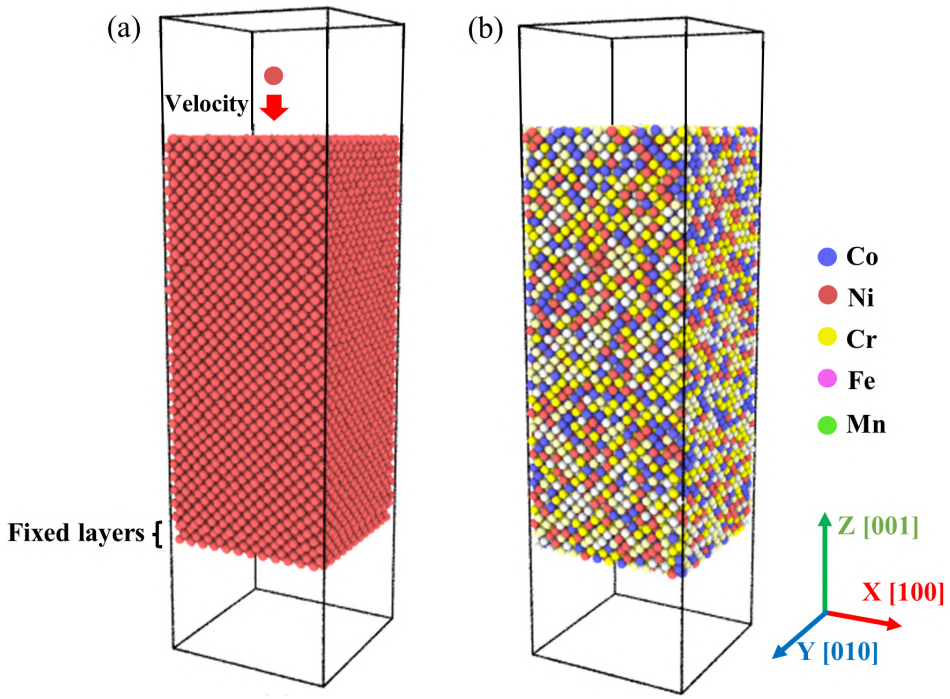

Figure 2.1: Surface radiation simulation models of pure Ni and CoNiCrFeMn HEA.

The second nearest-neighbor modified embedded-atom method (2NN MEAN) potential is used to describe the interatomic interaction in CoNiCrFeMn HEA as well as pure Ni [**61**]. In order to correctly describe the short-range interatomic interaction in the cascade for high-energy atomic collisions, the d-parameter of Co and Mn are adjusted from 0 to 0.03 and 0.02, respectively. Do et al. had shown that the variation of the d-parameter is sufficient for the short-range repulsion during atomic collisions and has little effect on the physical properties in each unary system [**16**]. All the MD simulations are conducted by large-scale atomic/molecular massively parallel simulator (LAMMPS) code [**62**]. Prior to the radiation bombardment simulations, the simulation systems are annealed with the NPT ensemble. The timestep is 0.001 ps, the annealing process is as follows: First, the simulation system is relaxed at 300 K for 100 ps,

then, the temperature is heated to 1200 K at 3.4 K/ps and hold for 1000 ps to reach equilibrium, finally, the temperature is cooled to 300 K at 3.4 K/ps. The radiation bombardment simulation is conducted with the NVE ensemble, which uses a adaptive timestep such that each atom moves no more than 0.002 nm per step. The radiation bombardment energy is 3000 eV as it is high enough to cause a large number of defects and will not penetrate the models, and temperature of system 700 K is chosen to simulate the serious high temperature working conditions. Berendsen thermostat is applied to the atoms with a thickness of 0.5 nm on each side of the model to avoid excessive thermal energy in the model during the radiation bombardment process [**63**]. OVITO visualization tool is used to analyze trajectories of all the atoms, and Wigner-Seitz (WS) method and common neighbor analysis (CNA) method are used to identify and count the number of defect atoms [**64**–**66**].

2.2.2 Internal radiation and defects evolution simulations

For the internal radiation simulation, the pure Ni and CoNiCrFeMn HEA models are also shown in **Fig. 2.2**. In the Ni model, the number of Ni atoms is 32,000. In the HEA model, five types of atoms in CoNiCrFeMn HEA are equally proportional and randomly distributed with the total number of 32,000 atoms. The two models both had a size of 7.06 nm in x, y, and z directions, respectively. Periodic boundary conditions were applied along x, y and z directions. Since short-range order (SRO) of HEA is critical to the physical properties of HEAs, therefore, we calculate the SRO parameters for all possible nearest neighbor bonds to check the randomness of five different elements [**67**]. Details of SRO parameter calculation results are presented in the **Tab. 2.1**. The closer the SRO parameter is to 0, the more randomly distribution the atoms. The results show that five types of atoms in the CoNiCrFeMn could be regarded as a random distribution. In the next chapter, we will focus on the SRO effect on the radiation resistance of HEA. In order to simulate a homogeneous irradiation effect and random

bombardments, the simulation cell was randomly shifted after each cascade collision, and then the irradiation atom was selected in the center of the simulation cell with an energy of 3000 eV, single PKA (Primary Knock-on Atom) process had been taken to confirm that the box was big enough for the energy of 3000 eV. The temperature at 700 K was adopted to mimic the severe working environment [**68**].

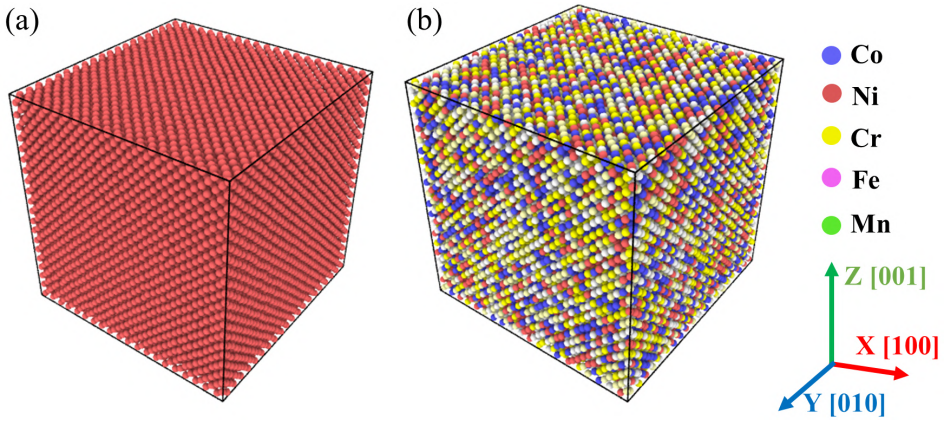

Figure 2.2: Internal radiation simulation models of pure Ni and CoNiCrFeMn HEA.

Table 2.1: Short-range order parameter of different element pairs

Element	Co	Ni	Cr	Fe	Mn
Co	-0.0114	-0.0029	0.0061	0.0067	0.0006
Ni		-0.0135	-0.0024	0.0043	0.0141
Cr			0.0095	-0.0034	-0.0075
Fe				-0.0072	0.0006
Mn					-0.0070

The same 2NN MEAM potential is used to describe the interatomic interactions among Co, Ni, Cr, Ni and Mn atoms. Before the internal cascade collisions simulation, the models are annealed under NPT ensemble with a time step of 0.001 ps. The annealing process is the same as in the previous surface radiation simulation. Also, Berendsen thermostat was applied to control the irradiation temperature $T = 700$ K of the 0.5 nm thick layers at all sides of the matrix to avoid excessive temperature. In addition, the intervals between two adjacent cascade events was 50 ps to make the temperature of system cool down to about 700 K and ensure defect clusters migration

have all finished. For point defects analysis, we still use the WS and CNA methods to calculate the sum of defects, the dislocation extraction algorithm (DXA) method is applied to analyze the dislocation distribution in the models [**69**].

2.3 Results and discussion

2.3.1 Surface radiation resistance in a single bombardment

During the PKA process, there are a series of events, such as cascade collision, the formation and relaxation of displacement spike, and the cooling of system to the ambient temperature. The point defects were produced and reached the peak due to the bombardment. Then the recombination of interstitial and vacancy occurred, and only a small part of point defects remained. To analyze point defects, the WS was applied to calculate the number of interstitial and vacancy. The relaxed Ni and CoNiCrFeMn matrix were taken as the reference structures for WS analysis. **Fig.2.3** showed the generation and evolution of defects in the two models during one typical PKA process, which lasted for about 10 ps. In the beginning of PKA, the number of defects in Ni and the CoNiCrFeMn HEA both increased rapidly due to the cascade collision, and reached a peak at around $t = 0.3$ ps. Then the kinetic energy and potential energy generated through cascade collision were randomly dissipated and converted into heat energy. The displacement collision, the movement and annihilation of defects all occurred at 0.3 - 3 ps. Furthermore, the number of defects gradually decreased, and the system cooled down to the ambient temperature. Finally, most of the defects caused by cascade collision were restored, and a small part of the defects remained inside the matrixes. The fraction for the defects that remained in the Ni matrix and CoNiCrFeMn HEA to the defects in peak were 24.8 % and 18.6 %, respectively. Multiple PKA simulations were carried out to obtain the statistics value of defects. The average interstitial and vacancy defects remained in the CoNiCrFeMn HEA were 11 ± 3 and 13 ± 3, respectively. The

unequal number of the interstitial and vacancies was attributed to the fast migration of interstitial to the surface. The average interstitial and vacancy defects remained in Ni were 21 ± 4 and 26 ± 5, respectively, which were substantially larger than those in the HEA.

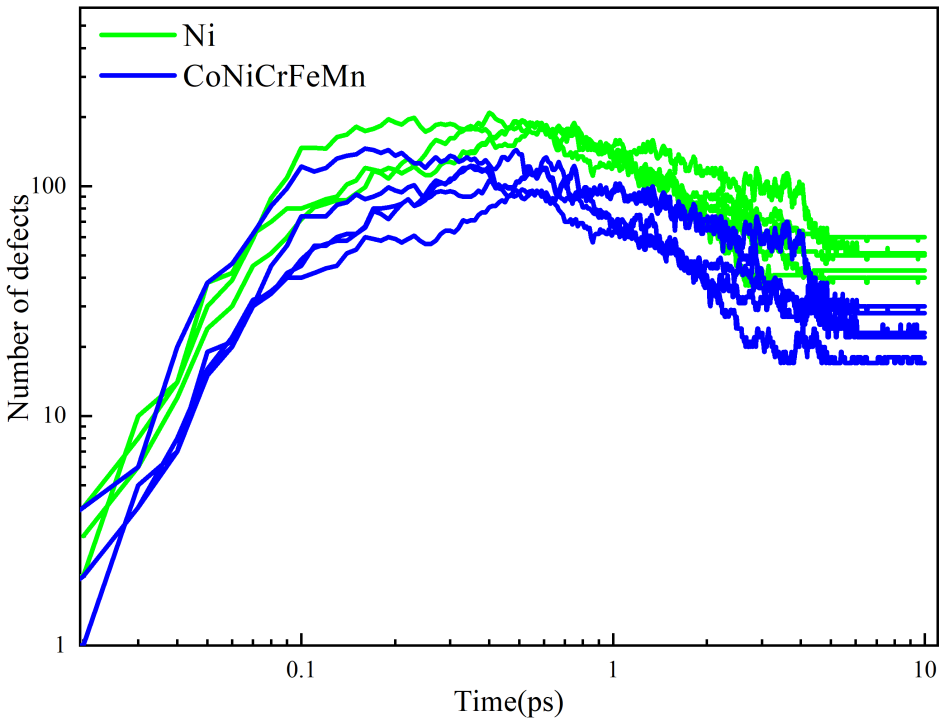

Figure 2.3: The number of defects in Ni and CoNiCrFeMn HEA during PKA process.

The distribution of kinetic energies of atoms in the Ni and CoNiCrFeMn HEA and the number of defects with the depth are shown in **Fig. 2.4**. When the displacement spike formed at $t = 0.3$ ps, the depth of cascade collision in Ni almost reached the bottom, as shown as **Fig. 2.4 (a)**. The distribution of defects versus the depth at $t = 0.3$ ps in Ni was shown in **Fig. 2.4 (b)**. Most defects remained in the deeper part of the Ni. However, in the CoNiCrFeMn HEA, as shown as **Fig. 2.4 (c), (d)**. Because of the effect of sluggish diffusion, the cascade collision was suppressed, and the cascade collision occurred mainly in the middle part of the matrix. Even at the displacement spike time $t = 0.3$ ps, radiation damage was still in the shallow part of CoNiCrFeMn HEA. Therefore, CoNiCrFeMn HEA could effectively reduce the number

of defects produced during the surface high-energy particles bombardment and can also suppress the radiation damage areas in shallower regions of models. We can conclude that CoNiCrFeMn HEA had much higher surface irradiation resistance to the energetic particle bombardment than Ni.

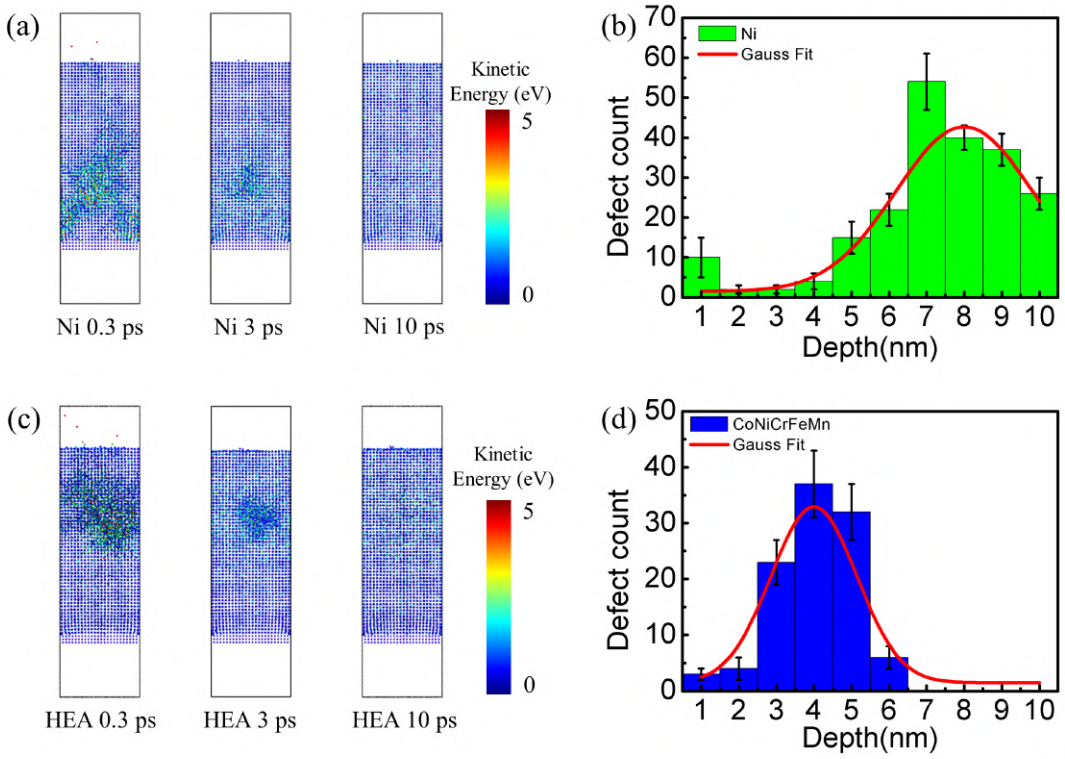

Figure 2.4: Kinetic energy distribution of atoms in (a) Ni and (c) CoNiCrFeMn HEA at $t = 0.3$ ps, 3 ps and 10 ps, respectively. The distribution of defects in (b) Ni and (d) CoNiCrFeMn HEA at $t = 0.3$ ps, when the displacement spike occurred.

2.3.2 The irradiation flux effect in surface bombardment

In this section, we will focus on the continuous radiation bombardments in Ni and CoNiCrFeMn HEA to evaluate the radiation resistance of two materials. As discussed in last section, $t = 0.3$, 3 and 10 ps are the crucial time for the evolution of defects in PKA process. Therefore, when the models are subjected to continuous radiation bombardments, time interval of $\Delta t = 0.3$, 3 and 10 ps are chosen, which correspond to the irradiation flux of 1.68×10^{29} n/(m^{2}s), 1.68×10^{28} n/(m^{2}s), and 5.59×10^{27}

n/(m^2s), respectively. 300 continuous radiation bombardments are carried out.

When the irradiation flux is 5.59×10^{27} n/(m^2s), the number of point defects caused by radiation bombardments is shown in **Fig. 2.5 (a)**. For pure Ni, the defects gradually increased during the irradiation process, finally reaching 631 defects. FurtherMore, a sharp increase in the number of defects was observed after 90 continuous bombardments. The number of defects in CoNiCrFeMn HEA shows a different trend. The defects increased slowly and finally remained relatively stable. After 300 continuous bombardments, the number of defects was only about 210. These results show that CoNiCrFeMn HEA has stable and fewer defects than pure Ni under continuous high irradiation fluxes. When the irradiation flux is enhanced of 1.68×10^{28} n/(m^2s), the number of defects in Ni and CoNiCrFeMn HEA during continuous bombardment is shown in **Fig. 2.5 (b)**. Similar to the case of irradiation flux was 5.59×10^{27} n/(m^2s), a sharp increase in defects occurs for pure Ni at about 70 bombardments, and then the number of defects gradually increase to more than 850. For CoNiCrFeMn HEA, the number of defects increases slowly and eventually stabilises at around 224. The result indicated that CoNiCrFeMn HEA exhibited stable performance even at extreme irradiation fluxes. In addition, when the irradiation flux increased to 1.68×10^{29} n/(m^2s), the second bombardment started just after the displacement spike formed in the initial PKA and the system had no time to relax. A large void formed in the middle of model and model rapidly swelled and failed. The pure Ni can withstand 5 times of extreme high flux bombardments and the CoNiCrFeMn HEA can withstand 12 times of extreme high flux bombardments. The details of the failure models are provided in **Fig. 2.6**.

The different behaviors of Ni and CoNiCrFeMn HEA under continuous bombardments can be attributed to the ability of migration and accumulation of defects in materials. Since CoNiCrFeMn HEA contains five elements, the different atomic sizes cause large lattice distortion and sluggish diffusion effect, resulting in a severe impact on the effective diffusion rate between atoms and an effective suppression of defect migration.

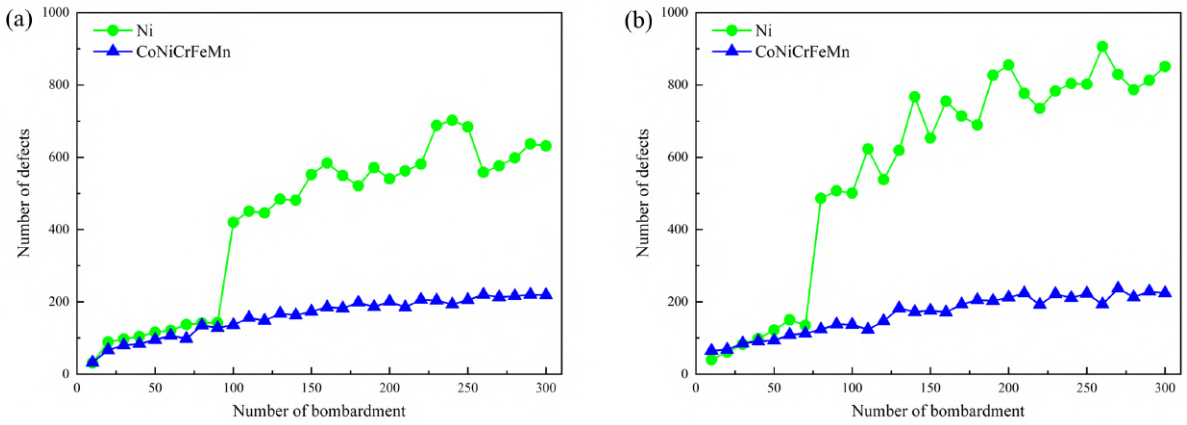

Figure 2.5: The number of defects in Ni and CoNiCrFeMn HEA during continuous bombardments at the irradiation flux of (a) 5.59×10^{27} n/(m^{2}s) and (b) 1.68×10^{28} n/(m^{2}s).

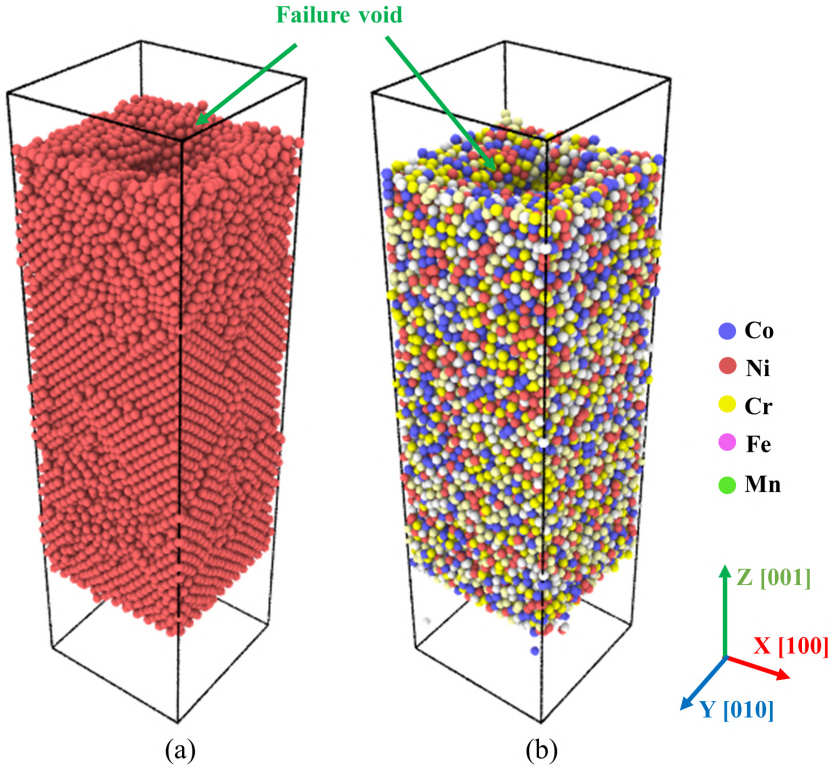

Figure 2.6: The failure of Ni and CoNiCrFeMn HEA models after extreme high flux of 1.68×10^{28} n/(m^{2}s) bombardments.

Therefore, the number of defects in CoNiCrFeMn HEA after radiation bombardments increased slowly and remained relatively constant. In addition, in order to find out the reason for the sharp increase of defects in Ni during bombardment, we investigate the defects evolution results in Ni when the sharp increase occurred. **Fig. 2.7 (a), (b)** shows the results at different irradiation flux, the formation of dislocation could be observed in Ni. The formation and sliding of the dislocations produced a large number of surface defects and dislocation loops inside Ni, which led to the sharp increase of defects. The the interstitial and vacancy distribution of Ni and CoNiCrFeMn HEA after 300 continuous bombardments at the irradiation flux of 5.59×10^{27} n/(m^{2}s) and 1.68×10^{28} n/(m^{2}s) are shown in **Fig. 2.7 (c), (d)**. The defect distribution in CoNiCrFeMn HEA is dispersed, which is quite different from the concentrated distribution of defects in Ni. In addition, two distinct interfaces of stacking fault can be observed inside the pure Ni, the rapid evolution of defects inside Ni after surface radiation bombardments results in the worse radiation resistance of Ni.

2.3.3 Internal defects and dislocation generation

The surface radiation results show that the evolution of defects produced inside the models by the radiation bombardments has a significant effect on the radiation resistance. Therefore, we next focus on the evolution of defects. In order to introduce radiation defects inside the models, internal atoms were selected as the bombardment particles and 300 continuous radiation bombardments were performed. The WS method was also used to calculate the number of defects. As shown in **Fig. 2.8 (a)**, the number of defects in Ni increased rapidly to approximately 300 at the start of continuous bombardments and remained increasing for a long time as the cascade collisions continued. After 300 cascade collisions, the number of defects reached over 950. **Fig. 2.8 (b)** shows the number of interstitial clusters in different size in Ni after 50, 100, 150, 200, 250, and 300 cascade collisions. Two distinct phenomena are observed. Firstly,

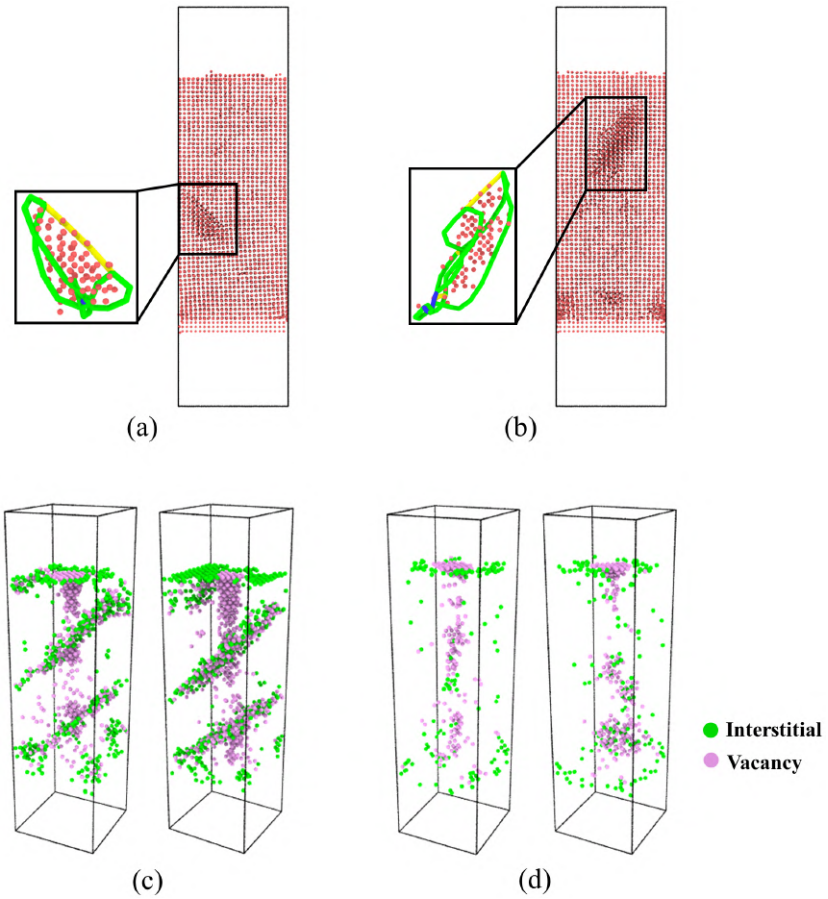

Figure 2.7: The formation of dislocation in Ni after (a) 90 times of bombardment at the irradiation flux of 5.59 $\times$ 10^{27} n/(m^{2}s) and (b) 70 times of bombardments at the irradiation flux of 1.68 $\times$ 10^{28} n/(m^{2}s). The blue, green, and yellow lines represent the Perfect, Shockley, and Hirth dislocation loops, respectively. (c) and (d) are the defects distribution in Ni (left) and CoNiCrFeMn HEA (right) after 300 times of bombardments at two irradiation fluxes.

the average number of small-size cluster (atoms number between 1 to 10) changes significantly, which implies that the migration of small-size clusters is vary active, and new clusters are gradually formed. Secondly, large-size cluster (atoms number over 51) appeared in Ni through the continuous cascade collisions. The formation of a large number of dislocation loops may occur when point defects aggregate into large-size cluster [**50, 70**]. In summary, these phenomenon suggest that defects generated by cascade collisions undergo significant migration and aggregation in Ni. **Fig. 2.8 (c)** is the number of defects in CoNiCrFeMn HEA, which shows a clearly different trend to that of

Ni. The number of defects remains stable throughout the cascade collision. Its number of about 400 is smaller than the value in Ni after 300 continuous cascade collisions. In addition, the interstitial cluster in different size between CoNiCrFeMn HEA and Ni is also very different, as shown in **Fig. 2.8 (d)**. The interstitial are mainly existed as small-size cluster and the defect cluster size distribution does not change significantly during continuous cascade collisions, indicating that the defects in CoNiCrFeMn HEA are relatively dispersed and no large-scale migration and aggregation occurs. The different defects behavior may be due to the lattice distortion and sluggish diffusion effects of CoNiCrFeMn HEA, which can successfully inhibit the migration of defects and promote the recombination of interstitial and vacancy, as suggested in the experiments [**26, 71**]. This trend is also similar to the previous surface radiation simulation, and the rapid increase in the number of defects in Ni could also be due to the behavior of dislocation, so we next analyzed the dislocation loops in both models.

Fig. 2.9 and **Fig. 2.10** show the evolution of dislocation in Ni and CoNiCrFeMn HEA after 50, 100, 150, 200, 250, 300 cascade collisions, respectively. In the Ni, a large number of dislocation loops are formed during continuous cascade collisions, especially the Frank loops keep growing throughout the process. After 300 cascade collisions, the long dislocation loops remain in the Ni. However, most of the defects are present as small-size cluster in CoNiCrFeMn HEA and few defects are observed to form dislocation loops. The surface radiation results have also shown that the present of dislocation loops is rarely observed in CoNiCrFeMn HEA. This suggests that interstitial or vacancy defects in Ni are more likely to aggregate or collapse to form dislocation loops, whereas the formation and growth of dislocation loops in CoNiCrFeMn HEA is significantly inhibited.

In order to further analyze the defects and dislocation loops during continuous cascade collisions, the total length of dislocations and the average length of dislocation loops in Ni and CoNiCrFeMn HEA are calculated separately. As shown in **Fig. 2.11**

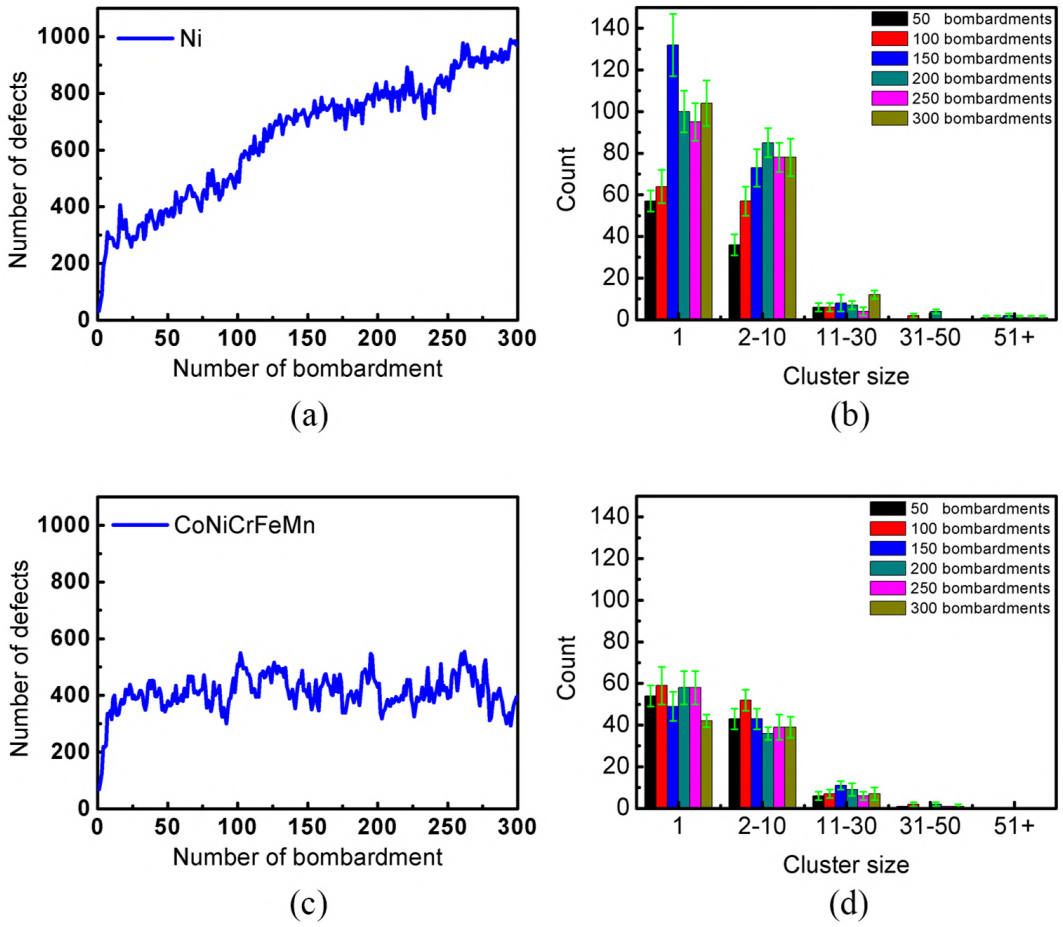

Figure 2.8: The number of defects in (a) Ni and (b) CoNiCrFeMn HEA models during continuous cascade collisions. The number of interstitial cluster in different size in (c) Ni and (d) CoNiCrFeMn HEA.

(a), a large number of dislocation loops are formed in the Ni at the beginning of the continuous cascade collisions and the total dislocation length remains at a high level of more than 40 nm for most of the time of continuous cascade collisions. Finally, only a large Frank loop survives with a total length of 20 nm due to the absorption of dislocation loops. **Fig. 2.11 (b)** shows the average dislocation length, which is stable and remain at a relatively low level for most of the time of continuous cascade collisions in both Ni and CoNiCrFeMn HEA. However, as the absorption and combination of dislocation loops in Ni, the average length of dislocation loops eventually reaches over 18 nm and the size of the dislocation loops increases significantly. As for the CoNiCrFeMn HEA, the growth of dislocation loops is suppressed throughout the continuous cascade

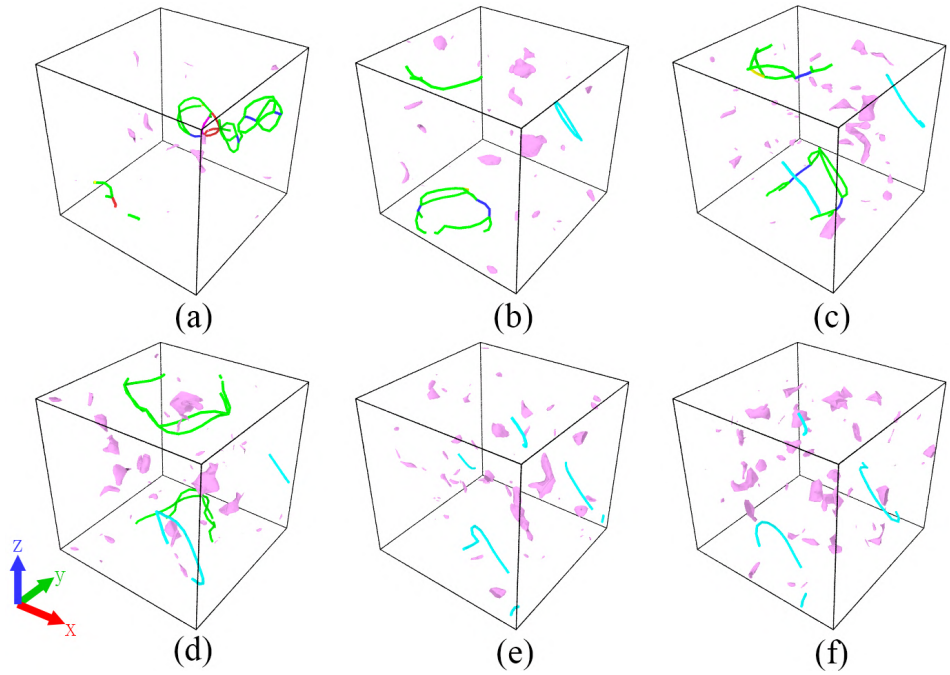

Figure 2.9: (a) - (f) Defects and dislocation loops distribution in Ni after 50, 100, 150, 200, 250, 300 cascade collisions, respectively. The different colored lines represent the different types of dislocation loops, where blue, green, purple, yellow, light blue represent the Perfect, Shockley, Srair-rod, Hirth, and Frank dislocation loops, respectively. The pink meshes are defect clusters

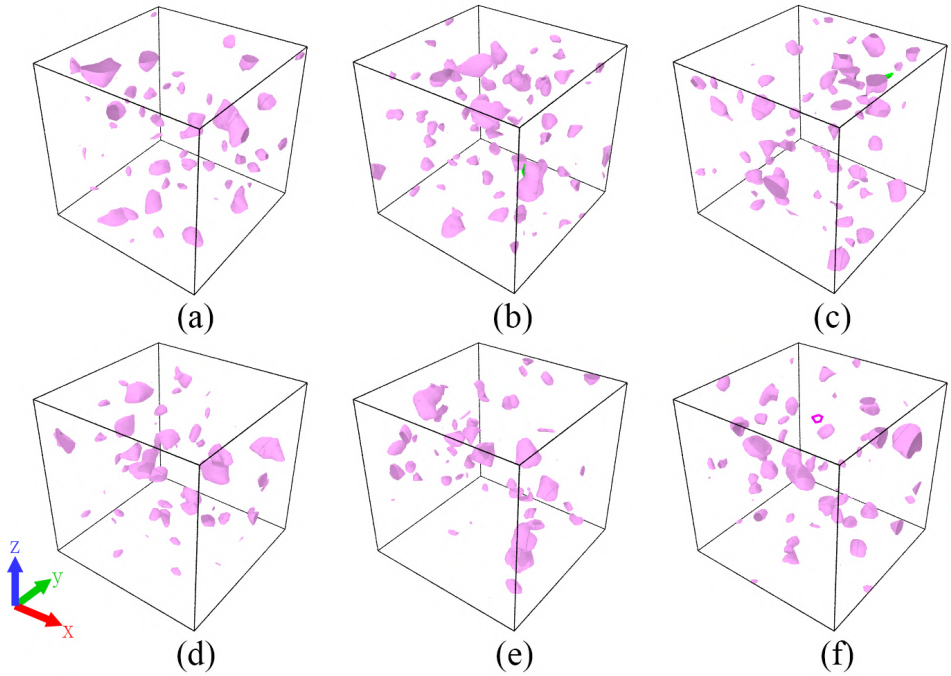

Figure 2.10: (a) - (f) Defects and dislocation loops distribution in CoNiCrFeMn HEA after 50, 100, 150, 200, 250, 300 cascade collisions, respectively. The colors of lines or meshes indicated the same with Figure 2-9.

collisions, and the total and average dislocation length remain at a very low level. This phenomenon is similar as other experimental and simulation works, the lattice distortion in HEA will lead to high recombination of defects and the dislocation loop is significantly small [**16, 40**].

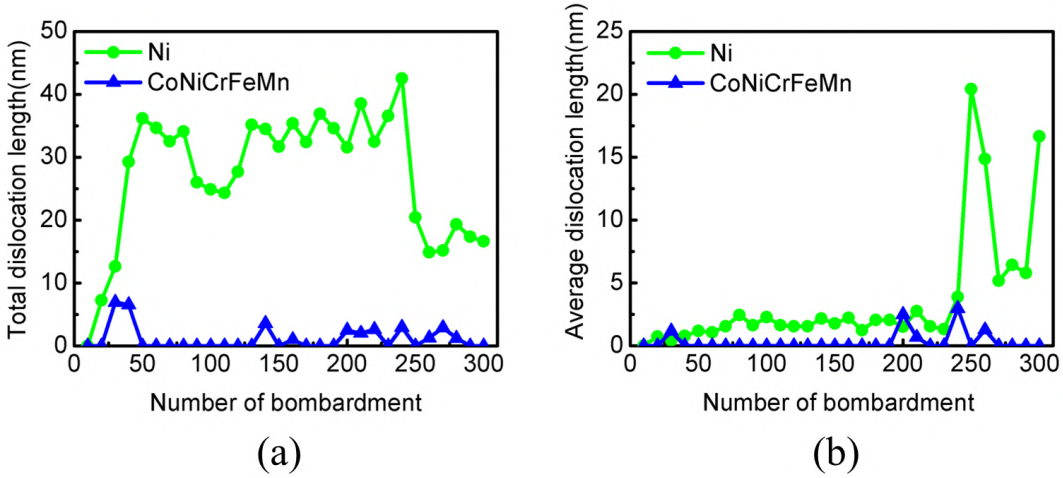

Figure 2.11: (a) Total length of dislocation loops, and (b) average length of dislocation loops in Ni and CoNiCrFeMn HEA after 300 cascade collisions.

2.3.4 Mean free path and migration barrier

The difference in defect and dislocation in Ni and CoNiCrFeMn HEA after irradiation may be related to cluster migration. It has been shown that small defect clusters in metallic can migrate along close-packed row of atoms [**72, 73**]. For simple metals, small interstitial clusters can migrate rapidly through 1-D motion [**74, 75**]. As the compositional complexity of the materials increases, the migration method of cluster is affected and a shift from 1-D to 3-D motion occurs. Mean free path (MFP) has been applied to asses the migration behavior of cluster in Ni and CoNiCrFeMn MEA before. The MFP is determined by calculating the average migration distance of small defect clusters before they change their migration direction. To investigate the migration behavior of interstitial cluster in Ni and CoNiCrFeMn HEA, a small interstitial cluster was created by inserting atoms inside the models. Considering that our results show

that that most clusters contain less than 10 atoms during irradiation, and in order to ensure that each element in the HEA is included, a cluster containing 10 atoms were chosen.

As the internal temperature of the substrate will reach a high temperature of approximately 1200 K during cascade collisions, interstitial cluster diffusion were performed at a temperature of 1200 K. **Fig. 2.12** shows the migration trajectories of the interstitial cluster centers in the Ni and CoNiCrFeMn HEA, respectively. The results show that the interstitial clusters in the Ni migrate a long distance with a relatively large MFP of 1-D motion before changing the direction of motion. However, for the interstitial cluster in CoNiCrFeMn HEA, only a small range of 3-D vibrations with much smaller MFP is observed, which is consistent with previous experimental work [**40**]. The MFPs of Ni and CoNiCrFeMn HEA exceed 40 nm and are less than 1 nm, respectively.The MFP of 10-atoms interstitial cluster in CoNiCrFeMn is reduced by more than 40 times compared to pure Ni, which may be a key mechanism for the high irradiation resistance of the CoNiCrFeMn HEA.

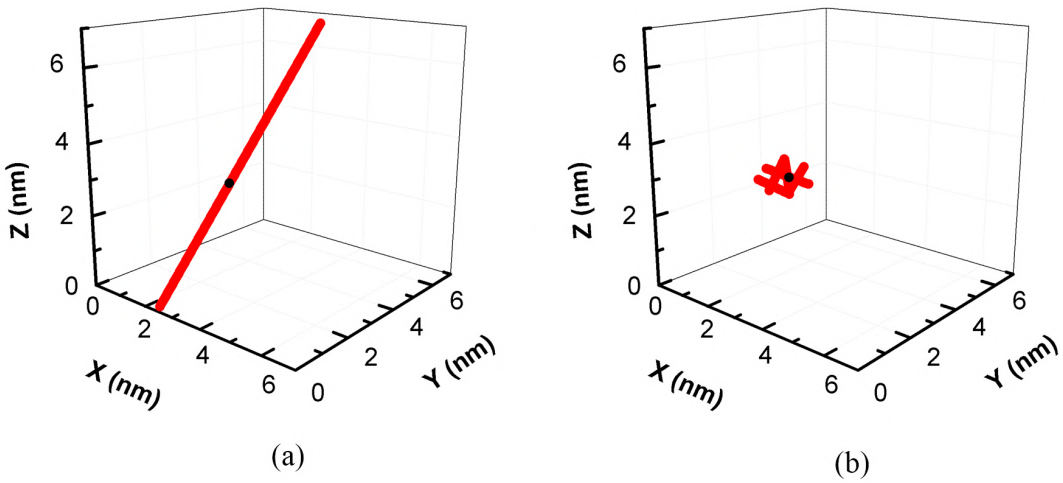

Figure 2.12: Trajectories of interstitial cluster diffusion in (a) Ni and (b) CoNiCrFeMn HEA.

The cage model can be used to explain the sluggish diffusion in CoNiCrFeMn HEA, which results in different migration behavior of defect cluster with Ni [**76**]. For the

traditional binary alloys, the minor elements are randomly distributed over the lattice sites. The percentage of minor elements is assumed to be c ($0 < c < 50\%$), These minor element atoms can be seen to form many cages and restrict the migration of defects in these cage regions. Interstitial clusters migrate through 1-D motion within a cage, however, the migration motion changes and gradually tends to 3-D motion at the surface or edges of the cage. The MFP λ in the cage model can be calculated as following equation:

$$\lambda = Ac^{-\frac{1}{3}} + B \tag{2.1}$$

where c is the percentage of the minor element, A and B are constants used to fit the equation. According to this equation, the MFP decreases with increasing percentage of minor element. For traditional binary alloys, c is less than 50%. However, for the CoNiCrFeMn HEA, which contains five principal elements in equal percentages and maintain an perfect atomic lattice structure, the corresponding percentage of minor elements c extends to 80% of each element, which more significantly suppresses the migration of interstitial clusters and dislocation. Therefore, the MFP of CoNiCrFeMn HEA is significantly reduced.

The migration behavior of interstitial clusters between Ni and CoNiCrFeMn HEA cause difference in the number of defects and dislocation loops. When interstitial clusters migrate long distances through 1-D motion in Ni, they will be detached from the cascade collision regions and therefore the probability of the interstitial cluster recombining with vacancies will be much lower, leaving more defects. Furthermore, when interstitial clusters migrate rapidly from the cascade collision regions to the surface or internal of Ni, the local supersaturation of the material will increase, which will lead to severe swelling and dislocation loops formation, as reported in previous experimental works [**77, 78**]. However, in the CoNiCrFeMn HEA, the severe lattice distortion not only inhibits the migration of interstitial clusters, but also increases the probability of interstitial and vacancy recombination through local vibrations. Thus, the composi-

tional complexity of CoNiCrFeMn HEA enhances the irradiation resistance.

As the migration behavior of defects has an important effect on the irradiation resistance properties of materials, we next calculated the single interstitial and vacancy migration barriers for Ni and CoNiCrFeMn HEA. The migration barriers are calculated using the NEB method, which determines the potential barriers to the reaction by searching the saddle points of the transition state [**79,80**]. Specifically, after defining the initial and final states with interstitial and vacancy, the variation of the total energy in the migration path is calculated and then the migration barriers are determined by calculation the climbing barriers of the model. The average interstitial migration barriers for Ni and CoNiCrFeMn HEA are calculated as 0.28 eV and 0.71 eV, respectively. While the average vacancy migration barriers for Ni and CoNiCrFeMn HEA are 1.48 eV and 0.97 eV, respectively. **Fig. 2.13 (a), (b)** shows one sample of the calculation results. It could be found that the difference between interstitial and vacancy migration barrier for Ni and CoNiCrFeMn HEA is quite large. **Fig. 2.13 (c)** shows the difference in migration barrier between interstitial and vacancy. For CoNiCrFeMn HEA, it has similar migration barrier with an average difference within 0.26 eV, whereas for Ni the difference much larger with a difference of more than 1.2 eV. It should be noted that the migration barrier can be uniquely defined in Ni, but not in CoNiCrFeMn HEA due to the complexity of the composition. Therefore, it is necessary to perform enough simulations to obtain an average value for CoNiCrFeMn HEA. The calculation results show that vacancy and interstitial in CoNiCrFeMn HEA have similar migration barriers, implying the high probability of recombination between interstitial and vacancy. For Ni, the migration barrier of vacancy is significantly larger than that of interstitial. Interstitial can rapidly escape the cascade collision regions, resulting in a large number of vacancies remaining in Ni, and the aggregation and collapse of vacancies can lead to the formation of dislocation loops and voids. Therefore, the difference in interstitial and vacancy migration barrier between Ni and CoNiCrFeMn may be the key factor in

radiation resistance.

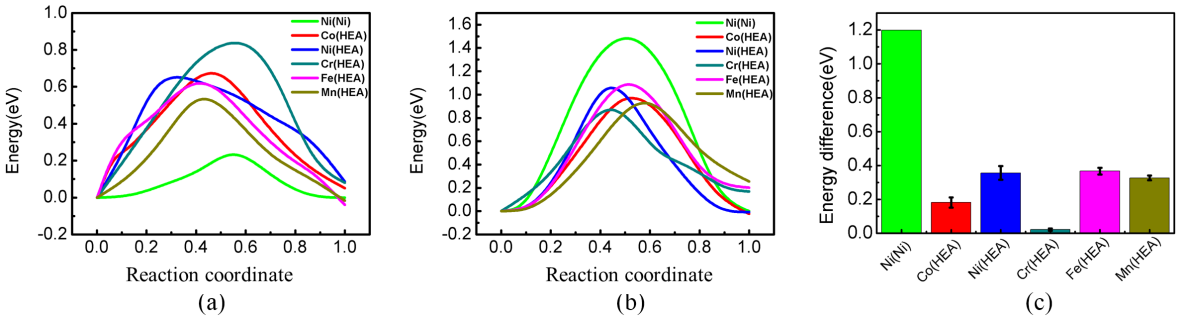

Figure 2.13: (a) Interstitial and (b) vacancy migration barrier, and (c) the difference in migration barrier between interstitial and vacancy migration barriers in Ni and CoNiCrFeMn HEA.

2.4 Conclusion

The extreme flux surface bombardments and internal consecutive bombardments were performed by MD simulations to study the surface radiation resistance and internal defects evolution in CoNiCrFeMn HEA, respectively. The number of defects, dislocation loops formation, and migration of interstitial and vacancy were discussed. All the simulation results are compared with pure Ni, and found that CoNiCrFeMn HEA has better radiation resistance. The cage model was used to explain the different behavior of defect between Ni and CoNiCrFeMn HEA, which may be the main reason for the better radiation resistance in CoNiCrFeMn HEA. The important results in this chapter can be concluded as following:

- During a single PKA process, the average depth of defects was shallower in CoNiCrFeMn HEA. During the consecutive bombardments, the number of defects in CoNiCrFeMn HEA was much less and stable, appearing to be insensitive to the number of bombardments. However, a boost of defects occurred due to the formation and slipping of dislocation loops in Ni. Therefore, CoNiCrFeMn HEA had much better surface radiation resistance.

- The internal defects evolution simulations show that more defects occurred in Ni and tended to form large size dislocation loops. However, defects in CoNiCrFeMn HEA was less and occurred in the form of small clusters, and the formation of dislocation loops was also effectively suppressed. The differences between Ni and CoNiCrFeMn HEA are due to the defect migration behavior. The MFP of interstitial cluster is smaller and interstitial cluster showed a small range 3-D vibrations in CoNiCrFeMn HEA. The cage model was used to explain the small MFP of interstitial cluster in CoNiCrFeMn HEA. In addition, interstitial and vacancy had similar mobility in CoNiCrFeMn HEA, which increased the probability of recombination of defects, resulting in less defects and dislocation loops.

- These results provided insights of the mechanism of radiation resistance in the CoNiCrFeMn HEA and could be useful in the design of radiation tolerance materials. It is also expected that the excellent radiation resistance of CoNiCrFeMn HEA could will enable its application in the nuclear structure materials.

Chapter 3

Chemical ordering effect on the radiation resistance of CoNiCrFeMn high entropy alloy

3.1 Introduction

Owing to its excellent radiation resistance, CoNiCrFeMn HEA shows potential for application in a new generation of nuclear structure material, which is driving much of research focused on HEAs [**16, 81**]. In the previous chapter, we focused on the surface radiation resistance and studied the evolution of internal defects in the random CoNiCrFeMn HEA. However, the high-temperature working conditions above 700 K will bring another challenge for the CoNiCrFeMn HEA as a material to be used in nuclear facilities [**10, 47, 82**]. Recently, several studies have pointed out that the chemical structure of CoNiCrFeMn HEA, previously considered to be a thermally stable single-phase, appears to be chemically ordered after prolonged annealing below a certain temperature [**83**–**85**]. Although the single-phase solid solution state is maintained even after annealing at 1100 K or above, a Cr-rich secondary phase may form after prolonged annealing at 900 K or below [**83**]. Therefore, additional attention should be paid to the chemical ordering of CoNiCrFeMn HEA, particularly with respect to the potential for phase decomposition due to the high-temperature working condition experienced by the materials used in nuclear facilities.

In addition, H/MEAs are generally considered to occupy a random solid solution state, but the degree of randomness of the atomic distribution in H/MEAs remains to be further determined. Several studies have reported that chemical short-range order (CSRO) structures are expected to develop in H/MEAs after annealing at specific temperature, which may have a significant impact on the structural stability and mechanical properties of H/MEAs [**46,86**–**90**]. On the one hand, first-principles density functional theory calculations and experimental TEM observations have shown that CSRO in CrCoNi is significantly related to the stacking fault energy and therefore the mechanical properties of the material can be improved by adjusting the degree of CSRO [**91, 92**]. Zhao et al. also reported that defect evolution in Ni–Fe alloys may be delayed due to the present of CSRO. In their framework, ordered structures can influence defect migra-

tion by changing the local atomic environment, so the radiation resistance of materials could be improved by the forming of the CSRO structures [**93**]. On the other hand, irradiation simulations of Fe-Cr and CuNiCoFe alloys have also shown that CSRO has little effect on the radiation resistance of H/MEAs containing these elements [**94, 95**]. Therefore, further studies are still needed regarding the formation of CSRO structures in H/MEAs and the influence of CSRO on mechanical properties, especially radiation resistance.

In order to systematically investigate the chemical ordering effect on the radiation resistance of CoNiCrFeMn HEA at high working temperatures, in this chapter, hybrid Molecular Dynamics (MD) – Monte Carlo (MC) annealing simulations at various temperatures are performed on the samples, followed by MD irradiation simulations on the annealed samples. MD simulation is a well-established approach for investigating irradiation, such as radiation damage and cascades phenomena, as we have described in the previous chapter. As an efficient and reliable approach, materials simulation plays an important role in the exploration of material properties [**57, 96**]. Here, we confirmed that the formation of Cr-rich regions in the initial stage after annealing at 600 K reduced the radiation resistance of CoNiCrFeMn HEA. The CSRO structure after annealing at 1100 K enhanced the radiation resistance, but the enhancement did not last long as the CSRO structures were destroyed under irradiation. Our investigations suggest that the chemical structures of H/MEAs including CSRO and its formation temperature should be carefully evaluated, especially when it is used as a radiation resistance material at various working temperatures, because if the formation temperature of CSRO can be adjusted to the working temperature, the radiation damage rate can be set to a moderate value, and the formation rate of CSRO can be accelerated by controlling, for example, the chemical compositions of H/MEAs, then further radiation resistance may be achieved. Finally, we discussed the condition of the CSRO preservation by proposing a CSRO radiation damage – diffusion healing competition model [**97**].

3.2 Simulation method and model details

3.2.1 Hybrid Molecular dynamics – Monte Carlo simulation

The same 2NN MEAM potential as in the previous chapter was chosen to describe the interatomic interactions of all atoms in CoNiCrFeMn HEA. This potential has been successfully applied to the irradiation simulations. In order to verify the quality of this potential in studying chemical ordering, we also tested the formation of other intermetallic phases by using this potential. Details can be found in the **Appendix A**. The hybrid MD – MC annealing simulations were performed to obtain models with different initial CSRO states after annealing at different temperatures. There are 10 MC steps for each MD step and a total of 5 million MC steps with an average of 20 swaps per atom. The Warren-Cowley parameter α_n^{ij} are used to evaluate the degree of CSRO for all element pairs after annealing at different temperatures [**98**]:

$$\alpha_n^{ij} = 1 - \frac{p_n^{ij}}{c_j} \tag{3.1}$$

where i and j refer to the element types, and n refers to the nth nearest neighbor. P describe the probability of occurrence of each element as a surrounding atom, and C is the system-wide average concentration of the corresponding element. When all atoms are completely randomly distributed, the expected CSRO parameter value is 0. The positive CSRO parameter value represents the segregation of elements i and j, and vice verse. In this study, temperature of 600 K and 1100 K were chosen and annealing simulations were carried out.

3.2.2 Chemical short-range order structures and parameters

Fig. 3.1 (a) - (c) show the local structural features of CoNiCrFeMn HEA after annealing at different temperatures and comparing them with the randomly distributed

state of atoms. The total number of atoms in the models is 256,000 and the length of each side is 14.28 nm. The CSRO parameters for each element pair in the model were determined at three different initial CSRO states as shown in **Fig. 3.1 (d)**. The CSRO parameters for CoNiCrFeMn HEA vary with annealing temperatures. After annealing at 600 K, the Co-Cr and Cr-Fe atom pairs strongly repel each other and show segregation. In contrast, the Co-Fe, Ni-Mn atom pairs exhibit mutual attraction and show a tendency to aggregate. The chemical ordering tendency of the different element pairs in CoNiCrFeMn HEA is in agreement with previous simulations by Guo et al. [**99**]. There is no crystal structure phase transition occurred during the annealing process.

We also found that Cr-rich regions were formed in CoNiCrFeMn HEA, which is consistent with previous experimental works by Otto et al., [**83**]. When CoNiCrFeMn HEA was annealed at 600 K, Cr-rich regions were formed due to the phase decomposition. It is important to note that in the experimental works of Otto et al. Cr tended to form bcc phases at grain boundaries or intracrystalline inclusions because of prolonged annealing. However, due to the limitations of the simulations, we only considered short annealing time in a perfect matrix structure and this Cr-rich region remained in the initial stage without phase transformation. The effect of this initial stage Cr-rich region on the properties of CoNiCrFeMn HEA has also attracted the interest of others [**58**]. The high annealing temperature of 1100 K weakens the segregation tendency of Co-Cr and Cr-Fe pairs, and the aggregation tendency of Co-Fe, Ni-Mn pairs. At higher temperature, the Cr-Cr parameter values decreased and the Cr-rich region also disappeared. After annealing at 1100 K, all the CSRO parameter values are much lower than after annealing at 600 K, and there are evident CSRO structures rather than phase decomposition. The CSRO parameter values for the models with random CSRO states were all found to be close to 0, indication that all elements are randomly distributed.

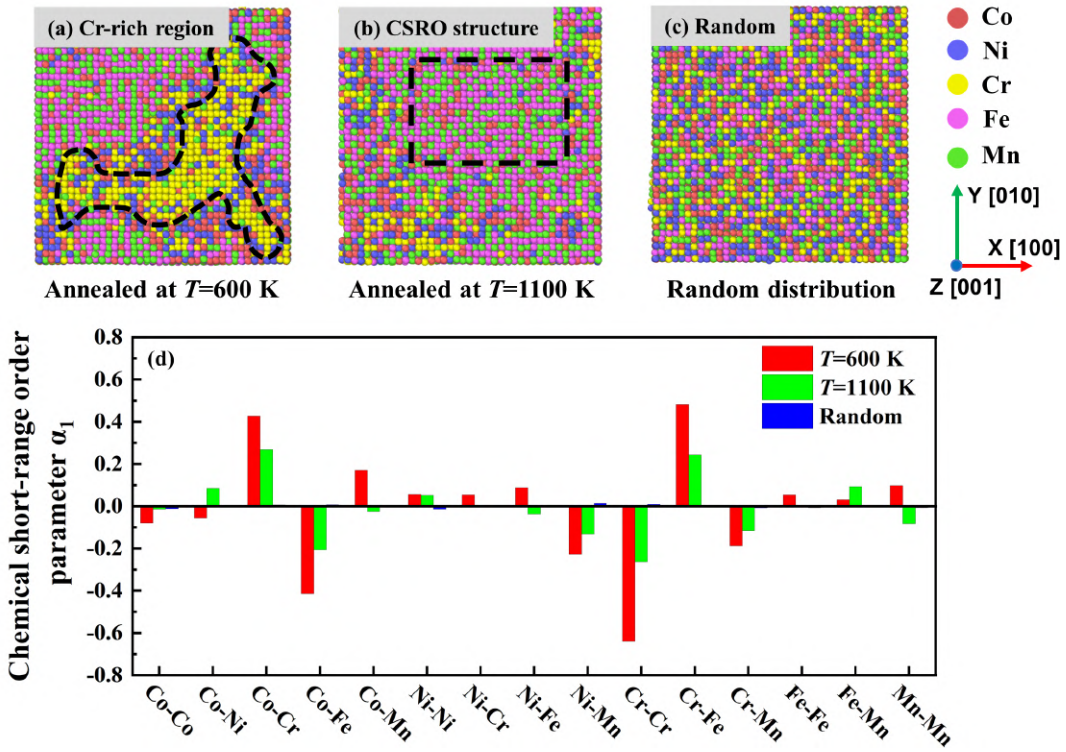

Figure 3.1: (a) - (c) Local structural features of CoNiCrFeMn HEA after annealing at a temperature of 600 K, 1100 K and in the random states, respectively. (d) Chemical short-range order parameter values of various element pairs.

3.2.3 Radiation damage simulation

The atomic structures of all the models were relaxed for 100 ps at 700 K using NVT ensemble MD simulations before stating the irradiation simulations. All atomic simulations in this study were performed by using the LAMMPS code. The PKA with an energy of 5000 eV was randomly selected in the model and the random direction of motions of all PKA was implemented to achieve a homogeneous irradiation effect. The irradiation process is carried out by imbuing each PKA with a random directional velocity corresponding to this energy. An adaptive step was used to ensure that no atom moved more than 0.002 nm during each simulation step. Three runs with different random seeds were performed for each condition and averaged. A Micro-canonical ensemble was applied during the irradiation simulation, and Berendsen thermostat with 700 K was applied only with 1 nm thick layer regions on all sides to simulate severe

high temperature working conditions. OVITO was used to analyze and visualize the simulation results. The WS method was used to count the number of defect atoms, and the DXA method was used to identify the dislocation loops. It is worth noting that many irradiation experiments and simulations were also carried out at around 700 K [**16,40**]. Each irradiation bombardment lasted 50 ps to ensure that the model could cool down to ambient temperature.The irradiation process consisted of 500 bombardments, taking into account the available computational resources and time. Based on the NRT-dpa (Norgett-Robinson-Torrens displacements per atom) model [**100**], a threshold displacement energy of 40 eV was used here, which is consistent with previous similar simulation and experimental works, and the final damage level could be achieved at a dose of 0.1 dpa [**41, 50**].

3.3 Results and discussion

3.3.1 Radiation damage results

Three models with different initial CSRO states were subjected to 500 consecutive irradiation bombardments. **Fig. 3.2** shows the structural damage and dislocation loops formation after 100, 300 and 500 irradiation bombardments with corresponding damage levels of 0.02, 0.06 and 0.1 dpa. There are no phase transition occurred during irradiation and several defects clustered together. Dislocation were found in models with different initial CSRO states due to irradiation bombardment and the evolution of defect clusters. Most of the dislocations appears in the form of complex dislocation loops, mainly represented by interstitial-type dislocation segments with the Burgers vectors of $b = 1/6<112>$. We have found only a few vacancy-type dislocation loops with a Burgers vector of $b = 1/6<110>$, some of which transform into stacking fault tetrahedral dislocations or voids during irradiation simulations. Therefore, CoNiCrFeMn HEA is able to suppress the formation of voids and shows enhanced radiation resistance.

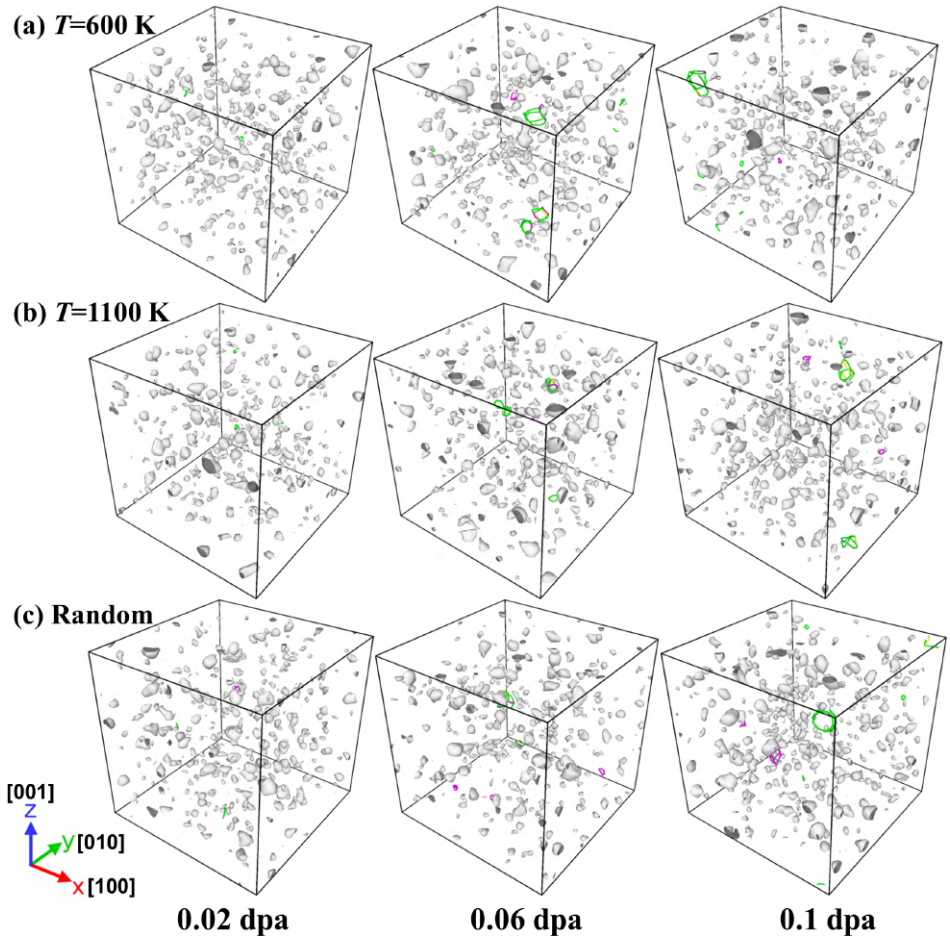

Figure 3.2: (a) - (c) Structural damage and dislocation loops in CoNiCrFeMn HEA annealed at 600 K, 1100 K and in the random states, respectively. Green, pink, and yellow lines denote Shockley 1/6<112>, Stair-rod 1/6<110>, and Hirth 1/3<100> dislocation loop segments, respectively.

In order to further evaluate the performance of HEA for different initial CSRO states during irradiation bombardments, we statistically analyzed the defect concentration, interstitial cluster size distribution, dislocation density, and average dislocation loops length. The results for different initial CSRO states were obtained by averaging three runs with different random seeds. **Fig. 3.3 (a)** shows the defect concentration as a function of the number of the number of bombardments calculated using WS method. Model with different initial CSRO states show a similar initial trend of rapidly increasing defect concentration. Due to the dynamic balance between the generation of new defects and the annihilation of interstitial and vacancy, the defect concentration then saturates

and fluctuates around a stable value, a trend that can also be found in other H/MEAs irradiation bombardments results [**50,101**]. Compared to the other initial CSRO states, the model annealed at 1100 K shows a relatively low defect concentration and the defect concentration remains slowly increasing during the simulation. Only after about 400 irradiation bombardments does the defect concentration gradually reach levels similar to those of the models for the other initial CSRO states. **Fig. 3.3 (b)** shows the interstitial cluster size distribution after 500 irradiation bombardments. The first nearest neighbor distance (2.5 Å) is used as a cluster identification criterion, and all interstitial atoms within this distance are considered to belong to the same defect cluster. The error bars represent the upper and lower deviations from the results of the three runs. In the model for each initial CSRO state, most of the interstitial defects (40% or more) are present in the form of medium-size clusters (11 to 30 defects per cluster). It is worth noting that super-large-size clusters ($>$ 100 defects per cluster) appear more frequently in the model annealed at 600 K than in the others models (approximately 15% of all defects); this finding suggests a more rapid evolution of defect clusters in this initial CSRO state model.

Fig. 3.3 (c) shows the dislocation density for each of the different initial CSRO state models, the fluctuating growth is maintained in all irradiation bombardments. However, the higher dislocation density occurs mainly in the model annealed at 600 K, as more interstitial defects are clustered in the super-large-size clusters. The model annealed at 1100 K shows a much delayed increase in dislocation density compared to the other models. **Fig. 3.3 (d)** shows the average dislocation loops length during irradiation bombardments. The average dislocation loop lengths for the models of the three initial CSRO states range from 10 Å to 17 Å. Although dislocation evolution sometimes increases the average dislocation loops over time, the average dislocation loops length decreases rapidly with dislocation decomposition due to the instability of large-size dislocation loops in CoNiCrFeMn HEA, such feature of HEAs are distinctly

different from those of traditional metals. As we have found in previous chapter, in pure Ni, large size dislocation loops are produced and stabilised as Frank 1/3 <111> dislocation loops.

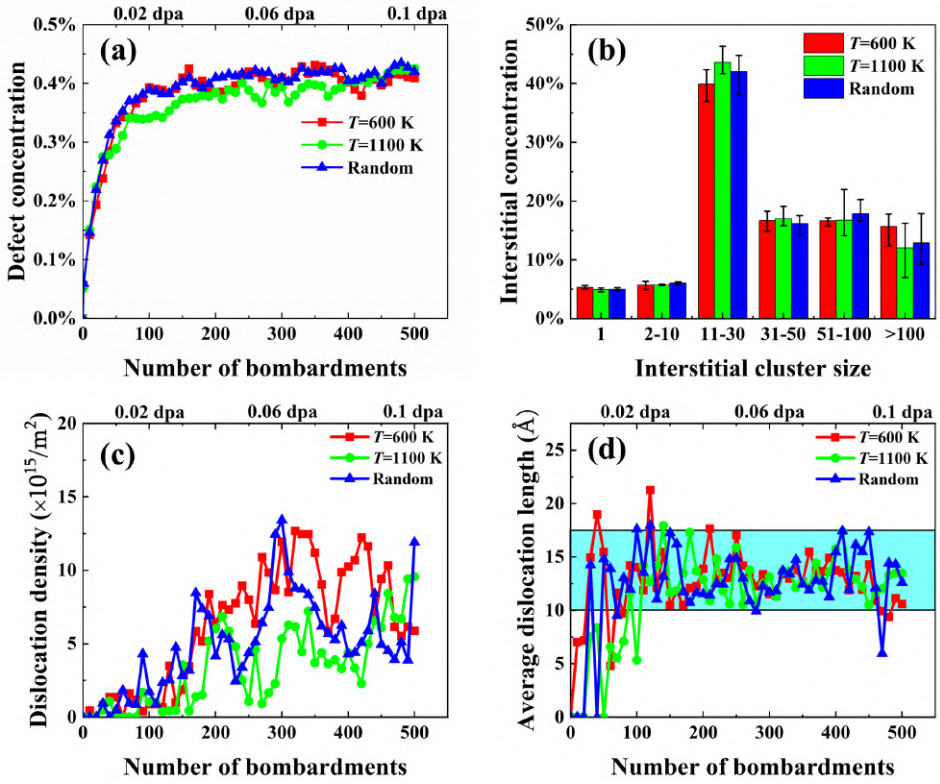

Figure 3.3: (a) Defect concentration during irradiation bombardment; (b) interstitial cluster size distribution; (c) dislocation density; (d) average dislocation loops length.

The above findings suggest that the annealing temperature of CoNiCrFeMn HEA acts through the CSRO level and influences the defect and dislocation loops performance during irradiation. The model annealed at 600 K shows a faster evolution of defect clusters leading to a higher dislocation density. The model annealed at 1100 K shows delayed defect growth and dislocation formation during irradiation bombardments, which corresponds to improved radiation resistance. The effect of annealing temperature on the properties of CoNiCrFeMn HEA deserves further attention.

3.3.2 Defects evolution and thermodynamics behavior after irradiation

Defects evolution simulations were carried out to determine the cause of the increase of dislocation density in the CoNiCrFeMn HEA annealed at 600 K. As shown in **Fig. 3.4**, Interstitial and vacancies (1% Frenkel pairs) were randomly added to a small size model of 32,000 atoms.The total simulation time was 10 ns, and the same simulations were done in the model with random CSRO status for comparison. Initially, all defects were randomly distributed as small-size clusters. During the defect evolution simulation, some interstitial aggregated into larger clusters, while some disappears by binding to vacancies. The results after 5 ns of evolution show that complex dislocation loops formed rapidly in the CoNiCrFeMn HEA annealed at 600 K. However, in the model with random CSRO status, all defects remain in small-size clusters and no dislocation loops are found. Finally, the dislocation loops in the model annealed at 600 K are stable, while the defects in the model with random CSRO state appear as large-size clusters.

We also note that the region of dislocation loops formation is in the Cr-rich region, a finding that implies that dislocations are more likely to form in the Cr-rich region. To confirm this, we compare the energy of prismatic dislocation loops in the Cr-rich and Cr-less regions. As shown in **Fig. 3.5**. Three CoNiCrFeMn models with different Cr concentrations were chosen ($Co_{22.5}Ni_{22.5}Cr_{10}Fe_{22.5}Mn_{22.5}$, $Co_{20}Ni_{20}Cr_{20}Fe_{20}Mn_{20}$, $Co_{15}Ni_{15}Cr_{40}Fe_{15}Mn_{15}$), all the atoms were randomly arranged with maintaining the given chemical composition. The model dimension in x, y and z directions were set to 63.99 Å, 66.50 Å, and 62.70 Å, respectively. Periodic boundary condition was applied in x, y, and z directions. The atomic structure of models were relaxed using conjugate gradient method. By using the loop radius of 15 Å, the energy of the dislocation per unit length were calculated as 5.01 eV/Å, 4.49 eV/Å, and 4.23 eV/Å, respectively. The dislocation in the Cr-rich model has significantly lower energy than in the Cr-less model.

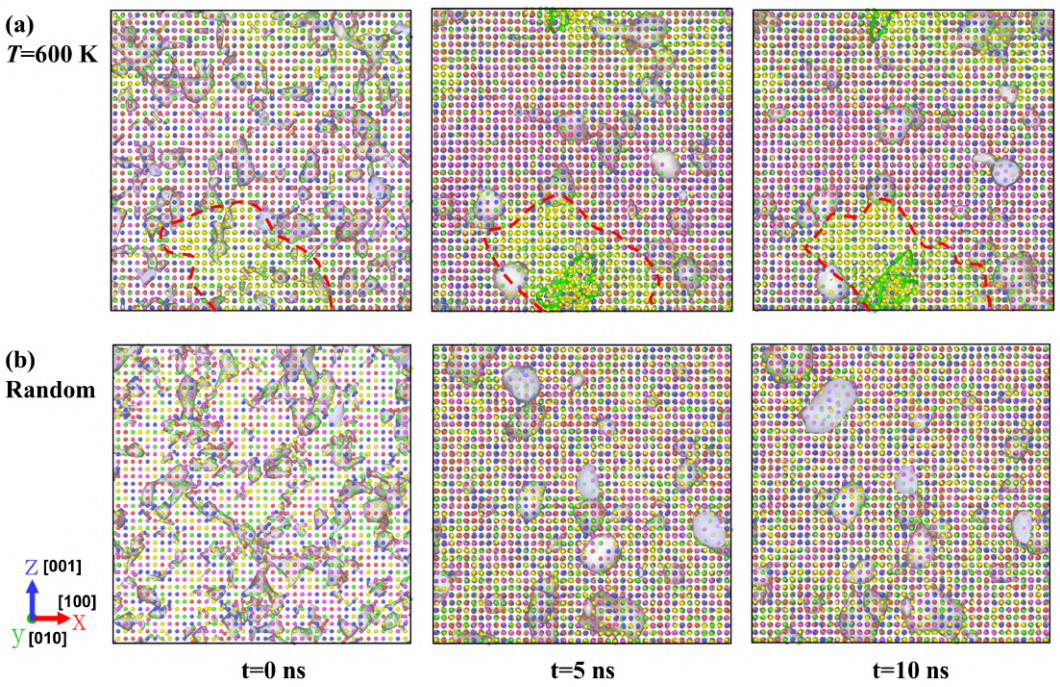

Figure 3.4: Evolution of 1% Frenkel pairs in CoNiCrFeMn HEA throughout 10 ns. (a) In the model annealed at 600 K and (b) random CSRO states. The colors of lines segments denote different types of dislocation loops as described earlier. The red dashed lines added as a guide for the eye and marked the Cr-region.

Therefore, the evolution of the aggregation of interstitial and defect clusters makes it easier for dislocation loops to form here. The Cr-rich region formed by annealing at 600 K seems to accelerate the growth of dislocation loops and reduce the radiation resistance of CoNiCrFeMn HEA.

The thermodynamics behavior of these defect structures after irradiation bombardments is also interesting. Therefore, the hybrid MD – MC annealing simulations were repeated on the non-equilibrium system to investigate the further evolution of defects. The change in potential energy during the annealing simulations is depicted in **Fig. 3.6 (a)**. This potential energy gradually decreases, eventually reaching equilibrium in the Cr-rich (annealed at 600 K) and CSRO (annealed at 1100 K) models. The potential energy energy per atom in the Cr-rich model is -3.962 (-3.959) eV/atom and -3.973 (-3.972) eV/atom before and after the annealing simulation, respectively. **Fig. 3.6 (b) - (e)** show the defect distribution before (non-equilibrium stage) and after annealing

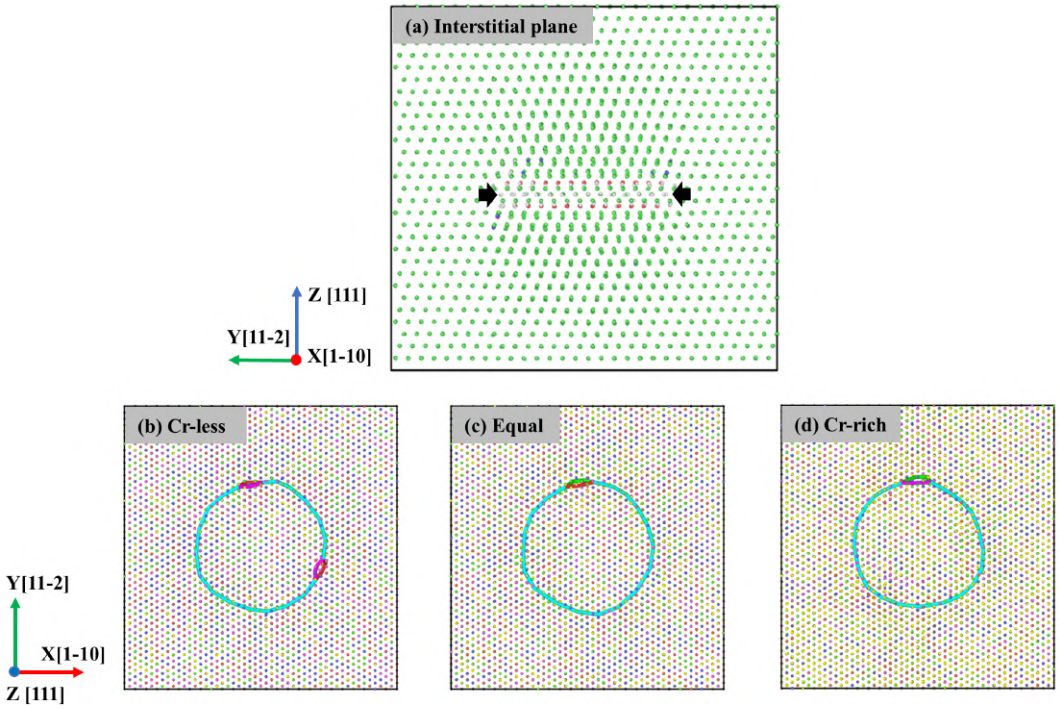

Figure 3.5: (a) Side-view of a prismatic dislocation loop constructed with inserting an extra (111) atom plane inside of the loop. (b)-(d) The prismatic dislocation loops in Cr-less, Cr-equal, and Cr-rich models, respectively.

(equilibrium stage). **Fig. 3.6 (f)** depicts the variation in the defect composition of the elements. The Cr and Mn atoms of the defects in the equilibrium stage structure increase after annealing. In particular, we investigated the composition of the largest-size defect cluster in the Cr-rich and CSRO models. As shown in **Fig. 3.6 (g) - (h)**, the total proportion of Cr and Mn atoms in the largest-size defect cluster reaches approximately 50% and 60% in the Cr-rich and CSRO models, respectively. It was found that Cr and Mn atoms are the fastest diffusion atoms in CoNiCrFeMn HEA, preferring to cluster at defect locations [**26**]. This is because Cr and Mn atoms nucleate and form new phases at grain boundary and defects more rapidly [**83**].

3.3.3 Interstitial diffusion behaviors

The formation of dislocation loops during irradiation simulations is mainly related to the aggregation of interstitial and the evolution of clusters. In order to investigate the

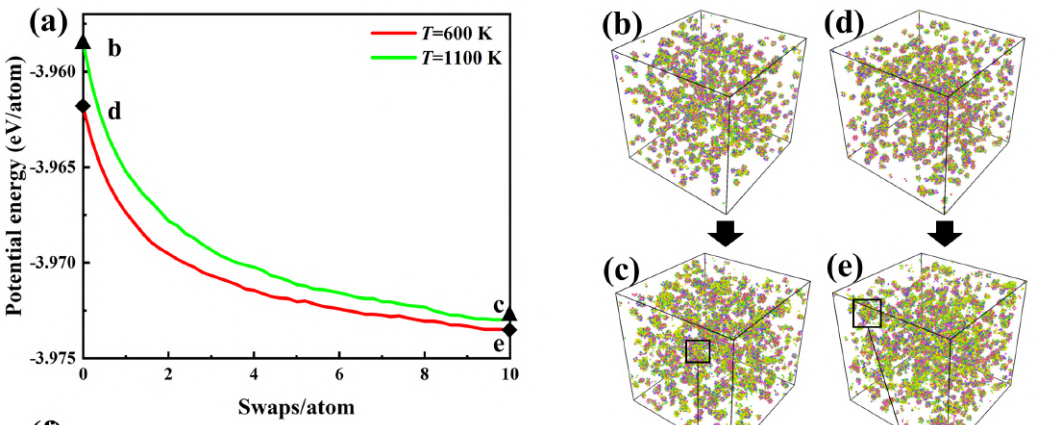

(f)

Defects composition (%)	Unannealed b (d)	Annealed c (e)
Co	20.3% (21.3%)	18.6% (18.8%)
Ni	14.3% (13.7%)	12.6% (11.9%)
Cr	22.3% (21.5%)	27.8% (27.7%)
Fe	17.0% (17.9%)	14.6% (14.7%)
Mn	26.1% (25.6%)	26.4% (26.9%)

Figure 3.6: (a) Potential energy change during MD – MC annealing simulation. (b) - (e) Defects distribution in the model before and after annealing. (f) Defect composition of elements before and after annealing. (g) - (h) Largest-size cluster in the model after annealing

effect of annealing temperature on the radiation resistance in CoNiCrFeMn HEA, the diffusivity of interstitial defects has to be calculated. The mean squared displacement (MSD) of individual interstitial defects was calculated, and the diffusivity of interstitial D can be estimated by:

$$D = \frac{\frac{1}{N}\sum_{i}^{N} |\boldsymbol{R}_i(t) - \boldsymbol{R}_i(0)|^2}{6t} \tag{3.2}$$

where N is the total number of atoms in the model, $\boldsymbol{R}_i(t)$ and $\boldsymbol{R}_i(0)$ are the position vectors of atom i at time t $= t$ and t $= 0$. **Fig. 3.7 (a)** shows the diffusivity of the interstitial defects of CoNiCrFeMn HEA annealed at 600 K and 1100 K varies significantly (from 2.74×10^{-3}Å^2/ns to 1.22×10^{-6}Å^2/ns and from 6.05×10^{-4}Å^2/ns to 2.83×10^{-7}Å^2/ns, respectively.) and strongly influenced by the local environment. However, the interstitial diffusivity in the model with a random state is relatively stable due to the more homogeneous atomic environment. Furthermore, we found higher

interstitial diffusivity in the model annealed at 600 K, but lower interstitial diffusivity in the model annealed at 1100 K. Due to the formation of Cr-rich region altering the interstitial diffusion pattern, as discussed below, where the CSRO structure delays the diffusion of defects, which is consistent with the relevant finding of Zhao et al. [**93**]: the preferential diffusion effect of the CSRO structure may effect the diffusion of interstitial, leading to a considerable delay in defect evolution. We also tracked the fraction of time spent in diffusion by different interstitial dumbbell pairs in CoNiCrFeMn HEA, as interstitial form different dumbbell pairs during diffusion. The WS method was used to determine the location of interstitial defects during diffusion, with perfectly structured lattice sites as reference configurations. When interstitial atoms and lattice atoms occupy the same lattice site, they are referred to as interstitial dumbbells and the statistics are shown in **Fig. 3.7 (b)**. It is worth noting that in the model with random states, the interstitial diffusion is mainly through the motion of Co-Cr, Co-Mn and Cr-Mn dumbbell pairs. However, in the CSRO model (annealed at 1100 K), the Co-Cr dumbbell pairs dominate the interstitial diffusion motion, while in the Cr-rich model (annealed at 600 K), the Cr-Mn dumbbell pairs dominate the interstitial diffusion motion. This suggests that interstitial diffusion is highly dependent on their local chemical environment and thus changes the time fraction of dumbbells.

We further investigated interstitial diffusion in the Cr-rich model. In some runs, the interstitial defects show rapid diffusion and high diffusion rates, but in other runs, the defects are almost stagnant. In fact, in the runs of model annealed at 600 K, three different cases of interstitial diffusion emerged. Firstly, when the interstitial is located near the boundary of the Cr-rich region, the interstitial is absorbed by the boundary and resists further movement. Secondly, when the interstitial was away from the boundary of Cr-rich region, the interstitial showed the similar diffusivity as the rest of the CoNiCrFeMn HEA. Finally, when the interstitial is in the Cr-rich region, more Cr-X interstitial dumbbell pairs are expected to form during diffusion. As shown

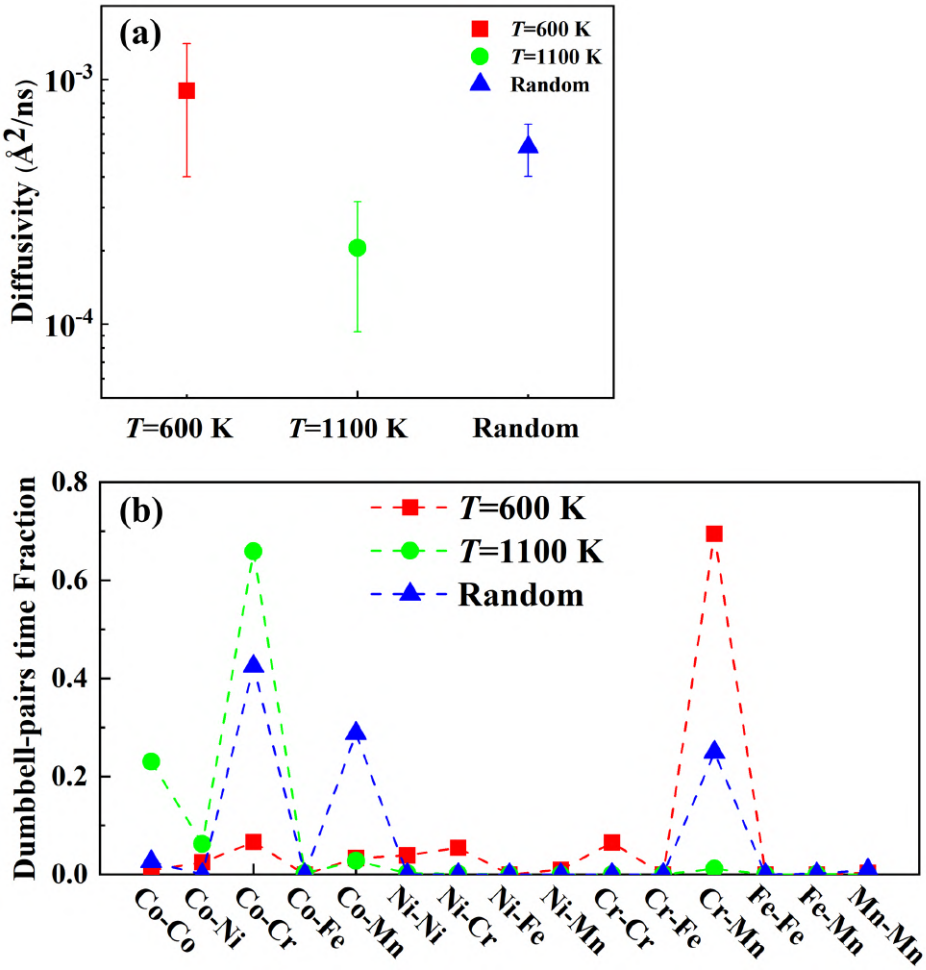

Figure 3.7: (a) Interstitial defect diffusivity. (b) Fraction of time spent by different interstitial dumbbell pairs during diffusion in the model with three different initial CSRO states.

in **Fig. 3.7 (b)**, it is clear that more Cr-Mn dumbbell pairs are formed in the Cr-rich model. This is due to the low energy of formation of [100] Cr-Mn dumbbells in CoNiCrFeMn HEA [**102**]. In addition, we calculated the migration potential barriers for Cr-Mn interstitial dumbbells for different Cr concentrations using the NEB method by DFT calculation, where higher Cr concentrations lead to lower migration barriers for interstitial dumbbells (Details of DFT calculation results can be found in the **Appendix A**). The same phenomenon was previously found in Ni-Fe alloys: Osetsky et al. found that the interstitial diffusivity gradually increased with increasing Fe concentration as the Ni-Ni interstitial pairs transformed into an Fe-Fe dumbbell [**103**]. Thus, the rapid

diffusion phenomenon of the interstitial in the Cr-rich model can be explained by the interstitial dumbbell transition. After annealing at 600 K, the formation of Cr-rich regions in CoNiCrFeMn HEA allows the local environment of the interstitial defects to have a considerable influence on diffusivity.

Overall, the Cr-rich region in CoNiCrFeMn HEA, the formation of which is caused by annealing at 600 K, leads to changes in the distribution of elements. These changes lead to the formation of Cr-X interstitial dumbbells in the Cr-rich region and result in rapid migration of interstitial defects, leading to less reliable radiation resistance performance. In addition, the CSRO structure formed by annealing at 1100 K appears to reduce the diffusivity of interstitial defects and delay defect evolution. This effect of CSRO on interstitial diffusion is expected to be reflected in the radiation resistance of CoNiCrFeMn HEA. For these reasons, strong attention should be paid to the effect of annealing temperature on elemental segregation of CoNiCrFeMn HEA, especially the effect of the Cr-rich region on the properties after annealing.

In addition, as previous mentioned, after annealing at 600 K, CoNiCrFeMn HEA shows worse radiation resistance because of the faster evolution of defect clusters in the Cr-rich region and consequently higher dislocation density. The mechanism of the effect of Cr-rich region on defect evolution thus needs to be further investigated. Diffusion simulations of two interstitial defects with different initial defect positions were carried out on a small size model of 4000 atoms to observe the influence of the Cr-rich region on defect evolution for 10 ns. As shown in **Fig. 3.8**, the various atoms are almost randomly distributed in the top part of the model, where the interstitial shows slow diffusivity and resisted long-distance migration. However, in the bottom part of the model, where the Cr-rich region is formed, interstitial exhibits rapid diffusion. After about 5.5 ns, the two interstitial defects meet at the phase boundary, where they merge and enter the Cr-rich region. The lattice constants for the top and bottom of the model have been calculated to be 3.60 Å and 3.65 Å, respectively. The lattice misfit degree

between the two parts is calculated as 1.38% according to:

$$\delta = \frac{2(a_2 - a_1)}{a_1 + a_2} \tag{3.3}$$

where a_1 and a_2 are the lattice constants of the two phases. This small lattice misfit suggests that the two phases can form a coherent interface that can exist stably. However, the large lattice constant in the Cr-rich region also affect the diffusion of defects, and the internal stress caused by the lattice misfit may provide part of the driving force for defect diffusion, promoting defect aggregation in the Cr-rich region. These results demonstrate the unique defect aggregation mechanism of CoNiCrFeMn HEA annealed at 600 K, whereby the appearance of Cr-rich regions and the ensuing lattice misfit provide part of the driving force for defect diffusion. The aggregated interstitial defects subsequently enter the Cr-rich region and merge with other defects. This unique interstitial aggregation mechanism suggests that the formation of Cr-rich regions accelerates the aggregation and growth of defects, leading to higher dislocation density during irradiation simulation.

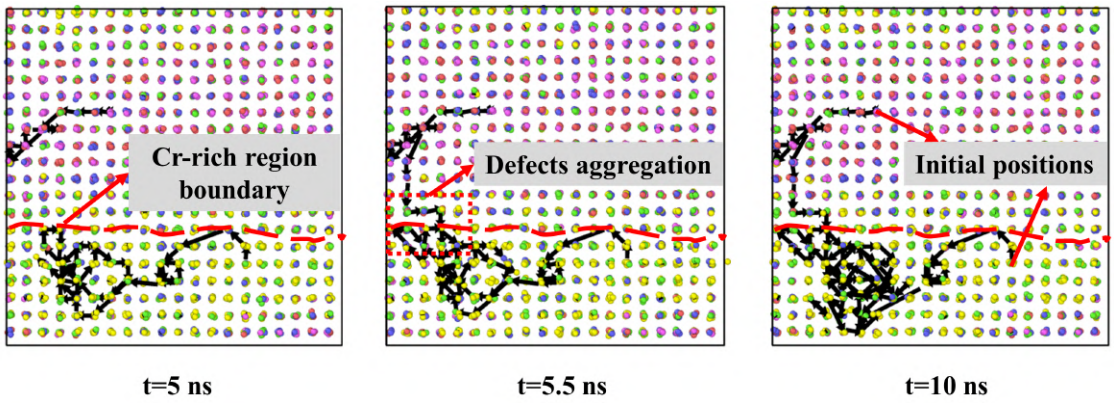

Figure 3.8: Diffusion simulation of two interstitial defects with distinct initial positions in CoNiCrFeMn after annealing at 600 K. Black lines denote the diffusion trajectories of interstitial defects; red dashed lines denote the Cr-rich region boundary.

Difference in local interstitial formation energies may also contribute to differences in interstitial aggregation mechanism. For the fcc lattice, interstitial remains in octa-

hedral vacancy site and then form an interstitial dumbbell with [100] oriented lattice atoms. **Fig. 3.9 (a)** shows such an interstitial dumbbell and the mechanism of interstitial migration. The interstitial migrates with the dumbbell in the [100] direction to a new octahedral vacancy site, and then another interstitial dumbbell is formed to complete the interstitial migration. Thus, the direction of migration of interstitial defect depends on the formation energy of interstitial dumbbell. As shown in **Fig. 3.9 (b)**, to determine the interstitial formation energy at different sites, the (100) plane was chosen to calculate the local interstitial formation energy. For each octahedral vacancy site, we insert an interstitial atom and then calculated the corresponding energy of the interstitial atom after it forms a dumbbell pair with the surrounding lattice atoms. Finally, we can obtain the interstitial formation energy in the (100) plane. The interstitial dumbbell formation energy was calculated according to:

$$E_{\mathrm{I}}^{\mathrm{f}} = E_{\mathrm{I}} - E_{\mathrm{perfect}} - \mu \tag{3.4}$$

where E_{I} is the total energy of the structure contain the interstitial, E_{perfect} is the energy of a perfect lattice, and μ is the chemical potential of the corresponding element in CoNiCrFeMn HEA. The details of interstitial dumbbell formation energy calculation can be found elsewhere [**102**].

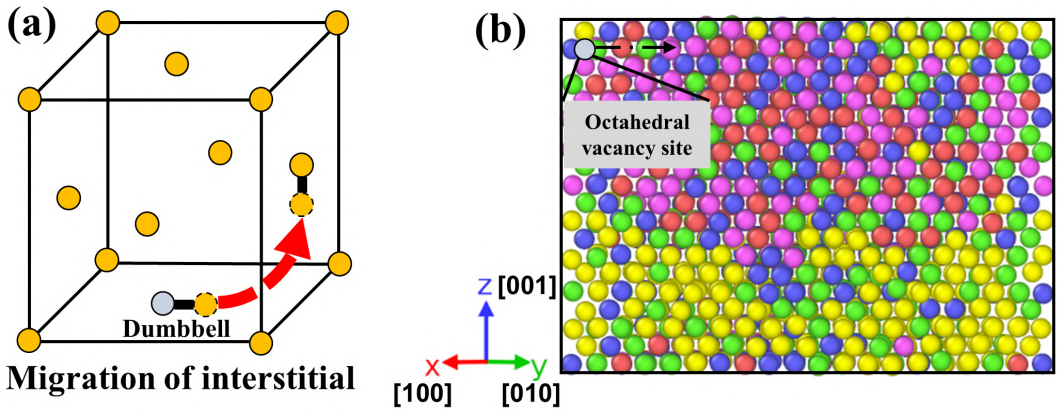

Figure 3.9: (a) Interstitial [100] dumbbell and migration mechanism in fcc lattice. (b) (110) CoNiCrFeMn HEA plane after annealing at 600 K.

To illustrate the differences in local interstitial dumbbell formation energies, contour maps of the interstitial formation energies for different octahedral vacancy sites in the (100) plane were plotted. **Fig. 3.10 (a) - (e)** show the results for the interstitial dumbbell formation energy for each element of CoNiCrFeMn HEA. In order to quantify the boundaries of Cr-rich regions, the Cr element chemical concentration in the region around each atom (within a sphere with a radius of 6 Å) was calculated. In this case, Cr element chemical concentration C_{Cr} greater than 0.3 were identified as Cr-rich regions and less than 0.2 were identified as atoms randomly distribution region, with the boundary lying between these two values. This approach has also been used in our previous work [**104**]. **Fig. 3.10 (f)** shows the average interstitial dumbbell formation energy in the [001] direction in the (100) plane; the Cr-rich region shows low dumbbell formation energies for all five elements of CoNiCrFeMn HEA. These results could also explain the greater tendency for dislocations to form in the Cr-rich region, as defects tend to cluster in this region.

3.3.4 Radiation damage – diffusion healing competition model

It has also been reported that CSRO structures confer good irradiation resistance by slowing down the diffusivity of defects, thereby retarding their evolution and inhibiting their growth [**88, 93**]. In this study, annealing at 1100 K produced CSRO structures where the aggregation of interstitial clusters was the main cause of dislocation formation during irradiation bombardment. Therefore, the defect clusters in CoNiCrFeMn HEA annealed at 1100 K are expected to be smaller than in other states and fewer dislocation loops are also expected. In our irradiation simulations, the model exhibiting CSRO does show a slower average interstitial diffusivity and lower defect concentration. The defect cluster size statistics also show that CSRO suppressed the total number of defects in the super-large-size clusters, thus allowing more defects exist in the medium-size clusters. However, in the model runs presenting the CSRO state, the lower defect

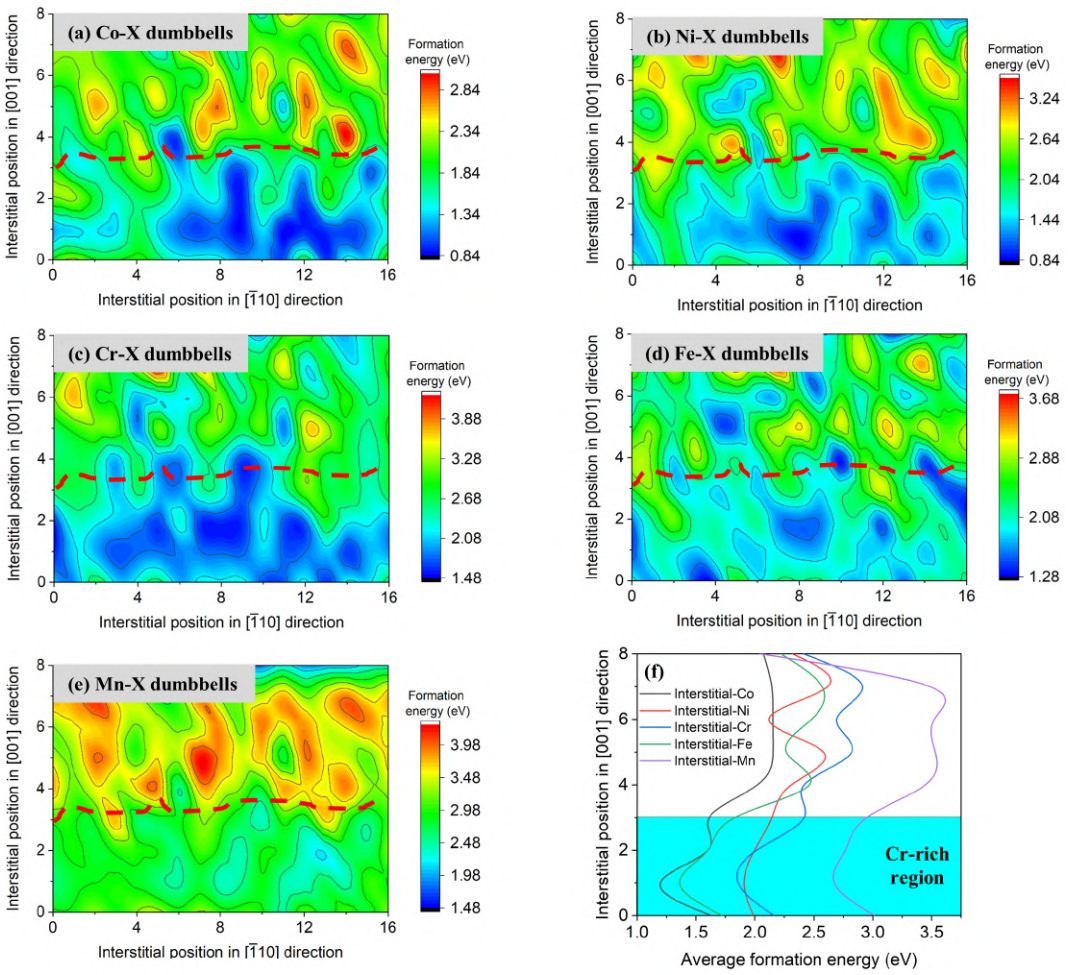

Figure 3.10: (a)–(e) Formation energy of interstitial dumbbell pairs of (a) Co–X, (b) Ni–X, (c) Cr–X, (d) Fe–X, and (e) Mn–X in the (110) plane; red dashed lines denote the region boundary. (f) Average formation energy change of interstitial in [001] direction of each element

defect concentration was only temporary; after about 300-400 bombardments, the defect concentration reached the same state as in the random model. This may be due to damage to the CSRO structure during radiation.

Fig. 3.11 (a) - (c) show the variation of CSRO parameters for key element pairs in the irradiation bombardment simulations with three different initial CSRO states. Here, it is worth noting that irradiation bombardment is a fast process. Immediately after each bombardment, all atoms in the radiation region melt and rearrange themselves within 10 ps. The thermal activation time of the CSRO is several orders of magnitude

longer than that destroyed by the radiation bombardments. Therefore, there is almost no nonlinear interaction between these phenomena, and we can assume that the changes of CSRO in **Fig. 3.11** are dominated by the bombardment during the irradiation simulation. It is interesting to find that the CSRO parameters for each element pair tended to be stable. For the initial random state model, the CSRO parameters show some variation, but their magnitude remains low compared to the corresponding parameters for the other model in the initial state. We predict that with more irradiation bombardment, the CSRO parameters for the three different initial states will eventually converge if there is no healing mechanism for the CSRO, as irradiation bombardment gradually destroys the CSRO structure. Hence, although the model runs exhibiting CSRO in the initial phase show low defect concentrations, irradiation bombardment will continue to destroy the CSRO structure. It is expected that the number of defects will continue to increase, eventually reaching the same density as the initial random state of the model. For this reason, the enhanced radiation resistance of CSRO will not last for long.

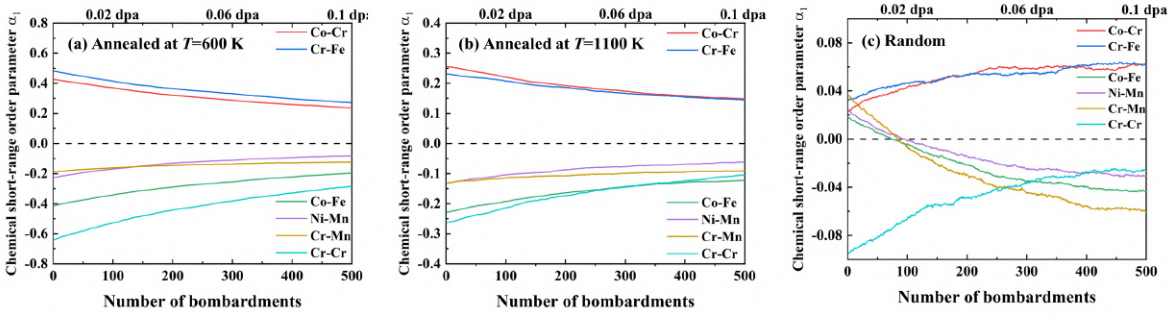

Figure 3.11: Changes in chemical short-range order parameters for CoNiCrFeMn HEA during irradiation bombardment for (a) annealed at 600K, (b) annealed at 1100 K, and (c) a random state.

However, if the working temperature is increased to 1100 K, we can obtain a healing mechanism for CSRO. The CSRO structure formed by annealing at 1100 K must be thermodynamically stable at 1100 K. Therefore, we still have the opportunity to preserve the radiation resistance advantage of CSRO in the long term by controlling

the working temperature and radiation bombardment. To show the possibility for CSRO preservation, the competition between radiation damage rate and CSRO healing (re-formation) rate at the working temperature should be discussed. Since the CSRO healing proceeds by thermally activated atomic diffusion through vacancy and interstitial jumps, the time scale of CSRO healing is provided by the frequency of the vacancy and interstitial jumps [**104**]. For simplicity, we only consider interstitial jumps as the healing mechanism of CSRO in the following discussion, since interstitial diffusion is much faster than vacancy diffusion. The CSRO parameter α_1 is used to describe a proxy for the CSRO state.

We propose a CSRO radiation damage – diffusion healing competition model as schematically shown in **Fig. 3.12 (a)**. The dash line of $\alpha_1^{\mathrm{E}}(T^{\mathrm{W}})$ and α_1^{D} shows the CSRO parameter α_1 at an equilibrium CSRO state after long-time annealing at a working temperature of T^{W} and fully damaged chemically disordered state after large radiation damage with high bombardment rate, respectively. The initial CSRO parameter is $\alpha_{1\mathrm{I}} = \alpha_1^{\mathrm{E}}(T^{\mathrm{W}})$, and then the bombardments start with an interval Δt. At each bombardment, the CSRO structure is destroyed and then the CSRO parameter decreases by a certain amount $\Delta\alpha_1^{\mathrm{B}}$. Here, we assume that $\Delta\alpha_1^{\mathrm{B}}$ is constant. The damage rate can be defined as $\dot{\alpha}_1^{\mathrm{D}} = \Delta\alpha_1^{\mathrm{B}}/\Delta t$. By ith bombardment, the CSRO parameter changes from $\alpha_{1\mathrm{I}}^i$ to $\alpha_{1\mathrm{E}}^i$ (the vertical red lines in **Fig. 3.12 (a)**), where $\alpha_{1\mathrm{E}}^i = \max\left\{\alpha_{1\mathrm{I}}^i - \Delta\alpha_1^{\mathrm{B}}, \alpha_1^{\mathrm{D}}\right\}$ because α_1 cannot fall below α_1^{D}. Whenever $\alpha_{1\mathrm{E}}^i < \alpha_1^{\mathrm{E}}$, the diffusion healing of CSRO occurs (the curved green lines in **Fig. 3.12 (a)**). The healing rate can be written as $\dot{\alpha}_1^{\mathrm{H}} = \overline{\Delta\alpha} N^{\mathrm{I}} \nu_0 \exp\left[\frac{-\Delta G(T^{\mathrm{W}})}{k_{\mathrm{B}} T^{\mathrm{W}}}\right]$, where $\overline{\Delta\alpha}$ is the average of change in α_1 by each interstitial jump once in a material with N atoms, N^{I} is the total number of interstitial in this material, $\nu_0 \approx 1 \times 10^{13}$ s^{-1} is attempt frequency of the interstitial jump, k_{B} is the Boltzmann constant, and $\Delta G(T^{\mathrm{W}})$ is apparent activation free energy of the interstitial jump. Therefore, the CSRO parameter at time t after the first bombardment ($t = 0$)

can be predicted by the following equation:

$$\alpha_1(t) = \alpha_1^{\mathrm{E}}(T^{\mathrm{W}}) - \sum_i^{N^{\mathrm{B}}}(\alpha_{1\mathrm{I}}^i - \alpha_{1\mathrm{E}}^i) + \overline{\Delta\alpha} N^{\mathrm{I}} \nu_0 \exp\left[\frac{-\Delta G(T^{\mathrm{W}})}{k_{\mathrm{B}} T^{\mathrm{W}}}\right] \tag{3.5}$$

where $N^{\mathrm{B}} = \mathrm{int}(t/\Delta t) + 1$ is the number of bombardments up to time t. According to the **Eq. 3.5**, it is obvious that the competition mainly depends on the working temperature T^{W} and bombardment intensity $\Delta\alpha_1^{\mathrm{B}}$ and interval Δt.

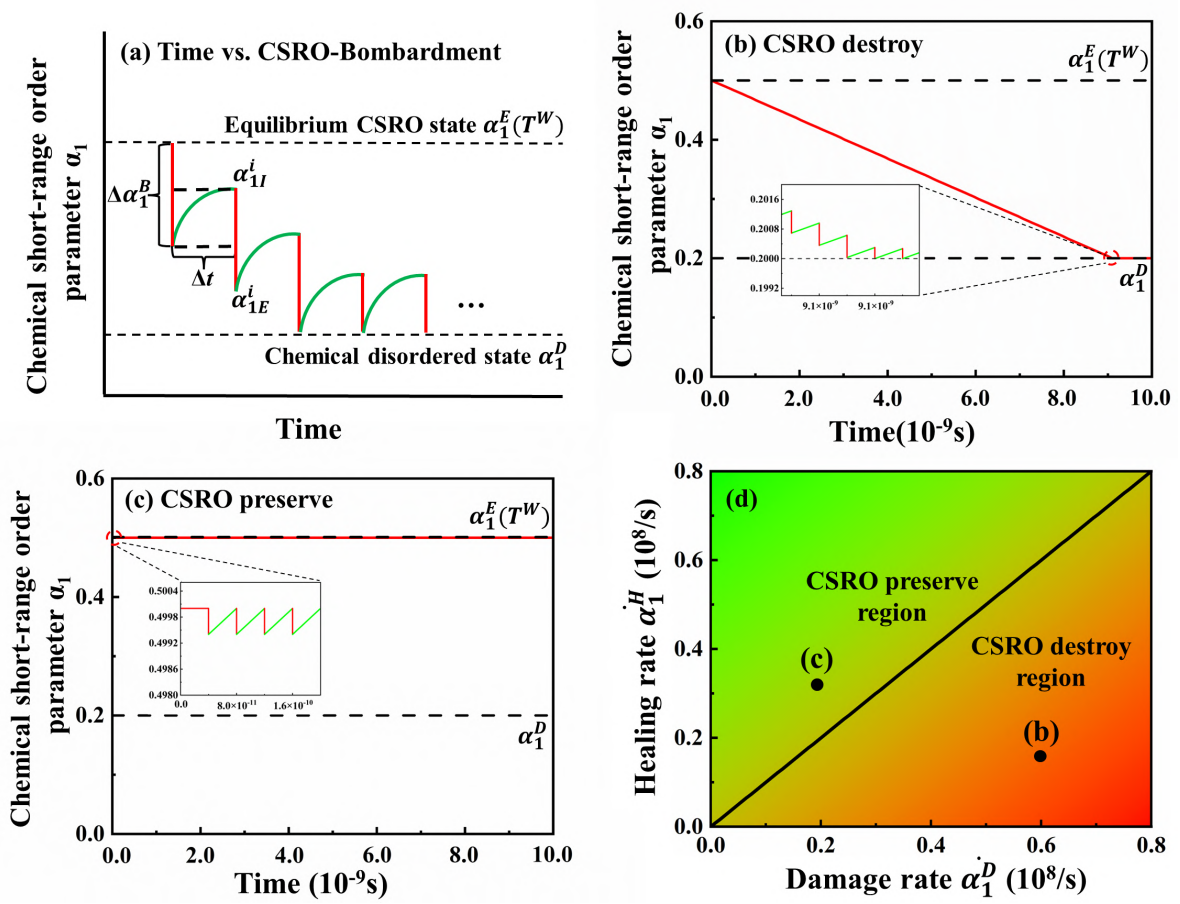

Figure 3.12: (a) Schematic Time vs. CSRO-Bombardment curve (See the main text for the details), (b) CSRO destroy case, and (c) CSRO preserve case. (d) Relationship between the healing rate $\dot{\alpha}_1^{\mathrm{H}}$ and damage rate $\dot{\alpha}_1^{\mathrm{D}}$). "(b)" and "(c)" are showing the condition used to compute figures (b) and (c), respectively.

Fig. 3.12 (b), (c) show the CSRO parameter changes calculated by **Eq. 3.5** in two different cases at working temperature $T^{\mathrm{W}} = 1100$ K, such as damage rate $\dot{\alpha}_1^{\mathrm{D}}$ dominant: CSRO destroy (b) and healing rate $\dot{\alpha}_1^{\mathrm{H}}$ dominant: CSRO preserve (c), as

shown in **Fig. 3.12 (d)**. Here we set the equilibrium CSRO state α_1^{E} and chemical disordered state α_1^{D} to 0.5 and 0.2, respectively [**46, 95**]. The apparent activation free energy of interstitial jump $\Delta G(T^{\mathrm{W}})$ is found in the **Appendix A**. According to our previous study, in the model with 256,000 atoms, the average of CSRO change $\overline{\Delta\alpha}$ by each interstitial jump once is calculated as 10^{-5}, the defect concentration in the equilibrium state is 0.4%, and the $\Delta\alpha_1^{\mathrm{B}}$ is a constant of 0.006 [**104**]. When $\dot{\alpha_1^{\mathrm{H}}} > \dot{\alpha_1^{\mathrm{D}}}$, the existence of the CSRO structure can be maintained for an extended period, thus better radiation resistance can be maintained.

3.4 Conclusion

The chemical ordering effect on the radiation resistance of a CoNiCrFeMn HEA was investigated by using combined atomic simulations that included MC and MD simulations. Radiation damage simulations were performed in three different initial CSRO status models. Defects evolution and thermodynamics behavior were analyzed after irradiation simulation. Our results showed that the annealing temperature of the CoNiCrFeMn HEA, which leads to temperature dependent chemical ordering, strongly influences the radiation resistance. The model with CSRO was found to have better radiation resistance while the model with Cr-rich region showed faster defects evolution. Interstitial diffusion results suggested that the CSRO could inhibit interstitial diffusion, which may be the key facto of better radiation resistance. Finally, we proposed a CSRO radiation damage – diffusion healing competition model. The important results in this chapter can be concluded as following:

- Warren-Cowley parameter was used to describe the chemical ordering degree. The hybrid MD-MC annealing simulation results show that annealing at a lower temperature of 600 K forms an initial stage Cr-rich region in CoNiCrFeMn HEA due to a strong chemical ordering-driven phase decomposition; whereas, annealing

at a higher temperature of 1100 K, the Cr-rich region disappear and forms the CSRO structure.

- MD radiation damage simulation shows that the Cr-rich region formed by 600 K annealing accelerates the aggregation and the evolution of defects, facilitating more dislocation loops formation. On the other hand, the CSRO structure formed by 1100 K annealing effectively delays the growth of defect number and tends to reduce the dislocation density and defect diffusion, suggesting better radiation resistance. However, the CSRO structure is destroyed by radiation, thus these advantages of CSRO will disappear in due time if CSRO cannot heal.

- We proposed a CSRO radiation damage – diffusion healing competition model, which demonstrates that the CSRO and the key anti-damage mechanisms can be maintained at the working temperature of 1100K under a relatively lower damage rate. If we can tune the CSRO formation temperature to the working temperature by controlling the chemical composition of a HEA, we may obtain high radiation resistance for an extended period.

Chapter 4

Chemical ordering structure and its effect on interstitial and vacancy diffusion in CrCoNi medium entropy alloy

4.1 Introduction

Diffusion has always been a very important foundation issue in the materials science [**105**]. It involves atomic scale dynamics of single atom or cluster, which has a great impact on materials properties, such as plastic deformation, high temperature strength and creep properties [**106–109**]. Especially in the irradiation environment, a large number of defects will be formed after irradiation damage, and the defect diffusion behavior will affect defect recombination, damage accumulation, defect evolution, and finally change the mechanical properties of materials [**40, 110–113**]. Therefore, the properties of material are closely related to the diffusion dynamics and changing atomic diffusion behavior can also be used to control the specific properties of materials to a certain extent [**114–116**]. In the past, people had a better understanding of the diffusion mechanism of interstitial and vacancy in some simple materials, such as in pure metal and traditional alloys [**105, 115, 117**]. However, with the proposal of a new multi-principal element alloys, there is a new challenge to the cognition of defect diffusion in materials.

Multi-principal element alloys, including high-entropy alloys (HEAs) and medium-entropy alloys (MEAs), have attracted great attention because of their excellent mechanical properties [**1, 2**]. Recently studies have demonstrated that the excellent radiation resistance of H/MEAs enables them to serve for a long time in harsh environment such as high temperature, high pressure and high radiation. Therefore, they are considered to have the potential to become the next generation of nuclear structure materials [**48, 49, 52**]. During the irradiation, high energy particle will produce a large number of interstitial and vacancy defects. The further evolution of interstitial and vacancy by diffusion will lead to the formation of defect clusters, dislocations and voids, which will eventually cause the material failure by embrittlement and swelling. Therefore, diffusion of interstitial and vacancy is the origin of structure damage after radiation damage.

The excellent radiation resistance of H/MEAs are closely related to the atomic diffusion dynamics in H/MEAs, and sluggish diffusion effect is suggested to be the key factor. Lu et al. demonstrate the delayed formation of dislocation in NiCoFeCrMn due to the sluggish diffusion effect [**40**]. Zhao et al. also found that mass transport in NiCoCr shows sluggish diffusion phenomenon, which may improve the radiation resistance [**118**]. However, the mechanism of sluggish diffusion is still unknown and controversial. For example, Tsai et al. reported that experimental results show the diffusion coefficient in the CoCrFeMnNi HEAs is lower, and the activation energy is higher than those in the reference metals [**26**]. However, Vaidya et al. concluded that diffusion in CoCrFeNi and CoCrFeMnNi HEAs is not inevitably sluggish and can be even enhanced at a given absolute temperature [**28**]. A recent theoretical also work pointed out that there is no relationship between configuration entropy and sluggish diffusion in HEAs, and the short-range order may contribute to sluggish diffusion [**119**]. All the results suggest that the sluggish diffusion effect in H/MEAs needs further study.

Currently, some works pointed out that chemical ordering structures will be formed in H/MEAs after annealing at a certain temperature, which may affect the interstitial and vacancy diffusion behavior and radiation resistance [**97, 120, 121**]. Especially, an experimental work pointed out that the local chemical order in CrCoNi can delay the formation and evolution of interstitial and vacancy, and the radiation resistance was improved at relatively low irradiation doses [**121**]. Their simulation results showed that local chemical order can reduce interstitial and vacancy diffusivity by increasing diffusion energy barriers and reducing diffusion correlation factor, which can promote the recombination of interstitial and vacancy. However, this simulation is still controversial because of the realistic chemical ordering structures and diffusion energy in chemical ordering CrCoNi is not well described by EAM potential [**89**]. In fact, the chemical ordering structures has not been clarified yet even experimentally. Zhang et al. [**92**] first reported the observation of short-range order structural features in CrCoNi and found

the increasing stacking-fault energy and hardness. By using atom probe tomography, Inoue et al. [**122**] found that 001 Cr-rich atomic layers and 001 Ni/Co-rich atomic layers tended to align mutually in CoCrNi. However, from electron diffraction and atomic-resolution chemical mapping, Zhou et al. [**123**] provided the evidence that chemical order structures present 113 Cr-rich atomic layers and Ni/Co-rich atomic layers under [112] zone axis in CoCrNi.

In our previous work, a machine learning neural-network potential (NNP) based on the DFT training dataset has been developed to accurately describe interatomic interaction of CrCoNi MEA. We are able to not only successfully specify realistic chemical ordering structures, but also predicted its formation kinetics in CrCoNi through simulations by using this newly developed potential [**34,124**]. In this work, we demonstrated the distribution of realistic chemical ordering structures in CrCoNi and interstitial diffusion molecular dynamics (MD) simulation and vacancy jump kinetic Monte Carlo (kMC) simulation were performed to quantitatively analyses the chemical order impact on interstitial and vacancy diffusion by using NNP. All the simulations were performed by Large-scale atomic/molecular massively parallel simulator (LAMMPS) code [**62**]. Our results indicate that chemical order enhances sluggish diffusion by restricting interstitial and vacancy diffusion regions.

4.2 Simulation method and model details

4.2.1 Kinetic Monte Carlo simulation

The vacancy jump kinetic Monte Carlo (kMC) simulation was used to perform the annealing process and vacancy diffusion in CrCoNi. One vacancy was introduced in the model. In the FCC structure, vacancy will jump to one of the 12 nearest neighbor lattice sites, and this was taken as one kMC event. The jump frequency of vacancy was calculated as $v_i = v_0 \exp\left(\frac{-\Delta E_i}{k_B T}\right)$, where $v_0 = 1 \times 10^{13}$ s^{-1} is an attempt frequency

and taken as the typical vibrational frequency here. ΔE_i is the barrier of vacancy jump to the nearest neighbor site i, this barrier is given by the artificial neural network (ANN) prediction, which could significantly accelerate the kMC simulation, especially when performing long time kMC simulations. k_{B} is the Boltzmann constant, and T is the absolute temperature. The incubation time for a vacancy jump was calculated as $\Delta t_{\mathrm{kmc}} = \frac{\overline{\ln(1/s)}}{\sum_{i=1}^{12} v_i}$, where s is a random number between 0 and 1. It should be noted that the equilibrium vacancy concentration is temperature dependent, $C_{\mathrm{v}}^{\mathrm{eq}} = \frac{N_{\mathrm{v}}}{N} = \int_{-\infty}^{+\infty} P(E_f^i)\exp\left(-\frac{E_f^i}{k_{\mathrm{B}}T}\right) dE_f^i$, where N_{v} is the number of vacancy, $N = 2916$ is the total number of atoms in the model. $P(E_f^i)$ is the probability of vacancy formation energy at site i is E_f^i [**125**]. Therefore, the annealing time can be calculated as $t_{\mathrm{a}} = \frac{c_{\mathrm{v}}}{c_{\mathrm{v}}^{\mathrm{eq}}(T)} \sum(\Delta t_{\mathrm{kmc}})$, where $c_{\mathrm{v}} = \frac{1}{N}$ is the actual vacancy concentration in the annealing simulation.

4.2.2 Interstitial diffusion simulation

Interstitial was introduced in the models to perform the interstitial diffusion simulations. The total number of atoms in the initial model was 2916. Periodic boundary conditions were used along x, y, and z directions, and timestep was 0.001 ps. NPT ensemble was adopted with temperature and pressure controlled by Nosé-Hoover thermostat [**126**]. An atom was randomly inserted as interstitial defect and interstitial will migrate by constantly forming new dumbbell pairs with surrounding lattice atoms. The total time of each diffusion simulation was 1 ns, the simulation temperature was set at $T = 1200$ K in order to get sufficient diffusion behavior within the limited simulation time window. The MSD was calculated as $\langle R^2(t)\rangle = \frac{\sum_i^N |\boldsymbol{R}_i(t) - \boldsymbol{R}_i(0)|^2}{N}$, where $\boldsymbol{R}_i(t)$ and $\boldsymbol{R}_i(0)$ are the position vectors of atom i at time t = t and t = 0, respectively. $N = 2916$ is the total number of atoms in the model. Interstitial diffusivity can be evaluated by calculating the slope of MSD – time curve. OVITO was used to visualize our simulation results, and the WS method was used to identify the position of interstitial defects.

4.2.3 Chemical domain structure identifying

Chemical domain structure matching analysis was used to identify all the chemical domain structures in the models. A matching degree was defined for an atom site i as $M_i^{\mathrm{I_d}} = \max_{\{\mathrm{I_d},\mathrm{T_{I_d}}\}} \frac{1}{N_{\mathrm{I_d}}} \sum_{K=1}^{N_{\mathrm{I_d}}} \delta_{\alpha(K)\beta(K)}$ in the model, where $\mathrm{I_d}$ represents the chemical domain motif type (e.g., motif type I: the Cr/CoNi layers are along [110] direction), $\mathrm{T_{I_d}}$ represents the space group operation (e.g., rotate the motif at different angles) of chemical domain motif $\mathrm{I_d}$, $N_{\mathrm{I_d}}$ represents the number of atom sites in the chemical domain motif type $\mathrm{I_d}$. $\alpha(K)$ represents element type at site K in the chemical domain motif, and $\beta(K)$ represent the actual element type at site K in the model. δ is Kronecker delta, which means if $\alpha(K) = \beta(K)$, then $\delta_{\alpha(K)\beta(K)} = 1$, otherwise $\delta_{\alpha(K)\beta(K)} = 0$. When $M_i^{\mathrm{I_d}} > 0.85$, we define site i belongs to the chemical domain motif type $\mathrm{I_d}$. This matching analysis method has been successfully used to find out the chemical domain structures in our previous work [**34**].

4.2.4 Mesh region division

Mesh region division was used to calculate defect residence time and chemical degree of each small mesh region. A 36 × 36 × 36 mesh was used to divide our model into small mesh regions. We assume the chemical ordering degree $\overline{P_k^{\mathrm{I_d}}} = \frac{n_k^{\mathrm{I_d}}}{N_k}$ of each mesh region is constant during defect diffusion, where k is the index of mesh region, $\mathrm{I_d}$ ($\mathrm{I_d}$= I, II, III and Other in this work) is the chemical ordering type, $n_k^{\mathrm{I_d}}$ is the number of type $\mathrm{I_d}$ atoms near mesh region k (within first nearest neighbor), N_k is the total number of atoms near mesh region k, and $0 \leq \overline{P_k^{\mathrm{I_d}}} \leq 1$, $\sum_{\mathrm{I_d}} \overline{P_k^{\mathrm{I_d}}} = 1$. A conditional function is defined as $C_k(\boldsymbol{r}) = \begin{cases} 1, \boldsymbol{r}(t) \in \Omega_k \\ 0, \boldsymbol{r}(t) \notin \Omega_k \end{cases}$ to count the time of defect residence in mesh k. where $\boldsymbol{r}(t)$ is the defect (interstitial or vacancy) position at time t, Ω_k is the region of mesh k. We sample the defect position at time t, and if the defect located in the mesh region Ω_k, we count this region once. Therefore, the normalized total defect residence

time in mesh k can be calculated as $Q_k = a\int_0^{t^{\mathrm{F}}} C_k(\boldsymbol{r}(t))\Delta t\ dt$, where $a = \frac{n}{t^{\mathrm{F}}}$ is the normalization factor, $t^{\mathrm{F}} = \sum_{k=1}^{n} Q_k$ is the total simulation time, n is the total number of mesh, and Δt is the sampling interval. It should be noted that, for the interstitial diffusion simulation, the sampling interval $\Delta t = 0.5$ ps is constant. However, for the vacancy diffusion simulation, since the kMC jump time Δt_{kmc} is not constant. the actual residence time of vacancy in each mesh should be calculated based on the kMC jump time. Finally, the correlation factor of defect residence time and chemical ordering type $\mathrm{I_d}$ region was defined as $\overline{G^{\mathrm{I_d}}} = a\frac{1}{n}\sum_k^n \overline{P_k^{\mathrm{I_d}}} Q_k$. A higher correlation factor $\overline{G^{\mathrm{I_d}}}$ indicates that defects prefer to diffuse in the chemical ordering type $\mathrm{I_d}$ region.

4.2.5 Chemical ordering parameter

Warren–Cowley parameter $\alpha_n^{ij} = 1 - \frac{P_n^{ij}}{C_j}$ was used to descript the CSRO parameters for all the element pairs during kMC annealing simulation and hybrid MD - MC simulation [**98**], where i and j refer to the elements, and n refers to the nth nearest neighbor. P describes the probability of occurrence of each element as a surrounding atom, and C is the systemwide mean concentration of the corresponding element. A positive value indicates a tendency of repulsion pairs of each other (e.g., Cr-Cr and Co-Ni pairs have a positive parameter in this work), while negative value indicates a tendency of attraction with each other (e.g., the Cr-Co and Cr-Ni pairs have a negative parameter in this work). If the value equal 0, which means the i and j element pairs are randomly distributed, and no chemical ordering existed.

4.3 Results and discussion

4.3.1 Formation of chemical structures by thermal annealing

According to the Time - Temperature - α diagram reported in our previous work, the formation of chemical ordering structures depends on the annealing temperature

and time [**34**]. Therefore, by controlling the annealing time, we can construct models with different degree of chemical order for the investigation of chemical order impact on interstitial and vacancy diffusion. Specifically, the isothermal annealing simulation was performed in CrCoNi by using kMC vacancy diffusion with different annealing time at temperature of $T = 673$ K, at which temperature significant growth of chemical order is expected in a reasonable annealing time. By using the NNP, chemical ordering structures were found in our kMC annealing simulation. All the chemical ordering structures were identified by the chemical ordering matching analysis. **Fig. 4.1 (a)** shows the distribution of chemical ordering structures in random CrCoNi model and after annealing for 8 min, 22min, 5.5 h, 7.8h, and 10.7h, respectively, labeled as Model 1-5 in this work. The chemical ordering structures formed soon after initial annealing simulation and increased with annealing time. Even after 8 min annealing, a certain volume of chemical ordering structures can be found in the model. After 10 h annealing, the volume of chemical ordering structures already occupies a large part of the model. This is consistent with the results predicted by the Time - Temperature - α diagram. **Fig. 4.1 (b)** show the distinguishing feature of three chemical ordering structures, labeled as Motif type I, II and III in this work. The red spheres represent Cr atoms and gray spheres represent Co and Ni atoms. The Cr-rich and Co/Ni-rich layers of the motif structures are oriented along 110, 100 and 113 directions for type I, II and III, respectively. Of these, type I has a pattern of Immm symmetry and Cr atoms have a tendency to form cluster. Type II is similar to the $L1_0$ structure, where Cr atoms are inclined to cluster in one layer and Co/Ni atoms in another. Type III is an $L1_1$ structure where Cr atoms form cluster on the eight vertices of the motif structure. These features of the chemical ordering structures are consistent with our previous finding by using NNP [**34**].

To describe the chemical order trends during the kMC annealing simulation, we further investigated the variations in chemical ordering parameters and chemical mo-

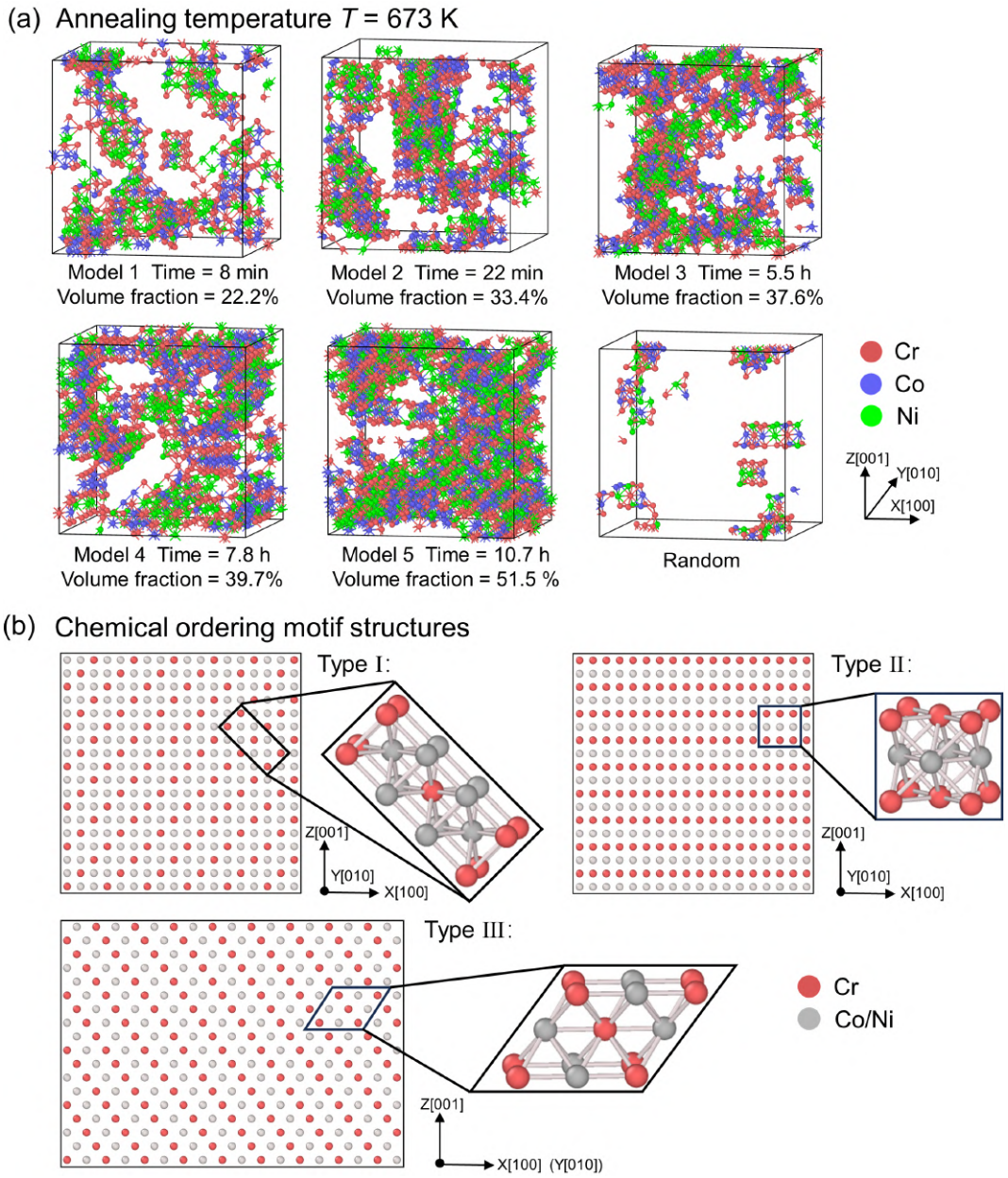

Figure 4.1: (a) Distribution of chemical ordering structures after annealing for different time. (b) Structure information of three chemical ordering motifs (the red spheres represent Cr atoms, and the gray spheres represent Co/Ni atoms).

tif structures volume fraction. Details of five models are summarized in **Tab. 4.1**. As shown in **Fig. 4.2 (a)**, chemical ordering parameters initially increased rapidly, indicating the fast formation of chemical ordering structures during annealing. After a total annealing time of about 11 h, the Cr-Cr and Co-Ni pairs exhibited a positive chemical ordering parameter of 0.38 and 0.25, respectively, indicating a tendency of repulsion. In the contrast, the Cr-Co and Cr-Ni pairs exhibited a negative parameter of -0.22 and -0.14, respectively, indicating a tendency of attraction. These trends are in agreement with the DFT results [**91**], showing the reliability of NNP. **Fig. 4.2 (b)** shows the chemical motif structure volume fraction in the five models with different chemical ordering degree. The volume fraction is calculated by $f_{\mathrm{v}}^{\mathrm{Id}} = m^{\mathrm{Id}}/N$, where m^{Id} is the number of atoms belong to at least one chemical motif structure discriminated by chemical ordering matching analysis and N is the total number of atoms in the model. It should be noted that some atoms may belong to multiple chemical ordering types concurrently. The motif type I and type II demonstrated an increase in chemical motif structure volume fraction with annealing time, especially, the volume fraction of motif type I structure has increased to nearly 39.6% after 10.7 h annealing, and a large size of chemical domain structures was present in CrCoNi, while the motif type III exhibited gradual decrease. The decrease of type III is attributed to the fact that the motif type III is unstable and gradually decomposes with increasing annealing time, as reported by Zhou et.al [**123**].

Table 4.1: Annealing time, chemical ordering structure volume fraction, and chemical ordering parameter of Cr-Cr in five models.

Name	Annealing time	Volume fraction	Parameter α_1^{CrCr}
Model 1	8 min	22.2%	0.25
Model 2	22 min	33.4%	0.31
Model 3	5.5 h	37.6%	0.35
Model 4	7.8 h	39.7%	0.35
Model 5	10.7 h	51.5%	0.38

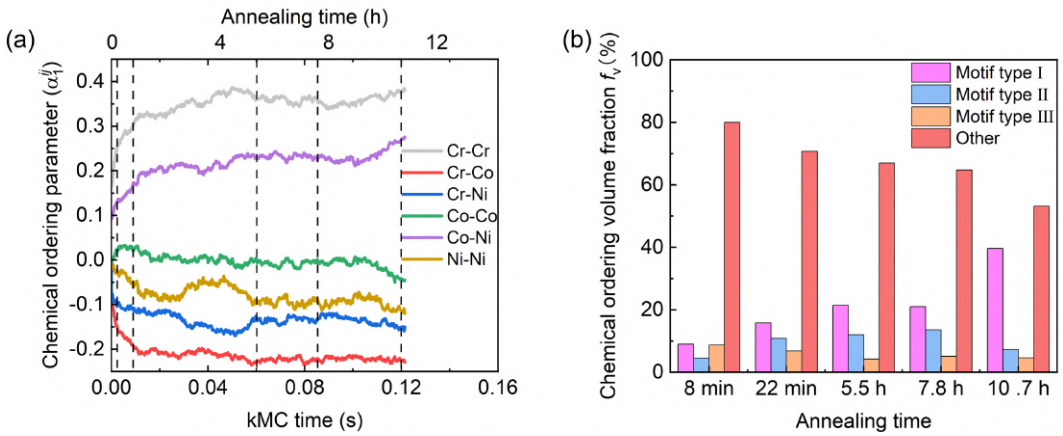

Figure 4.2: (a) Chemical ordering parameter changes during kMC annealing simulation. (b) Chemical motif structure concentrations at different annealing time, the label "Other" represents random structures without chemical ordering.

4.3.2 Chemical ordering impact on interstitial and vacancy diffusion

Interstitial diffusion MD simulation and vacancy jump kMC simulation were performed in five models with different chemical ordering degree and then compared to the random model (without chemical ordering). For the interstitial diffusion, an atom was randomly inserted in the models, and the diffusion temperature was set to T = 1200 K to ensure that a sufficient diffusion process was obtained within a MD simulation time of 1 ns with no significant change in chemical ordering (see **Appendix B** for the chemical ordering change during diffusion simulation). For the vacancy diffusion, given the higher migration barrier of vacancy, kMC simulations were used to investigate the chemical ordering effect on vacancy diffusion over a suitable timescale. A vacancy was created by deleting the atom and the kMC simulation temperature was also set to T = 1200 K, and total 2000 vacancy jumps were performed.

Fig. 4.3 (a) - (b), (d) - (e) show the interstitial and vacancy diffusion trajectories (red lines) in Model 5 and random model, respectively. For interstitial diffusion, the length of trajectories in Model 5 is significantly smaller than that in the random model for the same diffusion simulation time. For vacancy diffusion, the length of trajectories

is similar in two models because the same number of vacancy jumps were performed, but the time required to complete the jumps is much longer in Model 5 (see **Appendix B** for the vacancy jump time). Therefore, the formation of chemical ordering reduced interstitial and vacancy diffusion. Furthermore, we note that the distribution of interstitial and vacancy diffusion trajectories is inhomogeneous in Model 5, whereas it is more random in the random model. This suggests that chemical ordering may also affect diffusion regions. Details will be discussed in the next section. To quantify the diffusion of interstitial and vacancy, the average mean squared displacement (MSD) of interstitial and vacancy were calculated for all models and the slope of the MSD-time curves were used to calculate diffusivity. **Fig. 4.3 (c), (f)** show the MSD results of the interstitial and vacancy, respectively. The diffusivity of interstitial and vacancy in all the models are calculated and summarized in **Tab. 4.2**. Obviously, all the chemical ordering models show lower MSD slopes compared to the random model, and the MSD slopes decreased with increasing chemical ordering (annealing time). Specifically, in the random model, the interstitial and vacancy diffusivity were calculated to be 3.6×10^{-10} m^2/s and 8.8×10^{-14} m^2/s, respectively. while in the Model 5, the interstitial and vacancy diffusivity were calculated to be only 2.0×10^{-10} m^2/s and 3.1×10^{14} m^2/s, respectively. It is clear that chemical ordering model shows much slower interstitial and vacancy diffusivity compared with the random model, the chemical ordering structures formed after annealing efficiently reduced the interstitial and vacancy diffusion, promoting a strong sluggish diffusion effect, and this effect increases with the chemical ordering degree.

4.3.3 Relationship between chemical ordering structures and diffusion region

To validate our hypothesis that the chemical ordering structures in the annealed models can restrict interstitial and vacancy diffusion region, we performed additional

Table 4.2: Interstitial and vacancy diffusivity in all models.

Name	Interstitial diffusivity (m^2/s)	Vacancy diffusivity (m^2/s)
Random 5	3.6×10^{-10}	8.8×10^{-14}
Model 1	2.9×10^{-10}	5.1×10^{-14}
Model 2	2.7×10^{-10}	4.2×10^{-14}
Model 3	2.4×10^{-10}	3.4×10^{-14}
Model 4	2.3×10^{-10}	3.3×10^{-14}
Model 5	2.0×10^{-10}	3.1×10^{-14}

diffusion simulations to investigate the correlation between interstitial or vacancy diffusion region and the distribution of chemical ordering structures. Specifically, we carried out 50 independent interstitial and vacancy diffusion simulations in Model 5 and random model for comparison (see **Appendix B** for the results of random model), with each simulation from different initial interstitial or vacancy positions. The mesh region division was used to calculated interstitial and vacancy residence density in each small mesh region and the chemical ordering degree of each small mesh region. It should be noted that since the interstitial forms a dumbbell pair structure during diffusion, the mass center of the dumbbell pairs was used as the position of interstitial. In addition, we guess that the average interstitial and vacancy formation energies depend on the chemical ordering structures, which will affect the residence time during diffusion. Therefore, interstitial and vacancy formation energy were also calculated in both models by $E^{\mathrm{f}}_{\mathrm{defect}} = E_{\mathrm{defect}} - E_{\mathrm{perfect}} \pm \mu$, where $E^{\mathrm{f}}_{\mathrm{defect}}$ is the formation energy of interstitial or vacancy, E_{defect} is the total energy with interstitial or vacancy, E_{perfect} is the total energy without defect and μ is the chemical potential of interstitial or vacancy atom (see **Appendix B** for interstitial and vacancy formation energy distributions). In order to avoid the influence of small model sizes or possibly specific structures on the results, we annealed three samples with different initial structures to a same chemical ordering degree (same degree as Model 5) and repeated the interstitial and vacancy diffusion simulations. In addition, the same simulations were performed in the models

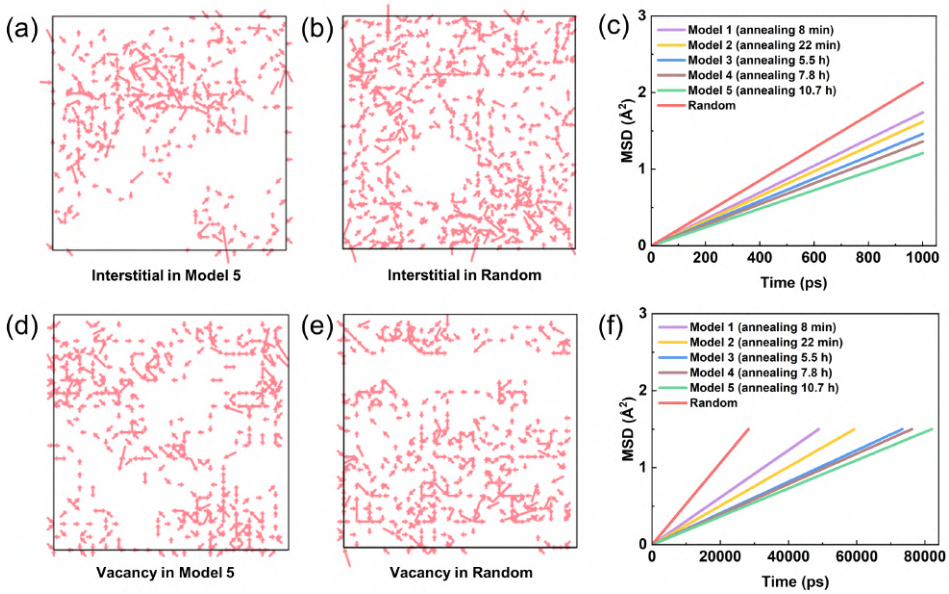

Figure 4.3: (a)-(b) Interstitial diffusion trajectories (red lines) in Model 5 and random model, respectively. (c) The MSD- time curve of interstitial in all models. (d)-(e) Vacancy diffusion trajectories in Model 5 and random model, respectively. (f) The MSD-time curve of vacancy in all models.

with lower chemical ordering degree (same degree as Model 3), details are described in **Appendix B**.

Fig. 4.4 (a) and (b) show one slice of chemical ordering degree $\overline{P_k^{\mathrm{Id}}}$ of type I and other (no chemical ordering) structures contour map in the Model 5, respectively. Since the Model 5 forms mainly chemical ordering type I structure, here we focus only on its the chemical ordering degree. **Fig. 4.4 (c) and (d)** show one slice of the interstitial and vacancy residence density Q_k contour maps in the Model 5, respectively. The higher residence density represents that interstitial and vacancy prefer to stay and diffuse in this region. To ensure that 50 independent diffusion simulations is sufficient to obtain interstitial and vacancy residence density information, we checked the root mean square error (RMSE) of the density results, which indicates that 50 separate diffusion simulations had converged (details can be found in the **Appendix B**). The residence density results show that the distribution of interstitial and vacancy residence density is inhomogeneous in the Model 5, with higher residence density in certain regions in

particular, indicating that interstitial and vacancy tend to diffuse preferentially in these regions. In contrast, the residence density in the random model is more homogeneous, with defects showing random diffusion in each region (see **Appendix B** for residence density in the random model). By comparing the interstitial and vacancy residence density maps and the chemical ordering degree of type I and other structures regions, a large overlap between the mesh region with higher interstitial and vacancy residence density and the mesh region with higher chemical ordering degree of other structures was found, suggesting that defect tend to diffuse in regions without chemical ordering structures (random structure). In other words, the formation of chemical ordering structures can restrict defect diffusion region. Finally, the interstitial and vacancy formation energy were calculated and shown in **Fig. 4.4 (e) and (f)**, respectively. We found that the interstitial and vacancy formation energy are higher in the region where chemical ordering structures is formed, and interstitial and vacancy tend to diffuse in the regions without chemical ordering, which explains why chemical ordering structures can restrict interstitial and vacancy diffusion regions.

To quantify the relationship between interstitial and vacancy diffusion regions and the distribution of chemical ordering structures, the average correlation factors between chemical ordering degree $\overline{P_k^{\mathrm{I_d}}}$ and residence density Q_k was calculated as $\overline{G^{\mathrm{I_d}}} = a\frac{1}{n}\sum_k^n \overline{P_k^{\mathrm{I_d}}} Q_k$. The correlation factors of interstitial (vacancy) for type I and other structures were calculated as 0.33 0.32) and 0.59 (0.62), respectively. The interstitial and vacancy residence densities are significantly more correlated with the other structures, which also proves that interstitial and vacancy prefer to diffuse in the region without chemical ordering structures. Therefore, all these results further confirm that the formation of chemical ordering structures in Model 5 leads to the inhomogeneous distribution of interstitial and vacancy diffusion trajectories, as previously shown in **Fig. 4.3 (a)** and **Fig. 4.4 (a)**. In summary, our interstitial and vacancy diffusion simulation results demonstrate that the chemical ordering structures formed after an-

nealing in CrCoNi lead to the sluggish diffusion phenomenon. One of the key reasons for the sluggish diffusion is the restriction of the defect diffusion region caused by the formation of chemical ordering structures.

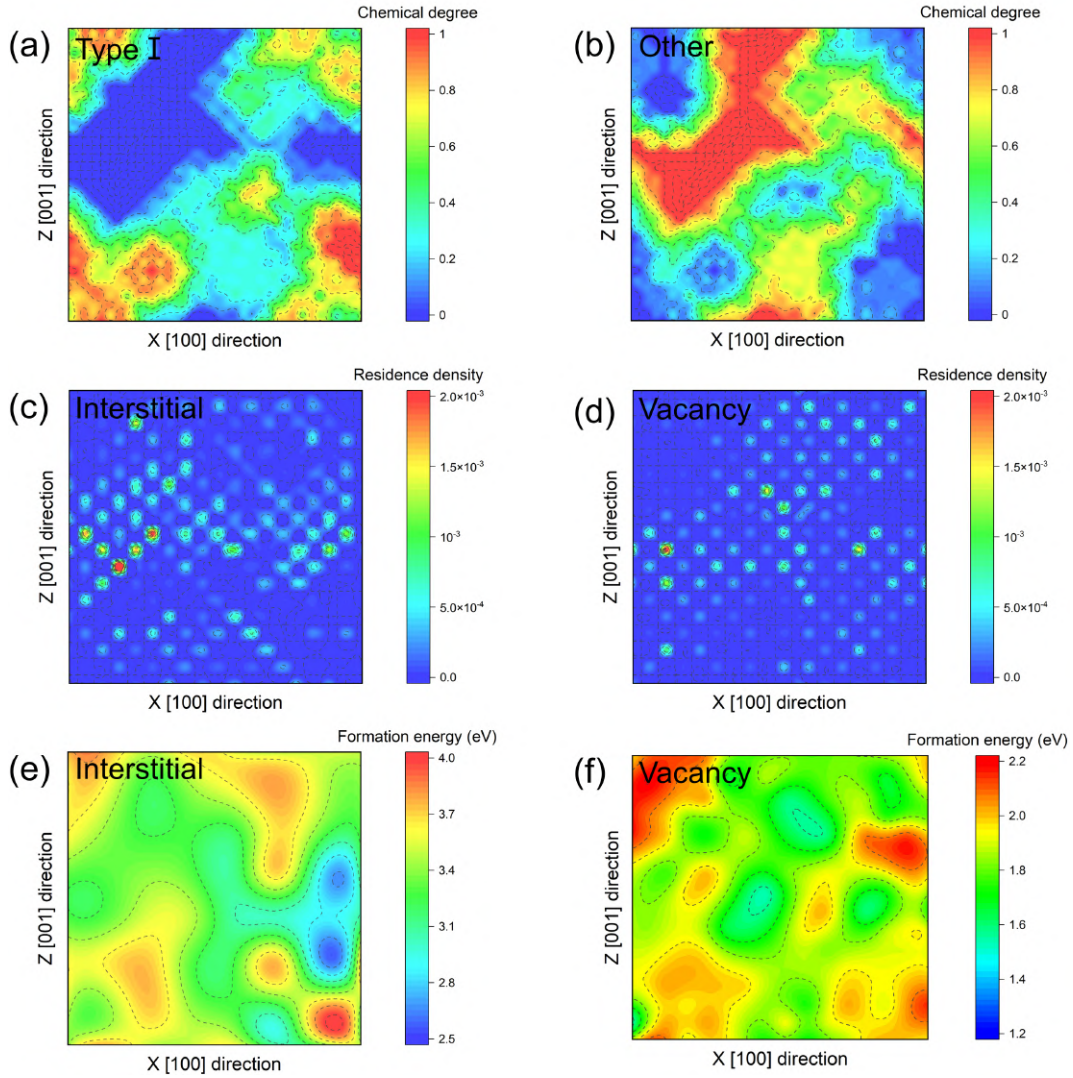

Figure 4.4: (a) - (b) Slice of chemical degree distribution contours of chemical ordering type I and other structures in the Model 5, respectively. (c)-(d) Slice of interstitial and vacancy residence density contours in the Model 5, respectively. The average correlation factors between chemical ordering degree of type I and other and interstitial (vacancy) residence density were calculated as 0.33 (0.32) and 0.59 (0.62), respectively. (e) - (f) Slice of interstitial and vacancy formation energy contours in the Model 5, respectively.

4.3.4 Diffusion driving force from annealing and operating temperature difference

Interstitial and vacancy diffusion are only the possible processes of change of chemical ordering. Whenever if the current chemical structure is not the equilibrium structure of the operating temperature of considering H/MEA, there always exist a driving force toward the equilibrium structure, which enhances the interstitial and vacancy diffusion. Therefore, the difference between the annealing temperature T^a and the operating temperature T^o provides the driving force for defect diffusion. Specifically, in this work, the model (Model 5) was annealed to equilibrium at $T^{\mathrm{a}} = 673$ K and chemical ordering structures have formed inside, while the interstitial and vacancy diffusion simulations were performed at higher temperature $T^{\mathrm{o}} = 1200$ K. Since the chemical ordering structures are reduced at high temperature equilibrium, interstitial and vacancy diffusion is excited at higher operating temperature ($T^{\mathrm{o}} > T^{\mathrm{a}}$) and destroys the existing chemical ordering structures to reach the equilibrium at the operating temperature with reducing free energy at the operating temperature. When operating temperature is lower than annealing temperature ($T^{\mathrm{o}} < T^{\mathrm{a}}$), interstitial and vacancy diffusion is excited again and forms further chemical ordering to reach equilibrium at the operating temperature also with reducing free energy at the operating temperature.

The above discussion can be understood by the schematic diagram of the relationship between chemical ordering degree α_n^{ij} change and annealing temperature T^a and operating temperature T^o, shown in **Fig. 4.5**, which is based on the "time – temperature – chemical-ordering-degree" diagram [**34**]. The C-shaped curves in **Fig. 4.5** represent constant chemical ordering degree with different annealing time and temperature. The red arrows show the case of $T^o > T^a$. In this case, the system can quickly reach the thermal equilibrium by exiting intestinal and vacancy diffusion because of high-speed diffusion at such high temperature. The green allows show the case of $T^o < T^a$. In this case, the system tends to form more chemical ordering to reach the

equilibrium structure of the operating temperature by exiting intestinal and vacancy diffusion. It may need certain time because of the slow diffusion at the low operating temperature even excited by the driving force.

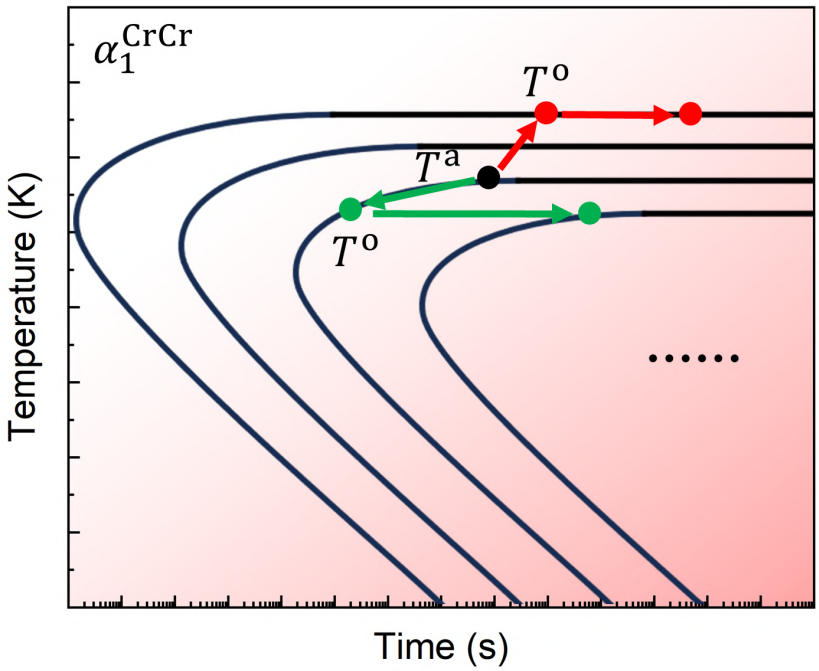

Figure 4.5: Schematic diagram of the relationship between chemical ordering degree α_n^{ij} change and annealing temperature T^a and operating temperature T^a. The same C-shaped curve represents the same chemical ordering degree. The longer the annealing time or the lower the annealing temperature, the higher the chemical ordering degree.

4.4 Conclusion

With the progress of research on the properties of H/MEAs, the effect of chemical ordering on their performances has gradually attracted attention. A lot of works has been done to investigate the chemical ordering effect on diffusion. According to current research results, it is widely believed that the formation of chemical ordering can suppress the diffusion behavior of internal defects, known as the sluggish diffusion effect [**26**]. Generally, the effect of chemical ordering on defect diffusion mainly lies in the diffusion barrier and diffusion correlation coefficient. For example, the MD simulation

result concluded that the change of diffusion barrier will lead to the vacancy trapping effect in CrCoNi and NbMoTa HEAs [**127**]. Meanwhile, the DFT calculation shows that chemical ordered structure in NiFe alloy will reduce defect jump frequencies and correlation factors, and diffusion in the ordered structure is slower [**118**]. The study on the effect of chemical ordering on the behavior of irradiation-induced defects also proves that chemical ordering structures can effectively slow down the defects evolution [**97**]. However, exactly how chemical ordering affects the migration behavior of defects has not been carefully explored.

In this work, the relationship between interstitial or vacancy diffusion and chemical ordering structures is investigated by simulations. The results indicate that, interstitial and vacancy prefer to diffuse in the region without chemical ordering structures and show sluggish diffusion phenomenon. On the other hand, the difference between annealing temperature and operating temperature will drive defect diffusion to change chemical ordering degree. Additional energy is required when diffusion destroys the chemical ordering structures. This will not only reduce interstitial and vacancy diffusivity by restrict diffusion region, but also increase diffusion barrier. In summary, we investigate the chemical ordering structure and its effect on interstitial and vacancy diffusion in CrCoNi. Our results in this chapter can be concluded as following:

- Chemical ordering structure will form in CrCoNi after annealing at certain temperature and some specific structures are able to form large size chemical domain structures. These chemical ordering structures could effectively slow down defect diffusion and lead to the sluggish diffusion phenomenon in CrCoNi.

- The mesh region division results show that interstitial and vacancy prefer to diffuse in the region without chemical ordering structure, as additional energy is required to break the chemical ordering structures. The formation of chemical ordering structures can restrict interstitial and vacancy diffusion regions.

- We proposed a schematic diagram of the effect of the difference between annealing and operating temperature on diffusion, which will drive interstitial and vacancy diffusion to change the chemical ordering degree and thus influence diffusion. These results provide help for the study of chemical ordering effect and defect diffusion dynamics in complex alloys and have a new understanding of the mechanism of sluggish diffusion effect in H/MEA.

Chapter 5

Conclusion and outlook

5.1 Main conclusion of this dissertation

In this dissertation, we focused on studying the radiation resistance of high/medium entropy alloys (H/MEAs) by multiple simulation methods. H/MEAs as new proposed materials have attracted extensive attention because of their outstanding properties, such as high strength, high tensile ductility and good corrosion. In contrast to traditional alloys, which contain only one or two principal elements, H/MEAs contain more principal elements, the properties of H/MEAs can also be greatly improved by adjusting the types and proportions of elements. In particular, their excellent radiation resistance makes them possible to be applied to the development of the next-generation nuclear energy and contributes to the development of sustainable energy sources. However, the mechanism of radiation resistance and defect behavior of H/MEAs have not been fully understood at the atomic scale, especially the high-temperature working conditions will bring another challenge for the H/MEAs as a material to be used in nuclear facilities.

In order to better understand the properties of H/MEAs and facilitate the development of high-performance H/MEAs, we have used a variety of atomic simulation methods, including density function theory (DFT), molecular dynamic (MD) and Monte Carlo (MC) to systematically study the surface radiation resistance and internal defects evolution of CoNiCrFeMn HEA. We have also further studied the chemical ordering effect on the radiation resistance of CoNiCrFeMn HEA, as well as the chemical domain structure in CrCoNi MEA and its effect on defect diffusion behavior. It is hoped that our work will provide theoretical guidance on the understanding of the radiation resistance of H/MEAs and the motions of irradiation defects, thus contributing to the future design of materials with better radiation resistance and the development of other materials with superior properties.

In Chapter 1, we briefly introduced the definition and the special properties of H/MEAs. Several commonly used simulation methods are presented and it is suggested how they can be used to address the key issue in the research of H/MEAs. The structure

of this dissertation is also explained.

In Chapter 2, surface radiation results show that compared to pure Ni, CoNiCrFeMn HEA has less defects during a single primary knock-on atom (PKA) process, and the average depth of defects distribution is shallower. For the consecutive radiation bombardments, CoNiCrFeMn HEA also exhibits much higher surface radiation resistance. Even under extreme irradiation flux, the number of defects in CoNiCrFeMn HEA is much less and stable, appearing to be insensitive to the number of bombardments and suggesting good surface radiation resistance, while in the pure Ni, the formation of dislocation will lead to a boost of defects. As for the internal radiation results, compared to pure Ni, less defects are produced in the CoNiCrFeMn HEA. Only a few small dislocations are observed, and the length of dislocation is also small. The interstitial cluster have much smaller mean free path (MFP) and exhibit a 3-D motion during migration. Specially, for an interstitial cluster containing 10 atoms, the MFP was reduced over 40 times compared to that in pure Ni. The small MFP and 3-D motion of interstitial cluster in HEA will increase the opportunity of recombination of interstitial and vacancy, which may explain the mechanism of good radiation resistance in CoNiCrFeMn HEA.

In Chapter 3, we focused on the chemical ordering effect on the radiation resistance of CoNiCrFeMn HEA. H/MEAs have generally been considered to occupy a random solid solution state, but the degree of randomness of the distribution of atoms in HEAs remains to be fully determined. Some studies have reported that chemical short-range order (CSRO) structure was expected to develop after HEAs annealing at a particular temperature, with possibly significant impacts on the HEAs structural stability and mechanical properties. Therefore, we further studied the chemical ordering of CoNiCrFeMn HEA and its effect on radiation resistance. The hybrid MD–MC annealing simulations at various temperatures followed by MD irradiation simulations are performed to the annealed samples. The annealing simulation results show that an initial stage Cr-rich region will form in CoNiCrFeMn HEA at a lower temperature of 600 K;

whereas, annealing at a higher temperature of 1100 K will form a chemical short-range order (CSRO). MD radiation damage simulation shows that the Cr-rich region accelerates the aggregation and evolution of defects, facilitating more dislocation formation, and the radiation resistance of CoNiCrFeMn HEA is reduced. On the other hand, the CSRO effectively delays the growth of defect number and tends to reduce the dislocation density and defect diffusion, suggesting enhanced radiation resistance. However, the enhanced radiation resistance did not persist long because that the CSRO structure will be destroyed by radiation damage. Therefore, the chemical structures of HEAs including CSRO and its formation temperature should be carefully evaluated, especially when it is used as a radiation resistance material at various working temperature. We also propose a CSRO radiation damage – diffusion healing competition model, which demonstrates that the CSRO and the key anti-damage mechanisms can be maintained at the working temperature of 1100K under a relatively lower damage rate. If we can tune the CSRO formation temperature to the working temperature by controlling the chemical composition of a HEA, we may obtain high radiation resistance for an extended period. These results can help us to better understand and design radiation resistance HEAs with CSRO enhanced effect.

In Chapter 4, chemical ordering structure and its effect on interstitial and vacancy diffusion are studied in CrCoNi MEA. Defect diffusion has always been a very important foundation issue in the materials science, which has a great impact on materials properties, such as plastic deformation, high temperature strength and creep properties. Especially in the irradiation environment, a large number of defects will be formed after irradiation damage, and the defect diffusion behavior will affect defect recombination, damage accumulation, defect evolution, and finally change the mechanical properties of materials. Therefore, the properties of material are closely related to the diffusion dynamics and changing atomic diffusion behavior can also be used to improve the radiation resistance of H/MEAs. In this work, a machine learning neural network potential

(NNP) based on the DFT training dataset is used to accurately describe interatomic interactions in CrCoNi MEA. After annealing below 800 K, long-range chemical domain structures have been proved to be formed in CrCoNi MEA. Interstitial diffusion and vacancy jump kinetic Monte Carlo (kMC) simulations are performed to investigate the impact of chemical ordering structures on defect diffusion in CrCoNi MEA. Diffusion results show that the formation of chemical ordering structures could reduce interstitial and vacancy diffusion trajectories and mean squared displacement (MSD), which will lead to the sluggish diffusion phenomenon. The mesh region division was used to investigate the correlation between interstitial or vacancy diffusion region and the distribution of chemical ordering structures. Our results show that chemical ordering structures could limit interstitial and vacancy diffusion region and lead to sluggish diffusion, which may delay the evolution of defect and promotes the recombination of interstitial and vacancy defects, thereby improving the radiation resistance.

5.2 Outlook of future research

This dissertation presents a variety of simulation methods to investigate the response of H/MEAs to radiation damage and the motion of radiation defects, which is expected to provide theoretical guidance for the design of next-generation nuclear materials. However, further validation of the simulation results with experimental results is desired in the further. In addition, the defects produced by irradiation damage are complex and only the motion of interstitial and vacancy simple point defects in H/MEAs are investigated in this dissertation. The generation of some high-dimensional defects and their effect on the properties of H/MEAs need to be further investigated, such as the movement of dislocations and the possibility of phase transitions occurring during radiation damage. Finally, due to the limitations of computational performance, the model size and simulation time are still limited to a small range of scales. It remains

a challenge to study higher levels of radiation damage in large models and over longer time scale. In the further, it is expected that new simulation method will be developed to address these issues and provides more accurate and effective simulation results.

Appendix A

Verification of quality of potential in Ni-Mn alloys:

In order to verify the quality of potential, we performed an additional MD–MC annealing simulation works for Ni-Mn alloys. **Fig. A.1** showed the results in Ni-Mn alloy after annealing simulation at T= 600 K, and it is obvious that our potential could successfully predict the $L1_0$ order structure of Ni-Mn alloy.

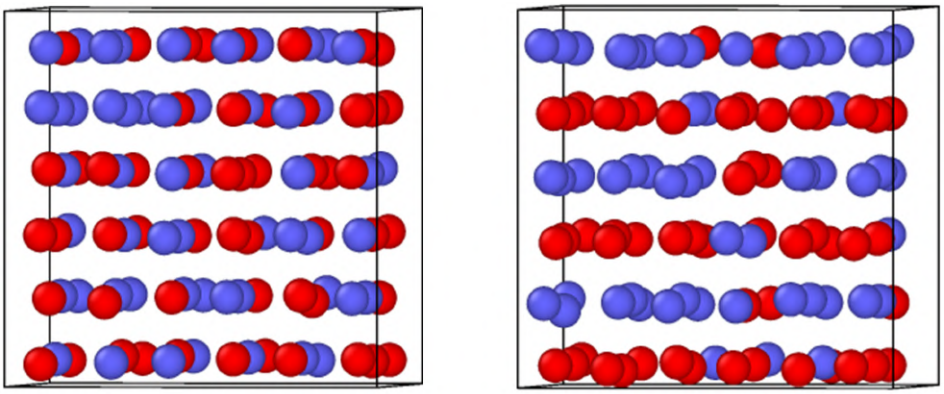

(a) Random Ni-Mn **(b) $L1_0$ Ni-Mn**

Figure A.1: Ni-Mn alloy structure after MD–MC annealing, (a) random Ni-Mn and (b) $L1_0$ Ni-Mn. A $3 \times 3 \times 3$ supercell contains 108 atoms was used to perform the annealing simulation at $T = 600K$, with an average of 10 swaps per atom.

Interstitial dumbbell migration barrier by DFT:

Nudged elastic band method ([The Journal of chemical physics 113.22 (2000): 9901-9904.], [The Journal of chemical physics 113.22 (2000): 9978-9985.]) was used to identify the interstitial dumbbells migration paths and migration energy barrier. The energy and force convergence criterion were set as 10^{-6} eV and 10^{-2} eV/Å respectively ([Physical Review Materials 2.1 (2018): 013602.]). The interstitial dumbbells migration paths were shown in **Fig. A.2**. Interstitial dumbbell migration barriers in equal-atomic model and Cr-rich model were calculated as 0.76 eV and 0.44 eV, respectively. Higher Cr concentration leads to lower interstitial dumbbell migration barrier, which will cause faster migration of interstitial in Cr-rich regions.

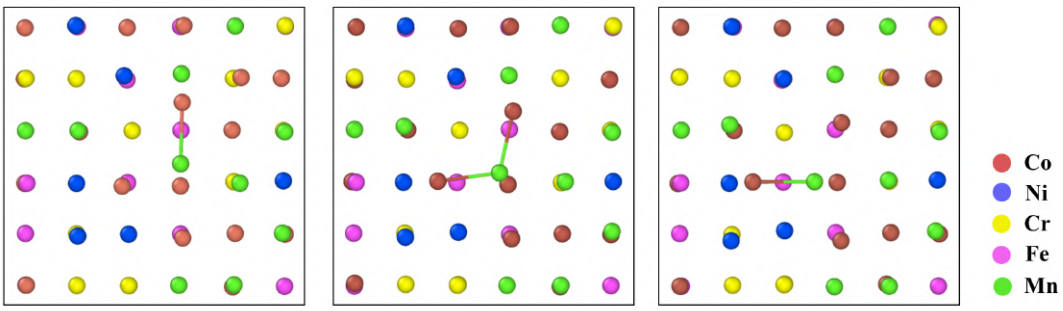

(a) Initial state (b) Transition state (c) Final state

Figure A.2: Migration process of interstitial dumbbell. (a) Initial state, (b) transition state, (c)final state. A $3 \times 3 \times 3$ supercell contains 108 atoms was used to perform the migration barrier calculation, the energy cutoff was set to be 350 eV, and $4 \times 4 \times 4$ k-points mesh was used.

CSRO relaxation and destroying timescale:

The relaxation of the CSRO consists of thermally activated events, such as atoms diffusion by vacancy and interstitial. However, the relaxation of the CSRO, in other words, changing the chemical ordering, requires vast number of atoms jumps, and thus even at $T = 1100$ K it takes much longer time than the time for generating damage (destroying CSRO) by the bombardment. Actually, Zhang et al. aged the CrCoNi MEA for 120 hours followed by furnace cooling, and then observed the formation of SRO ([Nature 581.7808 (2020): 283-287]). The experiments results showed that the relaxation of CSRO during annealing in HEA/MEA is a slow process. As for the radiation bombardment effect, the whole radiation process is very rapid, and the radiation bombardment could quickly destroy the CSRO. **Fig. A.3 (a)** showed the PKA process in CoNiCrFeMn HEA with the energy of 5000 eV, the number of defects reached the peak at around 0.3 ps, and all the atoms in radiation region were immediately melted due to the high-energy particle bombardment. After about 10 ps, all the atoms in radiation region will rearrange through cooling and recrystallization. Additionally, our previous work had studied the time scale of CSRO formation through vacancy jumps [Computational Materials Science 198 (2021): 110670.], according to the TTC (time-temperature-CSRO) curve, the formation of certain degree of CSRO at 700 K (the

irradiation temperature) should require 10^3–10^4 atoms jump with the vacancy concentration of 10^{-3}. Here, we also roughly estimated the time scale of CSRO formation through interstitial jumps. **Fig. A.3 (b)** showed the activation energy $\Delta G(T)$ distribution of interstitial jumps through the dumbbell model, the time of jump i is predicted as $t_i = t_0 \exp\left[\frac{-\Delta G(T)}{k_B T}\right]$, where k_B is the Boltzmann constant, and $t_0 = 1 \times 10^{-13}$s. Therefore, the average time of each interstitial jump can be estimated as $\bar{t} = \sum_i^N t_i/N \approx 3.7 \times 10^{-9}$s. Consider the interstitial concentration (0.4%) during irradiation, we can simply estimate the time required to form a certain degree of CSRO by interstitial jumps should be around 10^{-6}∼10^{-5}s. Hence the time scales of relaxing and destroying CSRO by radiation bombardment is totally different with the order of 10^3∼10^4 times or more, in other words, there is almost no nonlinear time-scale interaction between these phenomena and thus we can consider separately.

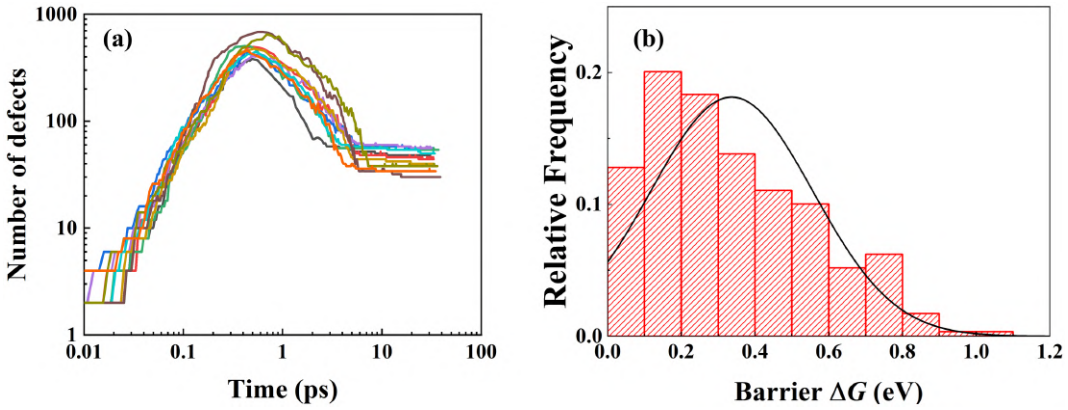

Figure A.3: (a) Number of defects during PKA simulations with 3000 eV energy in CoNiCrFeMn HEA, and (b) activation barriers of interstitial jumps through dumbbell model.

Appendix B

Chemical ordering degree change during interstitial diffusion simulation:

In order to ensure that there was no significant change in chemical ordering during the interstitial diffusion simulation, we checked the Warren-Cowley parameter during simulation. **Fig. B.1** shows the chemical ordering parameters of all the element pairs. It is clear that only small fluctuations in the chemical ordering values occurred, and therefore it is believed that there will be no chemical ordering changes will have an impact on the diffusion results.

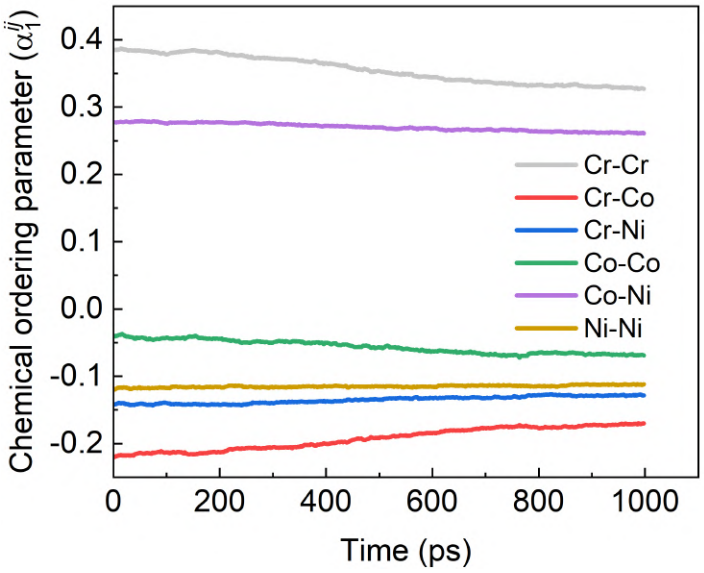

Figure B.1: Chemical ordering parameters change during interstitial diffusion.

Vacancy jump time in the order and random models:

For the kMC vacancy jump simulation, the time required for each vacancy jump in the chemical ordering model and random model are different. **Fig. B.2 (a), (b)** shows the distribution of time for vacancy jump once in the Model 5 and random models. In the Model 5 model (with chemical ordering structures), the time distribution is significantly wider and the average time for a vacancy jump once is much longer than in the random model. Therefore, vacancy diffusivity in Model 5 is slower than in the

random model.

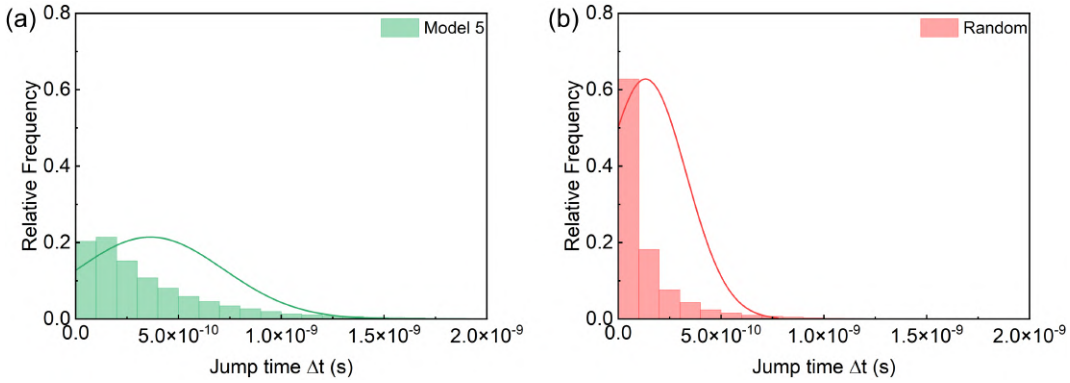

Figure B.2: Distribution of the time for vacancy jump once in the (a) Model 5 and (b) random model.

Interstitial and vacancy formation energy in Model 5 and random model:

Interstitial and vacancy formation energy were calculated and shown in **Fig. B.3 (a), (b)**. In Model 5 (with chemical ordering), the average interstitial and vacancy formation energies are both higher than in the random model. Thus, the formation of chemical ordering structures can restrict interstitial and vacancy diffusion.

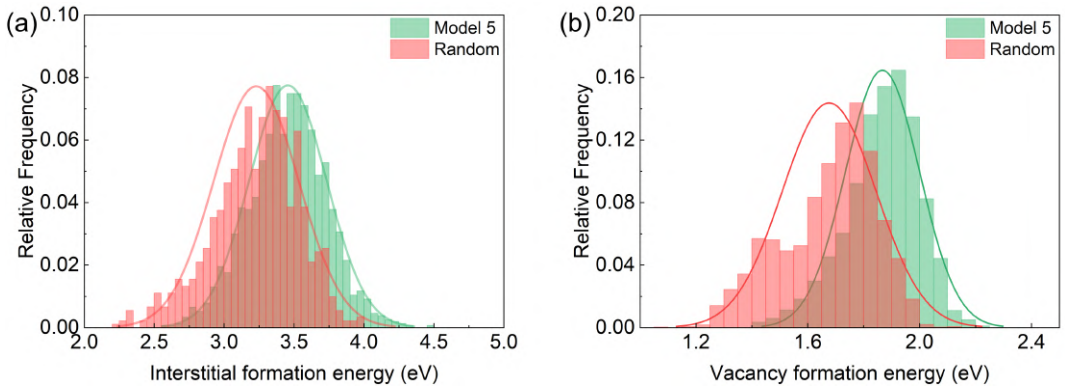

Figure B.3: Distribution of (a) interstitial and (b) vacancy formation energy in Sample 5 and (b) random model.

Chemical ordering degree, interstitial and vacancy residence density, and interstitial and vacancy formation energy in the random model:

For comparison, 50 independent interstitial and vacancy diffusion simulations were performed in the random model. **Fig. B.4 (a), (b)** show one slice of the chemical ordering degree $\overline{P_k^{\mathrm{I_d}}}$ of type I and other structures contour maps, respectively. Almost all atoms are presented as other structures, showing a random distribution. **Fig. B.4 (c), (d)** show one slice of the interstitial and vacancy residence density Q_k contour maps, respectively. The distribution of interstitial and vacancy diffusion regions also showing random, with no clear preference diffusion regions. The average correlation factors $\overline{G^{\mathrm{I_d}}}$ of interstitial (vacancy) for diffusion in type I and other structures were calculated as 0.01 (0.01) and 0.95 (0.94), respectively. **Fig. B.4 (e), (f)** show interstitial and vacancy formation energy contour maps, respectively. Compared with Model 5, the formation energy magnitudes are more evenly distributed, without significant difference. Therefore, the diffusion regions of interstitial and vacancy are also more uniformly distributed.

Chemical ordering degree distribution and interstitial and vacancy residence density in other models with the similar chemical degree to Model 5:

In order to avoid the model size effect, 3 different initial structure models are used to performed the annealing simulation and interstitial and vacancy diffusion simulation. **Fig. B.5** show the results of remaining two models (labeled as Model 5-2 and Model 5-3, respectively) with similar chemical ordering degree to Model 5. One slice of chemical ordering degree of type I and other structures, and interstitial and vacancy diffusion residence density maps are shown, respectively. The average correlation factors $\overline{G^{\mathrm{I_d}}}$ between type I and other and interstitial (vacancy) were calculated as 0.33 (0.24) and 0.48 (0.60) in Model 5-2, 0.42 (0.32) and 0.48 (0.62) in Model 5-3, respectively. Therefore, the results also show that defects prefer to diffuse in regions without chemical ordering structures, in other words, the formation of chemical ordering structures could restrict defect diffusion regions.

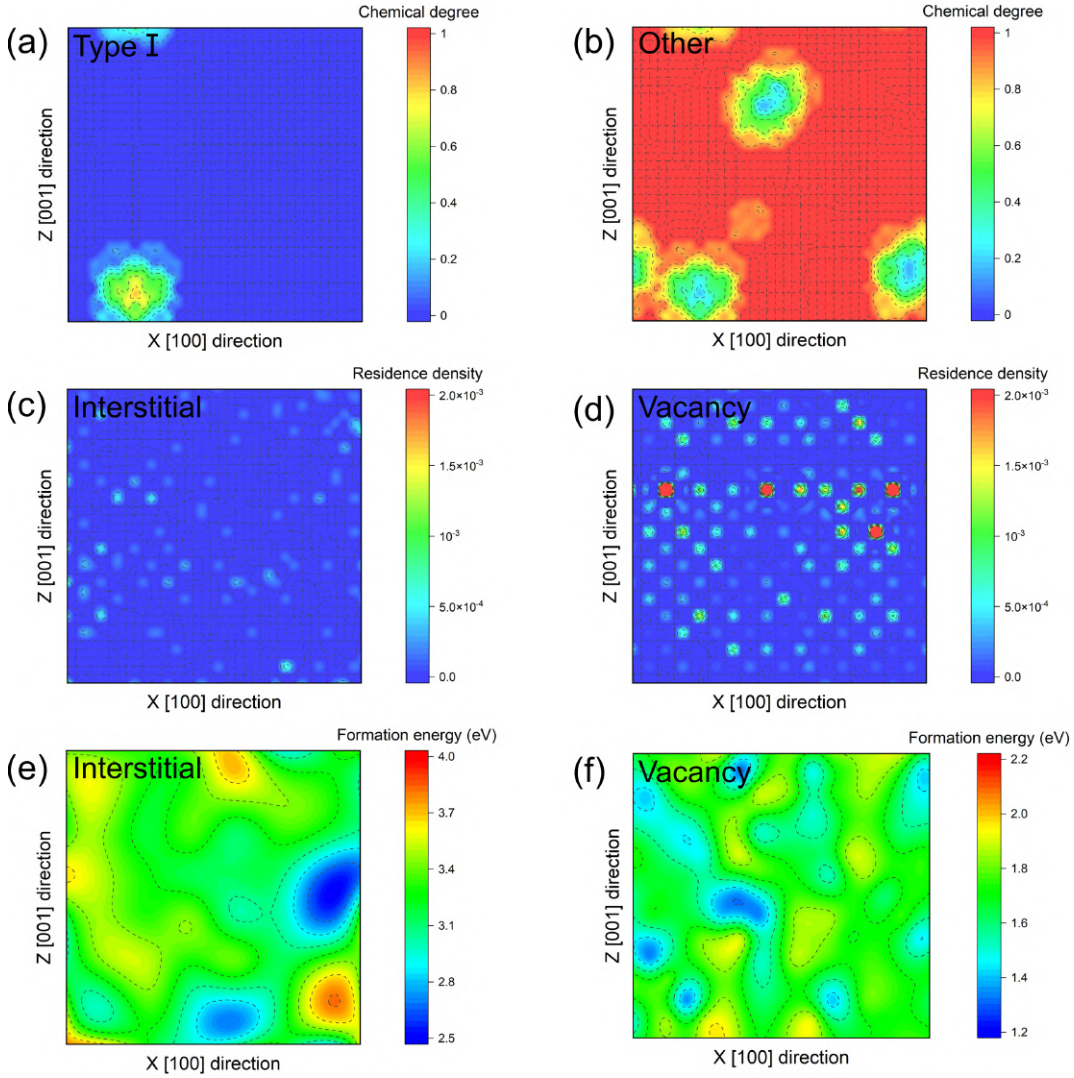

Figure B.4: (a) - (b) Slice of chemical degree distribution contours of chemical ordering type I and other structures in the random model, respectively. (c) - (d) Slice of interstitial and vacancy residence density contours in the random model, respectively. The correlation factor between chemical ordering degree of type I and other and interstitial (vacancy) residence density was calculated as 0.01 (0.01) and 0.95 (0.94), respectively. (e) - (f) Slice of interstitial and vacancy formation energy contours in the random model, respectively.

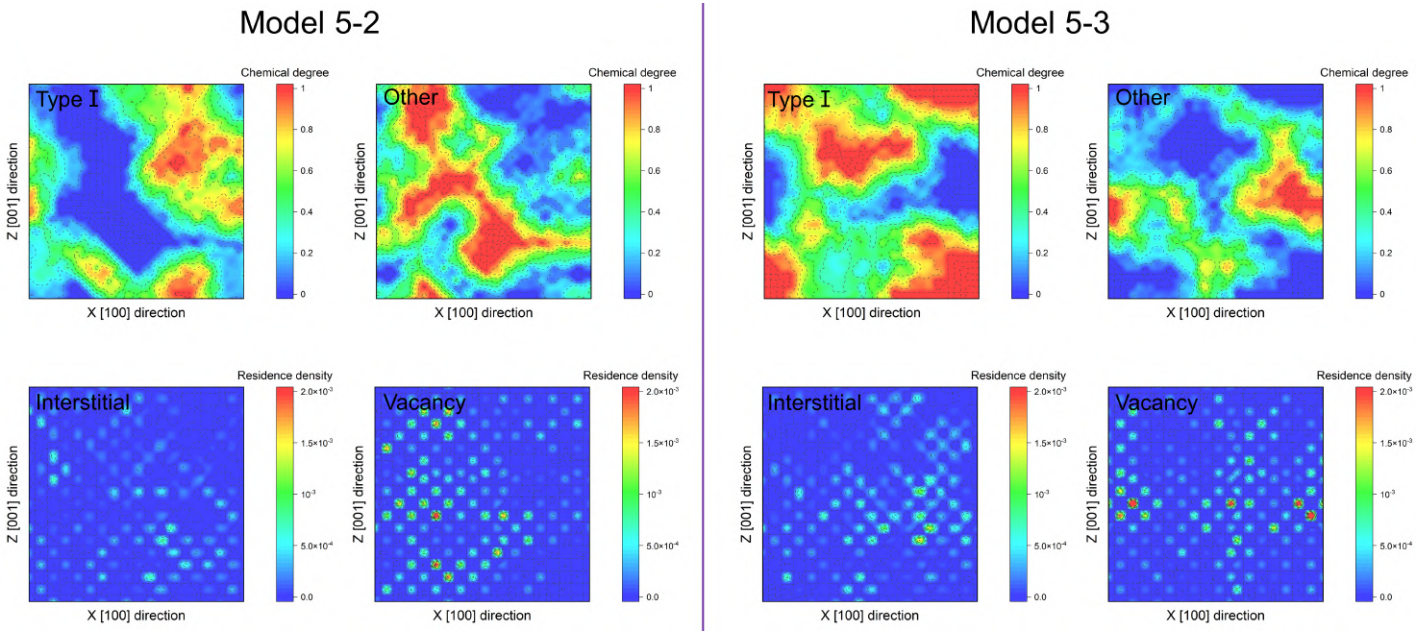

Figure B.5: Slice of chemical degree distribution contours of chemical ordering type I and other structures, and slice of interstitial and vacancy residence density contours in the Model 5-2 and Model 5-3, respectively. The correlation factor between chemical ordering degree of type I and other and interstitial (vacancy) residence density was calculated as 0.33 (0.24) and 0.48 (0.60) in Model 5-2, 0.42 (0.32) and 0.48 (0.62) in Model 5-3, respectively.

Chemical ordering degree distribution and interstitial and vacancy residence density in the Model 3 (lower chemical ordering degree):

In order to confirm that chemical ordering structure restrict defect diffusion regions not due to the specific chemical ordering degree, 3 different initial structure models (labeled as Model 3-1, Model 3-2, and Model 3-3) with less annealing time (Model 3 with lower chemical ordering degree) are used to perform the same interstitial and vacancy diffusion simulations. **Fig. B.6** one slice of the chemical ordering degree distribution of type I and other structures, and interstitial and vacancy residence density, respectively. Due to the reduction of the chemical ordering structures, a less restrictive effect on defect diffusion can be expected, and direct comparison of the results may not be able to get the correlation between diffusion region and the chemical ordering degree. Therefore, the average correlation factors for defects diffusion in different structures are calculated, and the correlation factor $\overline{G^{\mathrm{I_d}}}$ between type I and other and interstitial (vacancy) were calculated as 0.20 (0.18) and 0.67 (0.70) in Model 3-1, 0.25 (0.23) and 0.60 (0.66) in Model 3-2, 0.27 (0.27) and 0.60 (0.62) in Model 3-3, respectively. The results still support that chemical ordering structures could restrict defect diffusion regions.

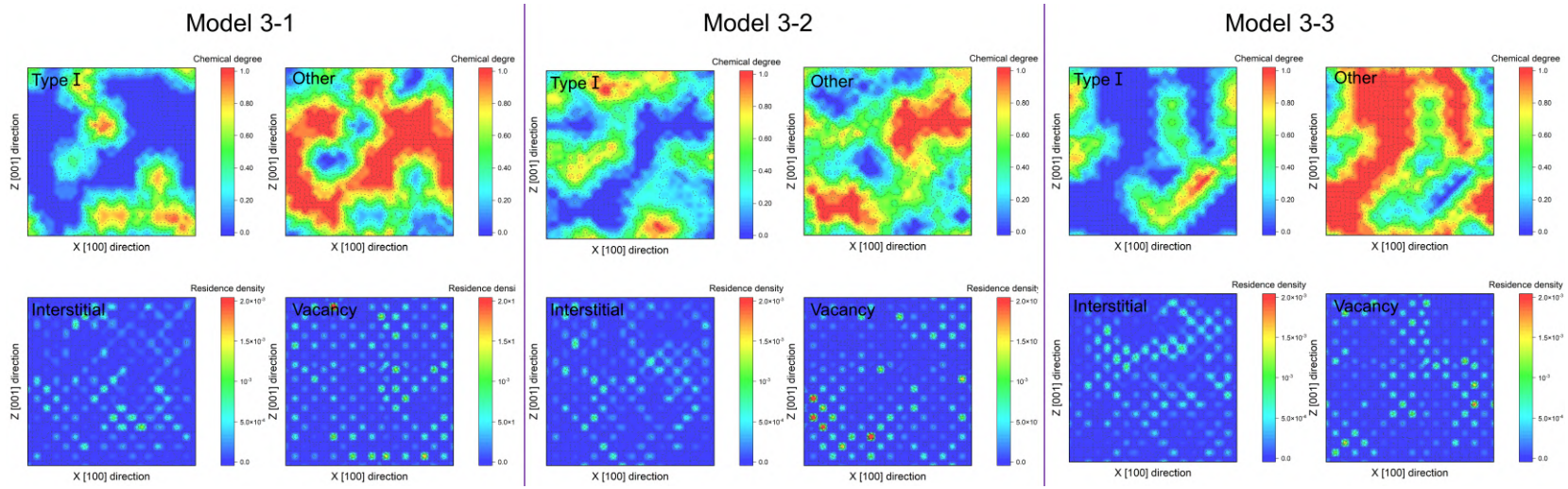

Figure B.6: Slice of chemical degree distribution contours of chemical ordering type I and other structures, and slice of interstitial and vacancy residence density contours in the Model 3-1, Model 3-2, Model 3-3, respectively. The correlation factor between chemical ordering degree of type I and other and interstitial (vacancy) residence density was calculated as 0.20 (0.18) and 0.67 (0.70) in Model 3-1, 0.25 (0.23) and 0.60 (0.66) in Model 3-2, 0.27 (0.27) and 0.60 (0.62) in Model 3-3, respectively.

Root mean squared error (RMSE) of defect residence density:

In order to capture the characteristics of defect diffusion in different region of models, a sufficient number of diffusion simulations is necessary. To conform that 50 defect diffusion simulations with different initial defect positions are enough to illustrate defect diffusion characteristics, we also checked the convergence of the root mean squared error (RMSE) of the defect diffusion density with the number of simulations by:

$$RMSE = \sqrt{\frac{\sum_{k=1}^{N} |Q_k - Q|^2}{N}} \tag{1}$$

where N is the total number of small mesh region, Q_k is the defect residence time in mesh k, and Q is the real defect residence time in each mesh. As shown in **Fig. B.7**, 50 times of simulations have been converged and are able to accurately reflect defect characteristics.

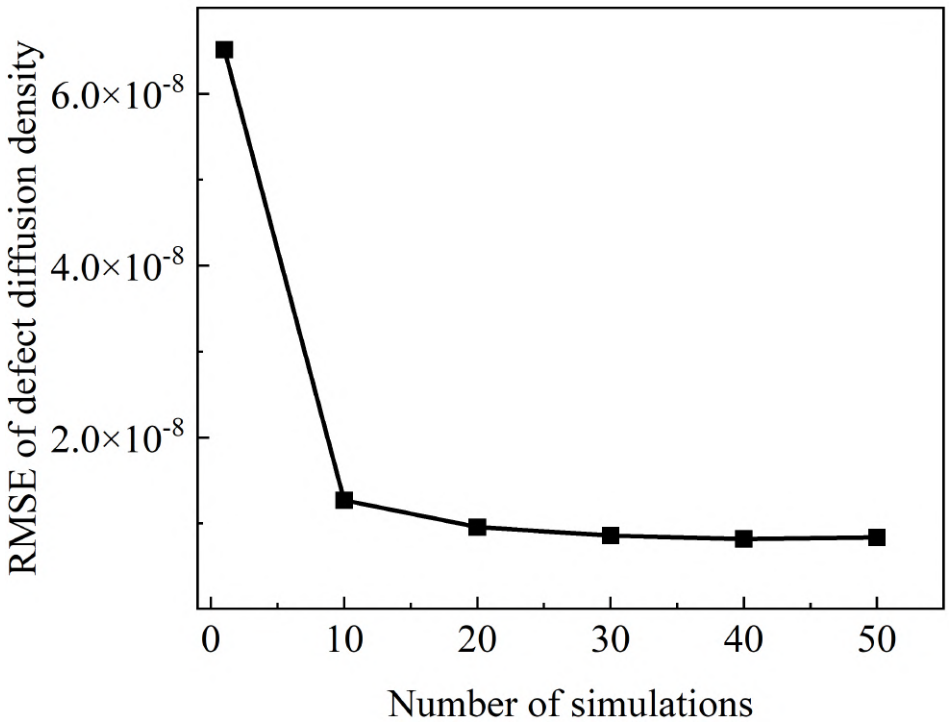

Figure B.7: Root mean squared error (RMSE) of the defect diffusion density with the number of simulations.

Bibliography

[1] Brain Cantor, ITH Chang, Peter Knight, and AJB Vincent. Microstructural development in equiatomic multicomponent alloys. *Materials Science and Engineering: A*, 375:213–218, 2004.

[2] J-W Yeh, S-K Chen, S-J Lin, J-Y Gan, T-S Chin, T-T Shun, C-H Tsau, and S-Y Chang. Nanostructured high-entropy alloys with multiple principal elements: novel alloy design concepts and outcomes. *Advanced engineering materials*, 6(5):299–303, 2004.

[3] Yong Zhang, Ting Ting Zuo, Zhi Tang, Michael C Gao, Karin A Dahmen, Peter K Liaw, and Zhao Ping Lu. Microstructures and properties of high-entropy alloys. *Progress in materials science*, 61:1–93, 2014.

[4] Daniel B Miracle and Oleg N Senkov. A critical review of high entropy alloys and related concepts. *Acta Materialia*, 122:448–511, 2017.

[5] Easo P George, Dierk Raabe, and Robert O Ritchie. High-entropy alloys. *Nature reviews materials*, 4(8):515–534, 2019.

[6] G Laplanche, A Kostka, C Reinhart, J Hunfeld, G Eggeler, and EP George. Reasons for the superior mechanical properties of medium-entropy CrCoNi compared to high-entropy CrMnFeCoNi. *Acta Materialia*, 128:292–303, 2017.

[7] YH Jo, S Jung, WM Choi, SS Sohn, HS Kim, BJ Lee, Nack J Kim, and S Lee. Cryogenic strength improvement by utilizing room-temperature deformation twinning in a partially recrystallized VCrMnFeCoNi high-entropy alloy. *Nature communications*, 8(1):15719, 2017.

[8] Ming-Hung Tsai. Physical properties of high entropy alloys. *Entropy*, 15(12):5338–5345, 2013.

[9] Zhiming Li, Konda Gokuldoss Pradeep, Yun Deng, Dierk Raabe, and Cemal Cem Tasan. Metastable high-entropy dual-phase alloys overcome the strength–ductility trade-off. *Nature*, 534(7606):227–230, 2016.

[10] Frederik Otto, A Dlouhỳ, Ch Somsen, Hongbin Bei, G Eggeler, and Easo P George. The influences of temperature and microstructure on the tensile properties of a CoCrFeMnNi high-entropy alloy. *Acta Materialia*, 61(15):5743–5755, 2013.

[11] Zezhou Li, Shiteng Zhao, Robert O Ritchie, and Marc A Meyers. Mechanical properties of high-entropy alloys with emphasis on face-centered cubic alloys. *Progress in Materials Science*, 102:296–345, 2019.

[12] CE Slone, Jiashi Miao, Easo P George, and Michael J Mills. Achieving ultra-high strength and ductility in equiatomic CrCoNi with partially recrystallized microstructures. *Acta Materialia*, 165:496–507, 2019.

[13] Weidong Li, Di Xie, Dongyue Li, Yong Zhang, Yanfei Gao, and Peter K Liaw. Mechanical behavior of high-entropy alloys. *Progress in Materials Science*, 118:100777, 2021.

[14] Mo-Rigen He, Shuai Wang, Shi Shi, Ke Jin, Hongbin Bei, Kazuhiro Yasuda, Syo Matsumura, Kenji Higashida, and Ian M Robertson. Mechanisms of radiation-

induced segregation in CrFeCoNi-based single-phase concentrated solid solution alloys. *Acta Materialia*, 126:182–193, 2017.

[15] Tengfei Yang, Songqin Xia, Shi Liu, Chenxu Wang, Shaoshuai Liu, Yuan Fang, Yong Zhang, Jianming Xue, Sha Yan, and Yugang Wang. Precipitation behavior of AlxCoCrFeNi high entropy alloys under ion irradiation. *Scientific reports*, 6(1):1–8, 2016.

[16] Hyeon-Seok Do and Byeong-Joo Lee. Origin of radiation resistance in multi-principal element alloys. *Scientific reports*, 8(1):1–9, 2018.

[17] Chenyang Lu, Taini Yang, Ke Jin, Ning Gao, Pengyuan Xiu, Yanwen Zhang, Fei Gao, Hongbin Bei, William J Weber, Kai Sun, et al. Radiation-induced segregation on defect clusters in single-phase concentrated solid-solution alloys. *Acta Materialia*, 127:98–107, 2017.

[18] YEH Jien-Wei. Recent progress in high entropy alloys. *Ann. Chim. Sci. Mat*, 31(6):633–648, 2006.

[19] Jien-Wei Yeh. Alloy design strategies and future trends in high-entropy alloys. *Jom*, 65:1759–1771, 2013.

[20] Ming-Hung Tsai and Jien-Wei Yeh. High-entropy alloys: a critical review. *Materials Research Letters*, 2(3):107–123, 2014.

[21] Oleg N Senkov, GB Wilks, JM Scott, and Daniel B Miracle. Mechanical properties of Nb25Mo25Ta25W25 and V20Nb20Mo20Ta20W20 refractory high entropy alloys. *Intermetallics*, 19(5):698–706, 2011.

[22] Yu Zou, Huan Ma, and Ralph Spolenak. Ultrastrong ductile and stable high-entropy alloys at small scales. *Nature communications*, 6(1):7748, 2015.

[23] Yong Zhang, Yun Jun Zhou, Jun Pin Lin, Guo Liang Chen, and Peter K Liaw. Solid-solution phase formation rules for multi-component alloys. *Advanced engineering materials*, 10(6):534–538, 2008.

[24] Hsuan-Ping Chou, Yee-Shyi Chang, Swe-Kai Chen, and Jien-Wei Yeh. Microstructure, thermophysical and electrical properties in AlxCoCrFeNi (0 x 2) high-entropy alloys. *Materials Science and Engineering: B*, 163(3):184–189, 2009.

[25] David A Porter, Kenneth E Easterling, and Mohamed Y Sherif. *Phase transformations in metals and alloys*. CRC press, 2021.

[26] K-Y Tsai, M-H Tsai, and J-W Yeh. Sluggish diffusion in co–cr–fe–mn–ni high-entropy alloys. *Acta Materialia*, 61(13):4887–4897, 2013.

[27] Juliusz Dąbrowa, Marek Zajusz, Witold Kucza, Grzegorz Cieślak, Katarzyna Berent, Tomasz Czeppe, Tadeusz Kulik, and Marek Danielewski. Demystifying the sluggish diffusion effect in high entropy alloys. *Journal of Alloys and Compounds*, 783:193–207, 2019.

[28] Mayur Vaidya, Simon Trubel, BS Murty, Gerhard Wilde, and Sergiy V Divinski. Ni tracer diffusion in CoCrFeNi and CoCrFeMnNi high entropy alloys. *Journal of Alloys and Compounds*, 688:994–1001, 2016.

[29] Pierre Hohenberg and Walter Kohn. Inhomogeneous electron gas. *Physical review*, 136(3B):B864, 1964.

[30] Walter Kohn and Lu Jeu Sham. Self-consistent equations including exchange and correlation effects. *Physical review*, 140(4A):A1133, 1965.

[31] David M Ceperley and Berni J Alder. Ground state of the electron gas by a stochastic method. *Physical review letters*, 45(7):566, 1980.

[32] Nicholas Metropolis and Stanislaw Ulam. The monte carlo method. *Journal of the American statistical association*, 44(247):335–341, 1949.

[33] Jörg Behler and Michele Parrinello. Generalized neural-network representation of high-dimensional potential-energy surfaces. *Physical review letters*, 98(14):146401, 2007.

[34] Jun-Ping Du, Peijun Yu, Shuhei Shinzato, Fan-Shun Meng, Yuji Sato, Yangen Li, Yiwen Fan, and Shigenobu Ogata. Chemical domain structure and its formation kinetics in crconi medium-entropy alloy. *Acta Materialia*, 240:118314, 2022.

[35] Robert J Budnitz. Nuclear power: Status report and future prospects. *Energy Policy*, 96:735–739, 2016.

[36] Steven J Zinkle and Lance Lewis Snead. Designing radiation resistance in materials for fusion energy. *Annual Review of Materials Research*, 44:241–267, 2014.

[37] Louis J Santodonato, Yang Zhang, Mikhail Feygenson, Chad M Parish, Michael C Gao, Richard JK Weber, Joerg C Neuefeind, Zhi Tang, and Peter K Liaw. Deviation from high-entropy configurations in the atomic distributions of a multi-principal-element alloy. *Nature communications*, 6(1):5964, 2015.

[38] Ke Jin, Brian C Sales, George Malcolm Stocks, German D Samolyuk, Markus Daene, William J Weber, Yanwen Zhang, and Hongbin Bei. Tailoring the physical properties of Ni-based single-phase equiatomic alloys by modifying the chemical complexity. *Scientific reports*, 6(1):20159, 2016.

[39] GUO Sheng and Chain Tsuan Liu. Phase stability in high entropy alloys: Formation of solid-solution phase or amorphous phase. *Progress in Natural Science: Materials International*, 21(6):433–446, 2011.

[40] Chenyang Lu, Liangliang Niu, Nanjun Chen, Ke Jin, Taini Yang, Pengyuan Xiu, Yanwen Zhang, Fei Gao, Hongbin Bei, Shi Shi, et al. Enhancing radiation tolerance by controlling defect mobility and migration pathways in multicomponent single-phase alloys. *Nature communications*, 7(1):13564, 2016.

[41] Fredric Granberg, K Nordlund, Mohammad W Ullah, Ke Jin, Chenyang Lu, Hongbin Bei, LM Wang, F Djurabekova, WJ Weber, and Y Zhang. Mechanism of radiation damage reduction in equiatomic multicomponent single phase alloys. *Physical review letters*, 116(13):135504, 2016.

[42] Kang Xiang, Liang-Yu Chen, Linjiang Chai, Ning Guo, and Hao Wang. Microstructural characteristics and properties of CoCrFeNiNbx high-entropy alloy coatings on pure titanium substrate by pulsed laser cladding. *Applied Surface Science*, 517:146214, 2020.

[43] Binglun Yin, Francesco Maresca, and WA Curtin. Vanadium is an optimal element for strengthening in both fcc and bcc high-entropy alloys. *Acta Materialia*, 188:486–491, 2020.

[44] Qingqing Ding, Yin Zhang, Xiao Chen, Xiaoqian Fu, Dengke Chen, Sijing Chen, Lin Gu, Fei Wei, Hongbin Bei, Yanfei Gao, et al. Tuning element distribution, structure and properties by composition in high-entropy alloys. *Nature*, 574(7777):223–227, 2019.

[45] Zhifeng Lei, Xiongjun Liu, Yuan Wu, Hui Wang, Suihe Jiang, Shudao Wang, Xidong Hui, Yidong Wu, Baptiste Gault, Paraskevas Kontis, et al. Enhanced strength and ductility in a high-entropy alloy via ordered oxygen complexes. *Nature*, 563(7732):546–550, 2018.

[46] E Antillon, C Woodward, SI Rao, B Akdim, and TA Parthasarathy. Chemical short range order strengthening in a model FCC high entropy alloy. *Acta Materialia*, 190:29–42, 2020.

[47] Zhenggang Wu, Hongbin Bei, George M Pharr, and Easo P George. Temperature dependence of the mechanical properties of equiatomic solid solution alloys with face-centered cubic crystal structures. *Acta Materialia*, 81:428–441, 2014.

[48] Osman El-Atwani, Nan Li, Meimei Li, Arun Devaraj, JKS Baldwin, Matthew M Schneider, Damian Sobieraj, Jan S Wróbel, Duc Nguyen-Manh, Stuart A Maloy, et al. Outstanding radiation resistance of tungsten-based high-entropy alloys. *Science advances*, 5(3):eaav2002, 2019.

[49] Yangen Li, Rui Li, Qing Peng, and Shigenobu Ogata. Reduction of dislocation, mean free path, and migration barriers using high entropy alloy: Insights from the atomistic study of irradiation damage of CoNiCrFeMn. *Nanotechnology*, 31(42):425701, 2020.

[50] E Levo, F Granberg, C Fridlund, K Nordlund, and F Djurabekova. Radiation damage buildup and dislocation evolution in Ni and equiatomic multicomponent Ni-based alloys. *Journal of Nuclear Materials*, 490:323–332, 2017.

[51] Juliusz Dąbrowa and Marek Danielewski. State-of-the-art diffusion studies in the high entropy alloys. *Metals*, 10(3):347, 2020.

[52] Ed J Pickering, Alexander W Carruthers, Paul J Barron, Simon C Middleburgh, David EJ Armstrong, and Amy S Gandy. High-entropy alloys for advanced nuclear applications. *Entropy*, 23(1):98, 2021.

[53] Da Chen, Y Tong, H Li, J Wang, YL Zhao, Alice Hu, and JJ Kai. Helium accumulation and bubble formation in FeCoNiCr alloy under high fluence He+ implantation. *Journal of Nuclear Materials*, 501:208–216, 2018.

[54] Feida Chen, Xiaobin Tang, Yahui Yang, Hai Huang, Jian Liu, Huan Li, and Da Chen. Atomic simulations of Fe/Ni multilayer nanocomposites on the radiation damage resistance. *Journal of nuclear materials*, 468:164–170, 2016.

[55] I Chant and KL Murty. Structural materials issues for the next generation fission reactors. *Jom*, 62:67–74, 2010.

[56] Kai Nordlund, Mai Ghaly, RS Averback, María Caturla, T Diaz de La Rubia, and Jura Tarus. Defect production in collision cascades in elemental semiconductors and fcc metals. *Physical Review B*, 57(13):7556, 1998.

[57] Qing Peng, Fanjiang Meng, Yizhong Yang, Chenyang Lu, Huiqiu Deng, Lumin Wang, Suvranu De, and Fei Gao. Shockwave generates< 100> dislocation loops in bcc iron. *Nature communications*, 9(1):4880, 2018.

[58] Mohammad W Ullah, Haizhou Xue, Gihan Velisa, Ke Jin, Hongbin Bei, William J Weber, and Yanwen Zhang. Effects of chemical alternation on damage accumulation in concentrated solid-solution alloys. *Scientific reports*, 7(1):4146, 2017.

[59] Shijun Zhao, Gihan Velisa, Haizhou Xue, Hongbin Bei, William J Weber, and Yanwen Zhang. Suppression of vacancy cluster growth in concentrated solid solution alloys. *Acta Materialia*, 125:231–237, 2017.

[60] Yangen Li, Rui Li, and Qing Peng. Enhanced surface bombardment resistance of the conicrfemn high entropy alloy under extreme irradiation flux. *Nanotechnology*, 31(2):025703, 2019.

[61] Won-Mi Choi, Yong Hee Jo, Seok Su Sohn, Sunghak Lee, and Byeong-Joo Lee. Understanding the physical metallurgy of the CoCrFeMnNi high-entropy alloy: an atomistic simulation study. *Npj Computational Materials*, 4(1):1, 2018.

[62] Steve Plimpton. Fast parallel algorithms for short-range molecular dynamics. *Journal of computational physics*, 117(1):1–19, 1995.

[63] Herman JC Berendsen, JPM van Postma, Wilfred F Van Gunsteren, ARHJ DiNola, and Jan R Haak. Molecular dynamics with coupling to an external bath. *The Journal of chemical physics*, 81(8):3684–3690, 1984.

[64] Alexander Stukowski. Visualization and analysis of atomistic simulation data with OVITO–the Open Visualization Tool. *Modelling and simulation in materials science and engineering*, 18(1):015012, 2009.

[65] N Stefanou, H Akai, and R Zeller. An efficient numerical method to calculate shape truncation functions for Wigner-Seitz atomic polyhedra. *Computer physics communications*, 60(2):231–238, 1990.

[66] J Dana Honeycutt and Hans C Andersen. Molecular dynamics study of melting and freezing of small Lennard-Jones clusters. *Journal of Physical Chemistry*, 91(19):4950–4963, 1987.

[67] Antonio Fernández-Caballero, Mark Fedorov, Jan S Wróbel, Paul M Mummery, and Duc Nguyen-Manh. Configurational entropy in multicomponent alloys: Matrix formulation from ab initio based hamiltonian and application to the FCC Cr-Fe-Mn-Ni system. *Entropy*, 21(1):68, 2019.

[68] Yannick Guérin, Gary S Was, and Steven J Zinkle. Materials challenges for advanced nuclear energy systems. *Mrs Bulletin*, 34(1):10–19, 2009.

[69] Alexander Stukowski, Vasily V Bulatov, and Athanasios Arsenlis. Automated identification and indexing of dislocations in crystal interfaces. *Modelling and Simulation in Materials Science and Engineering*, 20(8):085007, 2012.

[70] R Schäublin*, Z Yao, N Baluc, and M Victoria. Irradiation-induced stacking fault tetrahedra in fcc metals. *Philosophical magazine*, 85(4-7):769–777, 2005.

[71] Zhipeng Wang, Qihong Fang, Jia Li, Bin Liu, and Yong Liu. Effect of lattice distortion on solid solution strengthening of BCC high-entropy alloys. *Journal of Materials Science & Technology*, 34(2):349–354, 2018.

[72] Kazuto Arakawa, K Ono, Mi Isshiki, K Mimura, M Uchikoshi, and H Mori. Observation of the one-dimensional diffusion of nanometer-sized dislocation loops. *Science*, 318(5852):956–959, 2007.

[73] Yoshitaka Matsukawa and Steven J Zinkle. One-dimensional fast migration of vacancy clusters in metals. *Science*, 318(5852):959–962, 2007.

[74] BN Singh and AJE Foreman. Production bias and void swelling in the transient regime under cascade damage conditions. *Philosophical Magazine A*, 66(6):975–990, 1992.

[75] Yu N Osetsky, DJ Bacon, A Serra, BN Singh, and SI Golubov. Stability and mobility of defect clusters and dislocation loops in metals. *Journal of nuclear materials*, 276(1-3):65–77, 2000.

[76] Chenyang Lu, Taini Yang, Liangliang Niu, Qing Peng, Ke Jin, Miguel L Crespillo, Gihan Velisa, Haizhou Xue, Feifei Zhang, Pengyuan Xiu, et al. Interstitial migration behavior and defect evolution in ion irradiated pure nickel and Ni-xFe binary alloys. *Journal of Nuclear Materials*, 509:237–244, 2018.

[77] BN Singh, SI Golubov, H Trinkaus, A Serra, Yu N Osetsky, and AV Barashev. Aspects of microstructure evolution under cascade damage conditions. *Journal of nuclear materials*, 251:107–122, 1997.

[78] H Trinkaus, BN Singh, and AJE Foreman. Impact of glissile interstitial loop production in cascades on defect accumulation in the transient. *Journal of nuclear materials*, 206(2-3):200–211, 1993.

[79] Graeme Henkelman, Blas P Uberuaga, and Hannes Jónsson. A climbing image nudged elastic band method for finding saddle points and minimum energy paths. *The Journal of chemical physics*, 113(22):9901–9904, 2000.

[80] Emile Maras, Oleg Trushin, Alexander Stukowski, Tapio Ala-Nissila, and Hannes Jonsson. Global transition path search for dislocation formation in Ge on Si (001). *Computer Physics Communications*, 205:13–21, 2016.

[81] Q Xu, HQ Guan, ZH Zhong, SS Huang, and JJ Zhao. Irradiation resistance mechanism of the CoCrFeMnNi equiatomic high-entropy alloy. *Scientific Reports*, 11(1):608, 2021.

[82] Keli VS Thurston, Bernd Gludovatz, Anton Hohenwarter, Guillaume Laplanche, Easo P George, and Robert O Ritchie. Effect of temperature on the fatigue-crack growth behavior of the high-entropy alloy CrMnFeCoNi. *Intermetallics*, 88:65–72, 2017.

[83] Frederik Otto, Antonín Dlouhỳ, Konda Gokuldoss Pradeep, Monika Kuběnová, Dierk Raabe, G Eggeler, and Easo P George. Decomposition of the single-phase high-entropy alloy CrMnFeCoNi after prolonged anneals at intermediate temperatures. *Acta Materialia*, 112:40–52, 2016.

[84] Feng He, Zhijun Wang, Qingfeng Wu, Junjie Li, Jincheng Wang, and CT Liu. Phase separation of metastable CoCrFeNi high entropy alloy at intermediate temperatures. *Scripta Materialia*, 126:15–19, 2017.

[85] G Laplanche, S Berglund, C Reinhart, A Kostka, F Fox, and EP George. Phase stability and kinetics of σ-phase precipitation in CrMnFeCoNi high-entropy alloys. *Acta Materialia*, 161:338–351, 2018.

[86] FX Zhang, Shijun Zhao, Ke Jin, H Xue, G Velisa, H Bei, R Huang, JYP Ko, DC Pagan, JC Neuefeind, et al. Local structure and short-range order in a NiCoCr solid solution alloy. *Physical review letters*, 118(20):205501, 2017.

[87] Ruopeng Zhang, Shiteng Zhao, Colin Ophus, Yu Deng, Shraddha J Vachhani, Burak Ozdol, Rachel Traylor, Karen C Bustillo, JW Morris Jr, Daryl C Chrzan, et al. Direct imaging of short-range order and its impact on deformation in Ti-6Al. *Science advances*, 5(12):eaax2799, 2019.

[88] Yuan Wu, Fei Zhang, Xiaoyuan Yuan, Hailong Huang, Xiaocan Wen, Yihan Wang, Mengyuan Zhang, Honghui Wu, Xiongjun Liu, Hui Wang, et al. Short-range ordering and its effects on mechanical properties of high-entropy alloys. *Journal of Materials Science & Technology*, 62:214–220, 2021.

[89] Qing-Jie Li, Howard Sheng, and Evan Ma. Strengthening in multi-principal element alloys with local-chemical-order roughened dislocation pathways. *Nature communications*, 10(1):3563, 2019.

[90] Sheng Yin, Jun Ding, Mark Asta, and Robert O Ritchie. Ab initio modeling of the energy landscape for screw dislocations in body-centered cubic high-entropy alloys. *npj Computational Materials*, 6(1):110, 2020.

[91] Jun Ding, Qin Yu, Mark Asta, and Robert O Ritchie. Tunable stacking fault energies by tailoring local chemical order in CrCoNi medium-entropy alloys. *Proceedings of the National Academy of Sciences*, 115(36):8919–8924, 2018.

[92] Ruopeng Zhang, Shiteng Zhao, Jun Ding, Yan Chong, Tao Jia, Colin Ophus, Mark Asta, Robert O Ritchie, and Andrew M Minor. Short-range order and its impact on the CrCoNi medium-entropy alloy. *Nature*, 581(7808):283–287, 2020.

[93] Shijun Zhao, Yuri Osetsky, and Yanwen Zhang. Diffusion of point defects in ordered and disordered Ni–Fe alloys. *Journal of Alloys and Compounds*, 805:1175–1183, 2019.

[94] K Vörtler, N Juslin, G Bonny, L Malerba, and K Nordlund. The effect of prolonged irradiation on defect production and ordering in Fe–Cr and Fe–Ni alloys. *Journal of Physics: Condensed Matter*, 23(35):355007, 2011.

[95] Leonie Koch, Fredric Granberg, Tobias Brink, Daniel Utt, Karsten Albe, Flyura Djurabekova, and Kai Nordlund. Local segregation versus irradiation effects in high-entropy alloys: Steady-state conditions in a driven system. *Journal of Applied Physics*, 122(10):105106, 2017.

[96] Steven G Louie, Yang-Hao Chan, Felipe H da Jornada, Zhenglu Li, and Diana Y Qiu. Discovering and understanding materials through computation. *Nature Materials*, 20(6):728–735, 2021.

[97] Yangen Li, Jun-Ping Du, Peijun Yu, Rui Li, Shuhei Shinzato, Qing Peng, and Shigenobu Ogata. Chemical ordering effect on the radiation resistance of a conicrfemn high-entropy alloy. *Computational Materials Science*, 214:111764, 2022.

[98] De de Fontaine. The number of independent pair-correlation functions in multi-component systems. *Journal of Applied Crystallography*, 4(1):15–19, 1971.

[99] Shuai Guo, Hui Chen, and Meng Wang. Research on the dislocation differences of cocrfemnni with different local chemical orders during room temperature tensile test. *Journal of Alloys and Compounds*, 868:159215, 2021.

[100] MJ Norgett, MT Robinson, and I Mcalder Torrens. A proposed method of calculating displacement dose rates. *Nuclear engineering and design*, 33(1):50–54, 1975.

[101] Mohammad W Ullah, Dilpuneet S Aidhy, Yanwen Zhang, and William J Weber. Damage accumulation in ion-irradiated ni-based concentrated solid-solution alloys. *Acta Materialia*, 109:17–22, 2016.

[102] Huaqing Guan, Shaosong Huang, Jianhua Ding, Fuyang Tian, Qiu Xu, and Jijun Zhao. Chemical environment and magnetic moment effects on point defect formations in cocrni-based concentrated solid-solution alloys. *Acta Materialia*, 187:122–134, 2020.

[103] Yuri Osetsky, Alexander V Barashev, Laurent K Béland, Zhongwen Yao, Keyvan Ferasat, and Yanwen Zhang. Tunable chemical complexity to control atomic diffusion in alloys. *npj Computational Materials*, 6(1):38, 2020.

[104] Zeqi Shen, Jun-Ping Du, Shuhei Shinzato, Yuji Sato, Peijun Yu, and Shigenobu Ogata. Kinetic monte carlo simulation framework for chemical short-range order formation kinetics in a multi-principal-element alloy. *Computational Materials Science*, 198:110670, 2021.

[105] Helmut Mehrer. *Diffusion in solids: fundamentals, methods, materials, diffusion-controlled processes*, volume 155. Springer Science & Business Media, 2007.

[106] Benjamin Schuh, F Mendez-Martin, Bernhard Völker, Easo P George, Helmut Clemens, R Pippan, and Anton Hohenwarter. Mechanical properties, microstructure and thermal stability of a nanocrystalline cocrfemnni high-entropy alloy after severe plastic deformation. *Acta Materialia*, 96:258–268, 2015.

[107] Jun Ding, Mark Asta, and Robert O Ritchie. Melts of crconi-based high-entropy alloys: Atomic diffusion and electronic/atomic structure from ab initio simulation. *Applied Physics Letters*, 113(11):111902, 2018.

[108] NAP Kiran Kumar, C Li, KJ Leonard, H Bei, and SJ Zinkle. Microstructural stability and mechanical behavior of fenimncr high entropy alloy under ion irradiation. *Acta Materialia*, 113:230–244, 2016.

[109] Hong Luo, Zhiming Li, Andrea M Mingers, and Dierk Raabe. Corrosion behavior of an equiatomic cocrfemnni high-entropy alloy compared with 304 stainless steel in sulfuric acid solution. *Corrosion Science*, 134:131–139, 2018.

[110] Yanwen Zhang, Shijun Zhao, William J Weber, Kai Nordlund, Fredric Granberg, and Flyura Djurabekova. Atomic-level heterogeneity and defect dynamics in concentrated solid-solution alloys. *Current Opinion in Solid State and Materials Science*, 21(5):221–237, 2017.

[111] Shijun Zhao, Yuri Osetsky, Alexander V Barashev, and Yanwen Zhang. Frenkel defect recombination in ni and ni–containing concentrated solid–solution alloys. *Acta Materialia*, 173:184–194, 2019.

[112] Shijun Zhao, William J Weber, and Yanwen Zhang. Unique challenges for modeling defect dynamics in concentrated solid-solution alloys. *Jom*, 69(11):2084–2091, 2017.

[113] Shijun Zhao, Takeshi Egami, G Malcolm Stocks, and Yanwen Zhang. Effect of d electrons on defect properties in equiatomic nicocr and nicofecr concentrated solid solution alloys. *Physical Review Materials*, 2(1):013602, 2018.

[114] Blas Pedro Uberuaga, Louis J Vernon, Enrique Martinez, and Arthur F Voter. The relationship between grain boundary structure, defect mobility and grain boundary sink efficiency. *Scientific reports*, 5(1):9095, 2015.

[115] L Barnard and D Morgan. Ab initio molecular dynamics simulation of interstitial diffusion in ni–cr alloys and implications for radiation induced segregation. *Journal of Nuclear Materials*, 449(1-3):225–233, 2014.

[116] Chao Jiang, Larry K Aagesen, David Andersson, Christopher Matthews, and Fergany Badry. Bulk and surface diffusion of neodymium in alpha-uranium: Ab initio calculations and kinetic monte carlo simulations. *Journal of Nuclear Materials*, 557:153307, 2021.

[117] JD Tucker, R Najafabadi, TR Allen, and D Morgan. Ab initio-based diffusion theory and tracer diffusion in ni–cr and ni–fe alloys. *Journal of Nuclear Materials*, 405(3):216–234, 2010.

[118] Shijun Zhao, Yuri Osetsky, and Yanwen Zhang. Preferential diffusion in concentrated solid solution alloys: Nife, nico and nicocr. *Acta Materialia*, 128:391–399, 2017.

[119] Toshiyuki Koyama, Yuhki Tsukada, and Taichi Abe. Simple approach for evaluating the possibility of sluggish diffusion in high-entropy alloys. *Journal of Phase Equilibria and Diffusion*, 43(1):68–77, 2022.

[120] Leqing Liu, Xiongjun Liu, Qing Du, Hui Wang, Yuan Wu, Suihe Jiang, and Zhaoping Lu. Local chemical ordering and its impact on radiation damage behavior of multi-principal element alloys. *Journal of Materials Science & Technology*, 135:13–25, 2023.

[121] Zhen Zhang, Zhengxiong Su, Bozhao Zhang, Qin Yu, Jun Ding, Tan Shi, Chenyang Lu, Robert O Ritchie, and Evan Ma. Effect of local chemical order on the irradiation-induced defect evolution in crconi medium-entropy alloy. *Proceedings of the National Academy of Sciences*, 120(15):e2218673120, 2023.

[122] Koji Inoue, Shuhei Yoshida, and Nobuhiro Tsuji. Direct observation of local chemical ordering in a few nanometer range in cocrni medium-entropy alloy by atom probe tomography and its impact on mechanical properties. *Physical Review Materials*, 5(8):085007, 2021.

[123] Lingling Zhou, Qi Wang, Jing Wang, Xuefei Chen, Ping Jiang, Hao Zhou, Fuping Yuan, Xiaolei Wu, Zhiying Cheng, and En Ma. Atomic-scale evidence of chemical short-range order in crconi medium-entropy alloy. *Acta Materialia*, 224:117490, 2022.

[124] Peijun Yu, Jun-Ping Du, Shuhei Shinzato, Fan-Shun Meng, and Shigenobu Ogata. Theory of history-dependent multi-layer generalized stacking fault energy—a modeling of the micro-substructure evolution kinetics in chemically ordered medium-entropy alloys. *Acta Materialia*, 224:117504, 2022.

[125] Haitao Gao, Guiqiang He, Qi Li, Yangen Li, Wei Hu, Shaojie Zhou, Fengmei Liu, Jianglong Yi, Yupeng Zhang, Zhihong Cai, et al. Diffusion bonding of high entropy alloy and stainless steel at a relative lower temperature via surface nanocrystallization treatment. *Journal of Materials Research and Technology*, 24:475–487, 2023.

[126] Shūichi Nosé. A molecular dynamics method for simulations in the canonical ensemble. *Molecular physics*, 52(2):255–268, 1984.

[127] Bin Xing, Xinyi Wang, William J Bowman, and Penghui Cao. Short-range order localizing diffusion in multi-principal element alloys. *Scripta Materialia*, 210:114450, 2022.

Acknowledgements

This dissertation was written under the supervision of Professor Shigenobu Ogata while I was preparing to obtain my doctoral degree at the Graduate School of Engineering Science, Osaka University. I would like to express my deepest appreciation to my supervisor, Professor Shigenobu Ogata of Osaka University, for his excellent and detailed guidance, encouragement, inspiring, and for giving me the opportunity to complete my doctoral studies at Osaka University. I would like to thank my dissertation committee members, Professor Ryuichi Tarumi and Professor Atsutomo Nakamura, for their comments and suggestions of this dissertation. I am also deeply grateful to my former supervisor Professor Rui Li of University of Science and Technology Beijing (USTB), and Professor Qing Peng of Chinese Academy of Sciences, for their guidance from my master studies and for inspiring me in research.

I would like to thank Associate Professor Akio Ishii, Assistant Professor Shuhei Shinzato, laboratory members Mr. Jun-ping Du, Mr. Fanshun Meng and Mr. Peijun Yu (Current affiliation: Hainan University) and other researchers who are not listed here for the valuable discussion and unfailing help in my study and research. I also appreciate secretary Ms. Kaori Fujita for her help in my daily life in Japan as well as all the students in Ogata Laboratory.

The contents of Chapter 2 were mainly completed when I was master student in USTB. I still miss my studies there. I am very grateful to my former supervisor Professor Rui Li for her guidance at that time and to the other students in the laboratory for their help. I would like to extend my gratitude to Professor Qing Peng for his

useful comments and technical assistance. I would like to thank Mr. Jun-ping Du and Mr. Peijun Yu for their detailed discussions and useful opinions about my research, which enabled me to complete the Chapter 3 and Chapter 4 of this dissertation. I also thank all of my collaborators for the opportunity to complete some outstanding works together: Professor Lei Gao of USTB and Professor Haitao Gao of Guangdon Academy of Sciences.

I would also like to extend my sincerest appreciation to all of my friends in Japan, for all the joy and help they have given me. Studying abroad and completing the doctoral study is a tough process, especially during the three years when the COVID-19 pandemic was raging and we had supported each other. Fortunately, thanks to you all, I was able to stay healthy and complete my studies successfully. I hope that I have contributed the same thing to you and that you will soon be able to complete your studies and realize your dreams. It has been a wonderful memory and I will miss this period of study abroad immensely! In particular, I would like to thank the Next-Generation project (JST) and the Scholarship of Japan Student Services Organization (JASSO) for their financial support.

Finally, I would like to express my deeply grateful to my parents. For their endless love, support and encouragement throughout all my studies and life.

May all the beauty be blessed.

Yangen Li

September 2023

List of publications

Academic journal papers:

1. Yangen Li, Jun-Ping Du, Peijun Yu, Rui Li, Shuhei Shinzato, Qing Peng, and Shigenobu Ogata. "Chemical ordering effect on the radiation resistance of a CoNiCrFeMn high-entropy alloy". *Computational Materials Science*, 214:111764, 2022.

2. Yangen Li, Rui Li, Qing Peng, and Shigenobu Ogata. "Reduction of dislocation, mean free path, and migration barriers using high entropy alloy: Insights from the atomistic study of irradiation damage of CoNiCrFeMn". *Nanotechnology*, 31(42):425701, 2020.

3. Yangen Li, Rui Li, and Qing Peng. "Enhanced surface bombardment resistance of the CoNiCrFeMn high entropy alloy under extreme irradiation flux". *Nanotechnology*, 31(2):025703, 2019.

4. Yangen Li, Shigenobu Ogara et al. "Chemical order promoted interstitial and vacancy sluggish diffusion in CrCoNi medium-entropy alloy". *To be submitted*